Sensor-Based In-situ Process Control of Robotic Wire Arc Additive Manufacturing Integrated with Machine Learning

by

Yeon Kyu Kwak

A thesis submitted in partial fulfillment of the requirements for the degree of

Master of Science

in

Control Systems

Department of Electrical and Computer Engineering

University of Alberta

Abstract

Wire Arc Additive Manufacturing (WAAM) is a manufacturing technology that has the capability to fabricate a large-scale metallic part in a layer-by-layer fashion. It is receiving significant attention from many industries as a viable method of manufacturing as it has a high deposition rate, production rate, and cost efficiency. However, numerous challenges still need to be addressed and overcome to ensure the geometrical accuracy of the manufactured goods produced. As the number of deposited layers increases, geometrical errors increase, and the accumulated heat becomes significant, leading to the undesirable slumping of the beads. The quality of the part can be enhanced through in-situ real-time feedback control. However, as WAAM is a time-variant process that is highly non-linear and multi-dimensional, it is difficult to model the relation between the process parameters and the final quality of the produced part. To address this challenge, a sensor-based in-situ data-driven process control framework integrated with machine learning (ML) is proposed to iteratively learn from the feedback, the impacts of various process parameters to ultimately control the geometry of a single-bead multi-layer part to conform to desired geometrical specifications. The proposed control framework is then implemented and validated on a custom robotic large-scale WAAM system. The experiment result showed that the beads printed with the proposed control framework had a noticeable improvement in both consistency and following the user-specified bead's geometry, in comparison to traditional printing beads.

Acknowledgements

I would like to show a sincere gratitude to my graduate studies supervisors Dr. Mahdi Tavakoli and Dr. Ahmed Jawad Qureshi for providing excellent guidance and support throughout the research. I also thank post doctorate fellow Dr. Thomas Lehman, Dr. Abdullah Mohiuddin, and lab group members for providing technical insights and encouragement.

Table of Contents

List of Tables

List of Figures

List of Abbreviations

AE	Acoustic Emission
AI	Artificial Intelligence
AM	Additive Manufacturing
APCS	Adaptive Process Control Scheme
BTF	Buy-To-Fly
CAD	Computer-aided design
CCD	Charge-Coupled Devices
CMT	Cold Metal Transfer
CNN	Convolutional Neural Network
DED	Direct Energy Deposition
EBAM	Electron Beam Additive Manufacturing
FGM	Functionally Graded Materials
GA	Genetic Algorithm
GMAW	Gas Metal Arc Welding
GTAW	Gas Tungsten Arc Welding
GUI	Graphic User Interface
HDR	High Dynamic Range
IPM	Inches Per Minute
LMD	Laser Metal Deposition
LPBF	Laser Powder Bed Fusion

LSFF	Laser Solid Freeform Fabrication
MDP	Markov Decision Process
ML	Machine Learning
MPC	Model Predictive Control
PBF	Powder Bed Fusion
PID	Proportional-Integral-Derivative
PTAW	Transferred Arc Welding
ROS	Robotic Operating System
SAW	Submerged Arc Welding
SFF	Solid Freeform Fabrication
SLM	Selective Laser Melting
SM	Shape Melting
SMD	Shape Metal Deposition
SOD	Standoff Distance
SVM	Support Vector Machine
SW	Shape welding
TIG	Tungsten Inert Gas
TTS	Torch Travel Speed
WAAM	Wire Arc Additive Manufacturing
WFS	Wire Feed Speed
WLAM	Wire Laser Additive Manufacturing

1. Introduction

1.1 Motivation

Wire arc additive manufacturing (WAAM) is an emerging technology that is attracting interest from manufacturing industries and academia due to its potential to fabricate large-scale metal components with the benefits of low cost and short production lead time. It uses Direct Energy Deposition (DED) process by using wire and electric arc as a fusion source to deposit materials in a layer-by-layer fashion until a desired 3D part is fabricated. Not only it benefits from significant raw material savings in comparison to conventional manufacturing methods like CNC machining and forging [1], but it also offers competitive benefits in cost savings relative to other similar DED additive manufacturing technologies as well, such as Laser Metal Deposition (LMD), Wire Laser Additive Manufacturing (WLAM) and Electron Beam Additive Manufacturing (EBAM). Additionally, in comparison to the common powder-based additive manufacturing (AM) like powder bed fusion (PBF), WAAM uses wire as feedstock which costs less than the powder feedstock and offers high efficiency in the deposition of materials and no need for a peripheral powder recycling process [2], alleviating potential health and safety risks. WAAM also offers a competitive edge for being able to manufacture with a greater range of feedstock materials [3], and is suitable for manufacturing large-scale components with modest complexity with a high production rate.

Manufacturing industries are attracted to WAAM for its potential to manufacture large custom-made metal workpieces with high material utilization rates. For instance, the aerospace industry is expected to require approximately 20 million tons of billet materials due to the high buy-to-fly (BTF) ratio of materials used in the industry like titanium [4]. BTF is the weight of the raw material divided by the weight of the final component. High BTF is a result of poor machinability of the manufactured part [5]. With machining rates of about 90% and increasing material costs, the benefits of additive manufacturing often outweigh traditional subtractive manufacturing [6]. To demonstrate the benefits of WAAM in comparison to other additive manufacturing techniques, Panchenko et al. [7] evaluated the advantages of WAAM in a scale of 0 to 10 relative to other additive manufacturing processes as seen in Figure 1.1. Though

WAAM lacks in accuracy and complexity of the part, it outperforms other methods with its relatively inexpensive cost, high material deposition rate, strength, and power efficiency.

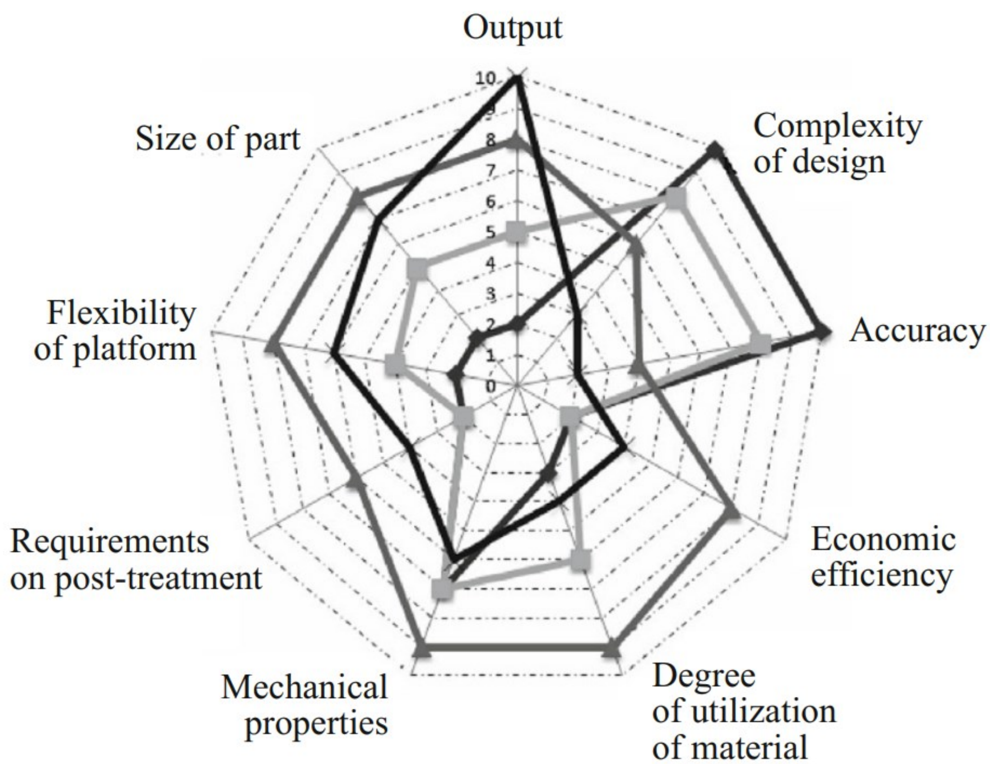

Figure 1.1 Advantage of WAAM over other Additive Manufacturing processes. ♦) bed deposition; ■) direct deposition; ×) electron beam freeform fabrication ▲) WAAM [7]

While WAAM has the ability to produce components with a high deposition rates and significant cost savings, it suffers from a lack of dimensional accuracy in the final product. As WAAM fabricates a component in a layer-by-layer fashion, a buildup of an error may occur where a small error in a previous layer would gradually build up throughout every layer, further negatively affecting the geometrical accuracy of the produced part. Various input parameters affect the geometrical accuracy of the final part, and they are often difficult to control as they are highly non-linear and coupled [8]. To overcome this challenge, control of process parameters is required as it would be able to rectify errors and correct itself throughout the manufacturing process. However, WAAM is a very complex time-variant dynamic process with numerous process parameters. Some of the input process parameters include torch positioning and speed, wire feed rate, dwell time, voltage, and current. To conform to the geometrical specifications, these parameters need to be monitored and controlled in real time. Monitored process parameters in this study include thermal and geometrical information of beads at the location of the deposition.

Table 1.1 Cost comparison of wire and powder as feedstocks for varying materials

Feedstock	Titanium 6AL-4V ($/lbs.)	Tantalum ($/lbs.)	Inconel 625 ($/lbs.)	Stainless Steel 316 ($/lbs.)
Wire – diameter 0.9mm	58	545.30	26.73	5.19
Powder – AM grade	77	522.00	48.00	10.00

1.2 Thesis Objectives

Overall, this research aims to develop an in-situ reinforcement learning control framework for the WAAM process to improve the geometrical quality of a multi-layer single-track wall. Specifically, the research objective of this research is as follows:

- Explore and extend knowledge of machine learning in its adaptability and suitability for application of WAAM process in-situ control.
- Develop a sensor-based in-situ control framework on a 3-axis robotic gantry system with WAAM.
- Discuss the effectiveness of the in-situ machine learning control framework in improving the geometrical quality of the printed part.

The first necessary step in achieving the objective was to research various ML techniques applicable to the WAAM process. Then an appropriate control framework was developed in software tools that can incorporate the researched ML techniques. Along with sensor integrations to collect the in-situ process data, the objective of the research was fulfilled.

This thesis proposes a method of sensor-based in-situ control of robotic WAAM integrated with machine learning (ML) techniques for the printing of multi-layer single-track walls. The term in-situ means ‘on site’ or online. Input process parameters controlled in the study include wire feed speed, torch travel speed, previous bead’s geometry, and standoff distance between the torch and the bead. The output or the geometrical quality analyzed in the study includes the width and the height of the printed bead. Two algorithms, namely Q-learning and policy gradient algorithms were simulated on a custom-built simulator and then tested in a real-world scenario. Additionally, by utilizing the historical input and output process parameters, a reinforced inverse supervised learning control algorithm is developed and experimented to show improvement in the geometrical quality of the printed workpiece.

2 Background

The background consists of the introduction to metal additive manufacturing, its history, and its different types. It also contains a brief introduction to various types of machine learning, namely reinforcement learning and supervised learning. Lastly, state-of-art papers related to the numerous sensing techniques and control of the metal additive manufacturing process are introduced.

2.1 Metal Additive Manufacturing

Subtractive manufacturing is a traditional way of manufacturing where an over-dimensioned block of raw material is machined down to the desired component. In contrast, additive manufacturing deposits the material in a layer-by-layer fashion to manufacture a component [9]. It is an innovative manufacturing process that produces a three-dimensional component directly through the use of the Computer-Aided Design (CAD) model. The major advantage of AM is that it reduces the time taken to manufacture and increases the buy-to-fly ratio [10] [11]. It provides enormous potential for cost savings in the machining of high-strength alloys and is widely adopted in marine, aeronautical and aerospace industries [12]–[16]. It can also fabricate large-scale industrial components using a type of alloy that is costly to manufacture by traditional methods [17]. AM can utilize a vast variety of materials including functionally graded materials (FGM) for production providing edges over other manufacturing processes [18] [19].

Numerous techniques have been developed for metal manufacturing AM processes, such as shape deposition manufacturing [20], selective laser sintering [21], electron beam freeform fabrication [22], direct metal deposition [23] and WAAM [24], [25]. Prominent techniques in how the feedstock for additive manufacturing is supplied are powder-feed or wire-feed processes [26], [27]. AM with powder-feed technology can fabricate components with precise geometrical accuracy but in a small volume. In contrast, the wire-feed technique can manufacture a larger component in a cleaner and more environmentally friendly way where the operator is not exposed to any potentially hazardous powder. It also has a material usage efficiency of up to 100%. Moreover, the cost of material is significantly lower with high availability, making the wire-feed method to be very competent.

2.1.1 History of Wire Arc Additive Manufacturing

While the acronym of WAAM has only emerged only about 20 years ago, the concept of near net shape manufacturing by welding has existed for the past century. Shape welding (SW), shape melting (SM), solid freeform fabrication (SFF), shape metal deposition (SMD), and 3D welding [28] were the names that were representing the contemporary welding techniques used to produce metal parts with unique shapes.

The first concept of metal additive manufacturing dates to 1920 when Baker filed a patent, “The use of an electric arc as a heat source to generate 3D objects depositing molten metal in superimposed layers”, to form a manufactured product as shown in Figure 2.1 [29]. White in 1964 manufactured a metal cylinder using submerged arc welding (SAW) as means of creating a compression roller [30]. Later, Ujiie from Mitsubishi proposed a method of fabricating a pressure vessel using SAW, tungsten inert gas (TIG), and multiple types of wires to give a functionally graded wall. Ujie further discussed the machining of the surfaces of the final product. By 1983, Thyssen company produced components out of weld metal and successfully built a 79 tons multilayer weldment by shape welding technique with a deposition rate of 80kg per hour [31]. WAAM in the 1970s and 80s was referred to as shape welding and was performed for large parts.

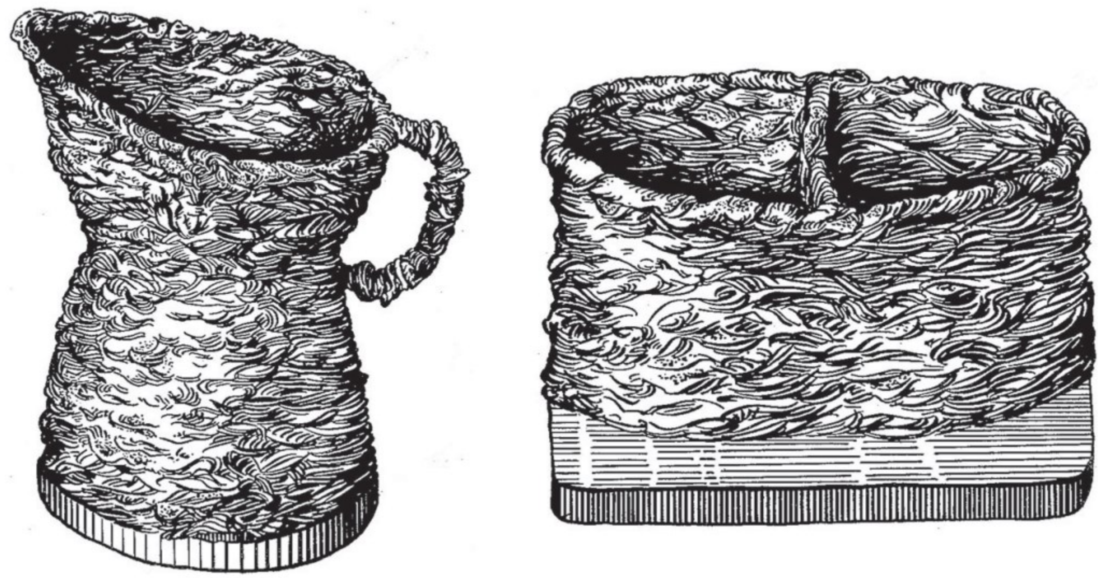

Figure 2.1 Products made by Baker using concept of metal additive manufacturing in 1920 AD [29]

Along with the advancement in computer-aided design and manufacturing (CAD/CAM), in 1992, Dickens et al. [32] utilized a 3D robot welding system and a CAD system to generate welding trajectories to manufacture a steel part. Prinz and Weiss patented methods of combining built parts with computerized numerical control (CNC) milling was referred to as Shape Deposition Manufacturing (SDM). Cranfield University and Rolls Royce developed the SMD technique to produce an aero-engine component with Ti-6Al-4V and Inconel 718 alloys from 1994 to 1999. WAAM is an SDM technology that is named by Cranfield University.

Figure 2.2 World's first ship propeller fabricated with WAAM in 2017 by RAMLAB [33]

Varying aspects of studies within the field of WAAM have evolved into more specific categories such as path planning, process surveillance and control, materials, post-processing, and more to make WAAM more applicable and practical [34]. Today, the complexity and variety of manufactured products have grown immensely. Figure 2.3 shows a WAAM-manufactured propeller being fabricated to be equipped on a ship. Figure 2.3 shows the first architectural application of WAAM where a 7.8-ton bridge is made.

Figure 2.3 MX3D bridge at Dutch Design Week 2018 [35]

2.1.2 Gas shielded metal arc welding

There are three methods to process the fabrication of large-scale metal parts in WAAM. They are Plasma Transferred Arc Welding (PTAW) [36], [37], Gas Tungsten Arc Welding (GTAW) [32], [38] and Gas Metal Arc Welding (GMAW) [39], [40]. The deposition technique utilized in the paper is Cold Metal Transfer (CMT) which is a subset of GMAW. A diagram of the GMAW process is depicted in Figure 2.4. GMAW torch feeds a consumable electrode or a feedstock material in a form of wire and strikes an arc between the substrate plate and the wire. The arc then melts the tip of the wire and deposits material onto the substrate. As the material is deposited at high temperatures, the material is prone to corrosion and oxidation. Therefore, shielding gas is in place to prevent the metal to react with the surrounding oxygen. The deposition rate of the GMAW method is approximately 2-3 times greater than that of the GTAW and the PTAW method. However, this comes at the expense of lower stability in manufacturing. The GMAW-based method generally produces more fume and spatters as the electric current directly acts on the feedstock [41]. Consideration of processing conditions and the production rate for the target component is required when deciding what WAAM technique is to be utilized.

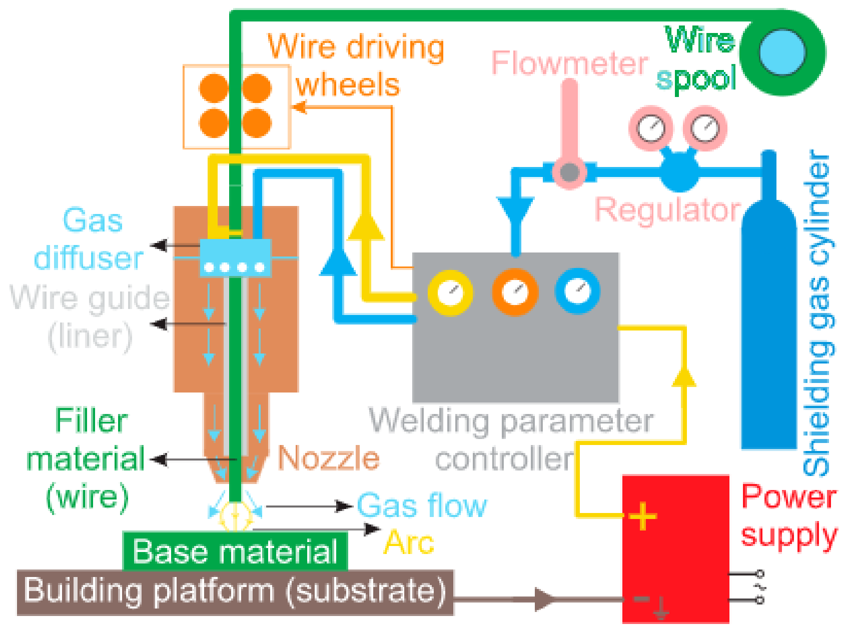

Figure 2.4 Gas metal arc welding process diagram [42]

2.1.3 Cold metal transfer

CMT is developed by Fronius Company from Austria in 2004 and is a subset of GMAW and a variation of the GMAW process. With the integration of high-speed electronics and mechanical controls, CMT primarily modified GMAW in the method of deposition or the wire feeding technique. CMT creates a weldment in a drop-by-drop fashion where an arc strike creates a single droplet of metal to be deposited onto the substrate. This drop-by-drop of the welding material is achieved by reducing the welding current and retracting the wire when a short circuit is detected in a repeated manner at very high frequency [43], [44].

The CMT process is characterized by its innovative method of a detachment of a weld drop through the motion of the wire, and the digital process control of the power supply. The process can be divided into repeating cycles of the following four stages of the process:

1. Arc is ignited with high voltage and current, melting the tip of the filler wire. Along with the rest of the wire from the torch, a globule of the melted wire moves toward the weld pool.

2. As the material dips into the molten weld material, a short-circuit is achieved and the arc is extinguished, and the digital controller decreases the welding current. The globule created from the last step is transferred to the weld pool.
3. The wire from the torch is retracted rapidly to facilitate the metal droplet to be detached from the wire.
4. The wire is retracted into the torch. Welding voltage and current are raised to ignite the arc again. It is ready to extend forward to reignite the arc, raising the temperature for the repeating cycle.

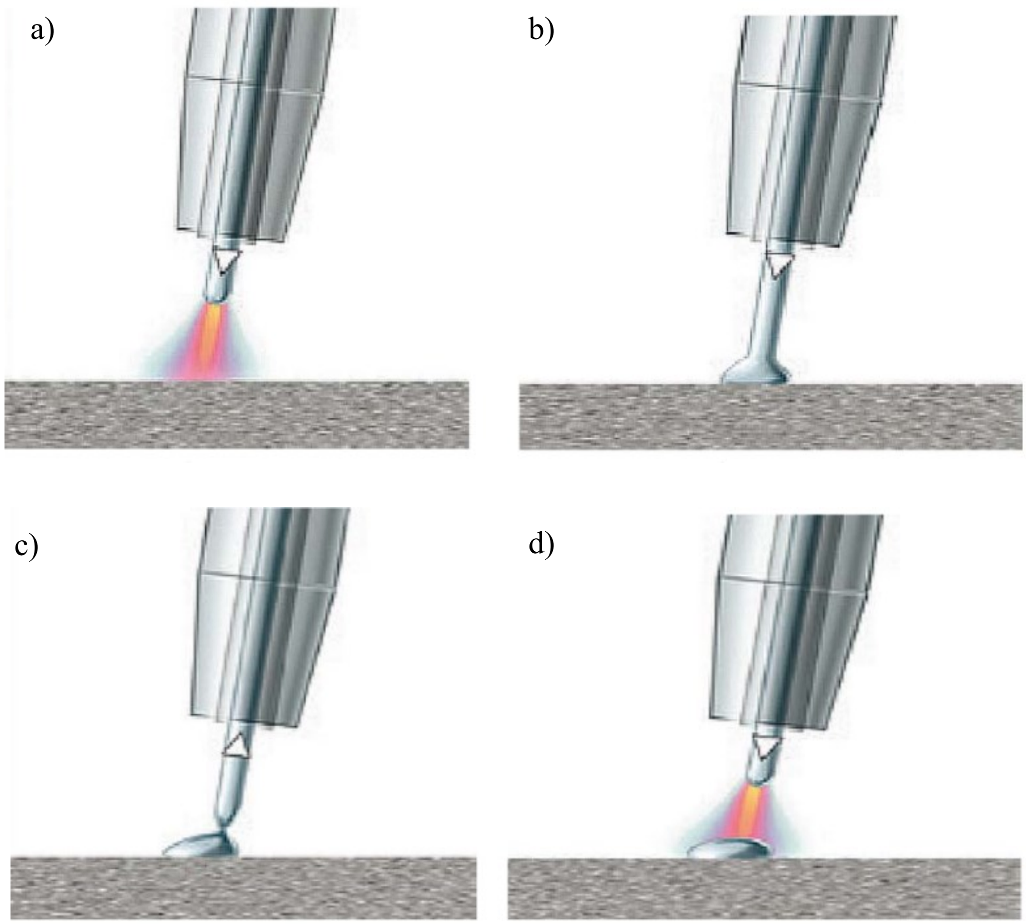

Figure 2.5 Four phases of wire feed process in CMT welding [45]

Due to the igniting, extinguishing and retracting procedure of CMT, in comparison to GMAW, CMT is spatter free with less arc, thus less heat input. The term ‘cold’ from CMT is best understood in terms of the welding process where the arc is extinguished, and the wire is retracted back into the torch. Additionally, with advancement of digital and mechanical control systems, CMT can regulate welding parameters like the arc length, amount of heat input and wire feed speed.

2.1.4 WAAM Process parameters

Despite the advantage of WAAM, the drawback is evident. In relation to the other metal additive manufacturing technologies, the final product of the WAAM process lacks geometrical accuracy, such as layer width and layer height. A few of the primary factors that influence the output geometry of WAAM are the dwell time, the geometry of the previous layer, wire feed speed, torch travel speed, shielding gas flow rate, and torch standoff distance. For example, changes in the heat input of the system or wire feed speed, or the torch travel speed can cause significant alteration to the geometry of the deposited bead, thus the quality of the entire manufactured part [46]. Furthermore, as these parameters are multi-dimensional and non-linear in relation to the resulting geometry of the printed beads of layer, it is often difficult to develop a model for the process.

2.2 Machine learning

Over the past decade, machine learning and artificial intelligence (AI) have become popular subjects both within and outside of the academic community. Machine learning is an important component of the growing field of science. Machine learning is simply defined as enabling computers to make a successful prediction based on their past experiences [47]. In many scientific disciplines, the objective of studies is often focused on modeling the relationship between the given input and the resulting outputs. With a mathematical model of the system developed, it is possible to predict the output of a system with only sets of input variables. However, this modeling and prediction of output given input may be a very difficult task as many phenomena encountered in the real world are multi-dimensional and highly non-linear to be put into a closed-form input-to-output relationship. ML is utilized in the thesis as physical models are often difficult to derive and are usually incomplete, and inaccurate. Training in ML refers to a process of algorithms building a model and the training data refers to the required set of data that is used for training. Once a model is trained, the model can be utilized as a tool to map the input data to that of the output to make a useful prediction when given a novel input that may or may not be part of the training data.

The accuracy of the model learned depends on a number of factors such as the accuracy, quality, and size of training data, the complexity of the input and output relationship, and computational constraints like the memory of the computing machine [48]. With the recent advancement of digital data gathering, storing, and processing power, the application of machine learning has broadened to a variety of industries such as robotics, bioinformatics, marketing and sales, transportation, oil and gas, and financial analysis [49].

There are three main categories in ML, namely, supervised learning, unsupervised learning, and reinforcement learning. The type of ML discussed in the paper is primarily based on supervised learning and reinforcement learning. Unsupervised learning is not discussed in this thesis as it is a method of recognizing a pattern in input data to predict output without any information on the output; therefore it is only useful if there is only input data without any corresponding output. However, the method of supervised learning and reinforcement learning both emphasizes the need for both input and output data. Supervised learning can model the input-to-output relationship through the use of both input and output data. RL aims to find an optimized policy such that if given a set of input data, it determines what actions to take to obtain the best outcome.

2.2.1 Reinforcement learning

Reinforcement learning is an area of Artificial Intelligence and a branch of machine learning that has emerged as an effective means of solving sequential decision problems in a wide range of fields and industries such as game theory, autonomous driving, robotics, and more [50].

Reinforcement learning is known to resemble the learning process of a human being. For example, a student chooses not to sleep before an exam, and that results in a bad grade. The student learns from this experience and chooses to get sufficient sleep before other upcoming exams.

The framework of RL allows an agent to interact with an environment and the goal of the agent is to learn to take an action inside the environment such that it receives maximized cumulative reward over time [51]. Or the agent in an environment attempts to learn the optimal sequence of actions to maximize reward. This concept of RL can be modeled as a Markov Decision Process (MDP) [52]. The major advantage of MDP is their generality in the ability to handle nonlinear and stochastic dynamics and nonquadratic reward functions [53]. The next advantage is that contrary to supervised learning, it may be in a model-free form. Thus, it does not need a model of environment dynamics, and simply learns either online, by gathering transition samples directly from the interaction with the model, or offline by utilizing samples obtained beforehand. This generality provides a significant value in designing an optimal controller for a non-linear and stochastic dynamic system.

2.2.2 Supervised learning

Supervised learning is applied when the training data is given in the form of input and output target value pairs [54]. A supervised learning algorithm learns the mapping function that models the input-to-output relation. It is utilized when specific goals are identified to be accomplished from a specific set of inputs. It is a "task-driven approach" [55].

Supervised learning can be classified into a classification or a regression problem. First, classification algorithms are used in supervised learning to address problems in which the output variable is categorical, such as male or female, good or bad, and yes or no. The classification algorithm can predict the outcome based on the input. A popular example of the application of classification is spam filtering. Next, regression is used to solve problems that have a correlation between the input and output variables. Regression finds this correlation to predict continuous output variables given input variables. Weather prediction is one example of a supervised learning regression problem.

2.3 State of the art

Wire arc additive manufacturing requires various welding processes to facilitate the deposition in a layer-by-layer fashion. First comes a CAD model that is converted to a machine path by 3D slicing software. This manufacturing process is often done with sensory information feedback to the welding process control system to produce a compliant part as shown in Figure 2.6.

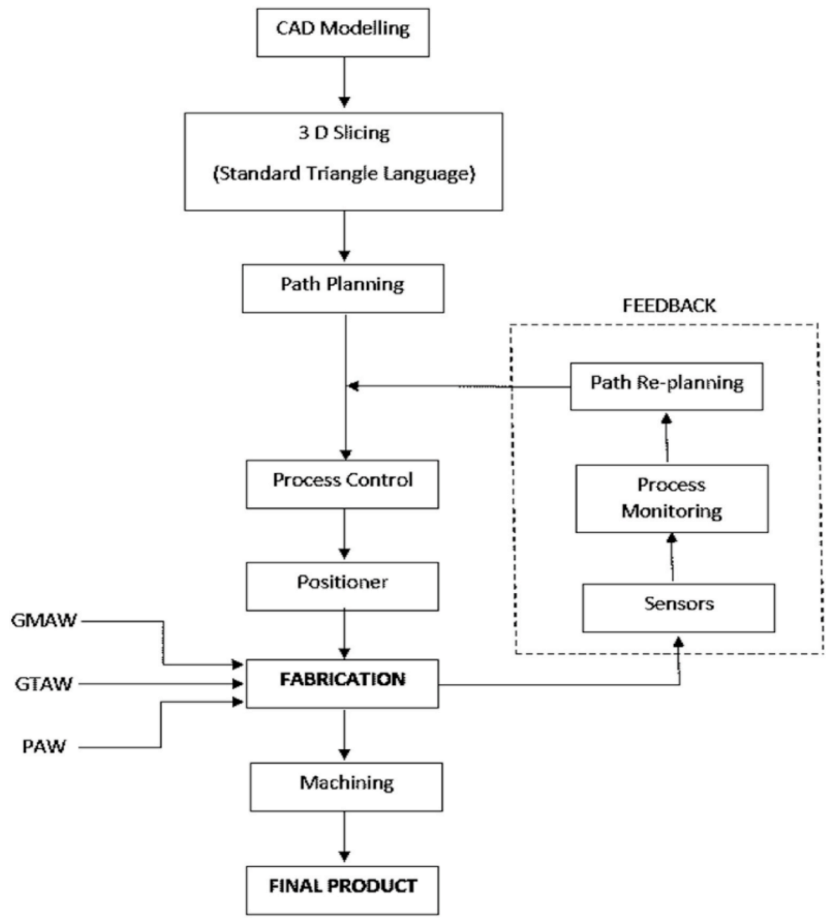

Figure 2.6 Overall flowchart for performing WAAM with sensor feedback [56]

2.3.1 Process monitoring in WAAM

To comply with geometrical, mechanical, or metallurgical specifications such as the deposited bead's width and height, the input process parameters such as the wire feed speed, dwell time, and torch travel speed needs to be controlled in real-time while the part is being fabricated. Before having to control any of these input process parameters, it is important to quantify and measure the output of the system. During the fabrication stage of the WAAM process, various sensing units and optical systems are utilized to obtain real-time data of the additive manufacturing process. The data gathered from the sensory equipment are used alongside the input process parameter into a control system, which will ultimately conform the finished component to the geometrical specifications and constraints. Sensors that are commonly used to monitor the welding site use acoustic [57], vision [34], spectral [58], and thermal [59] data. A combination of these various sensors is often deployed to provide greater insights into the WAAM process. Pringle et al. [60] developed an open-source arc analyzer by combining voltage, current, acoustic, spectral, and thermal sensors on the WAAM of an aluminum part to analyze the sensitivity of each sensor on varying wire feed speeds. Xu et al. [61] proposed a multi-sensor monitoring and control system by utilizing profile, voltage, current, gas flow, and oxygen sensors. Flowchart of the deposition control process with sensor observation and control stage is shown in Figure 2.7 where it shows more details into the feedback loop Figure 2.6.

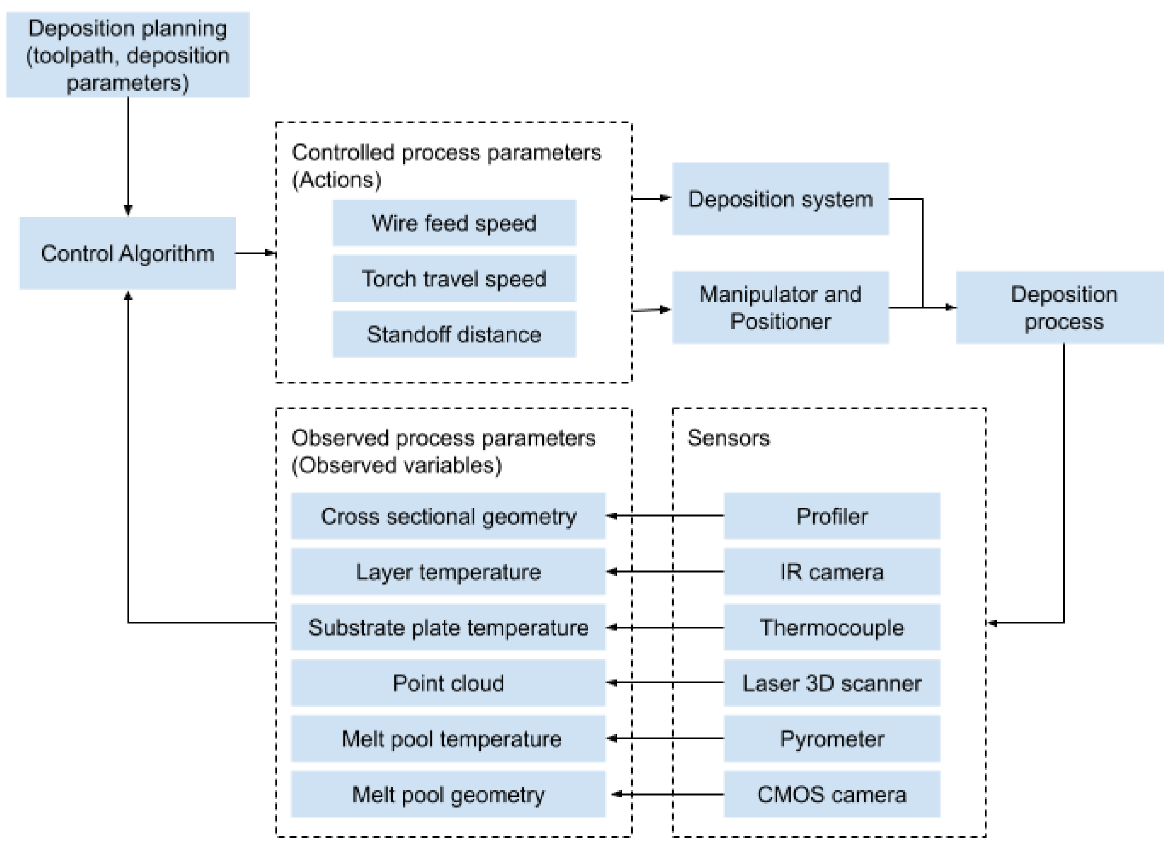

Figure 2.7 Flowchart of the WAAM deposition control process with various sensors to monitor the deposition process

2.3.1.1 Vision sensing

Vision sensing in WAAM is utilized for measurements and analysis of bead layer and surface geometry. Along with the ongoing development of computer vision technology, a large number of studies were done with the vision sensing techniques of the metal AM process in hopes of providing vital information to perform analysis and controls. Davis et al. [62] proposed an approach for non-contact online clad height measurement with high accuracy. Charge-coupled device (CCD) camera and line laser were used in combination with unique line detection and spur trimming algorithm to measure the complete clad profile. Clijsters et al. [63] designed an in-situ optical measurement system consisting of high-speed infrared thermal CMOS (complementary metal oxide semiconductor) camera and a photodiode for monitoring and logging of melt pool data at high sampling rate. The obtained data is post-processed into a mapping algorithm to provide the characteristics of the molten pool. The reliability of the system was validated by comparing defects found in real time to the defect discovered in the printed part. Grasso et al.[64] developed an in-situ vision monitoring system for an SLM process by acquiring images of byproducts generated through the AM process. It acquires plume images which are put through machine learning algorithms to detect unstable melting conditions that may result in defects. Zhang et al. [65] identified three levels of the final product quality by capturing the image of the melt pool, plume, and spatters in the LPBF process in an offline manner. Images were acquired with a high-speed camera, and they were post-processed by extraction of key features which are used as inputs for support vector machine (SVM) and convolutional neural network (CNN) classifiers. Repossini et al. [66] monitored and identified the quality of the LPBF process by using post-processed in-situ spatter images captured with a high-speed camera.

Research related to vision sensing in WAAM had been performed not only on the bead but also on the wire. For instance, the direction of the wire-feeding significantly influences the different droplet transfer modes, lowering the accuracy and quality of the built part. Tang et al. [67] developed a detection and classification system capable of detecting surface defects. CMOS camera was used to obtain layer surface images. SVM was used to post-process the images to categorize the defect into normal, depression, pore, hump, or undercut. Bonaccorso et al. [68] combined images obtained from a camera with a filter with arc voltage measurement to control the arc length in the GTAW process. Zhan et al. [69] developed a system of monitoring the wire feeding location and the wire deviation angle by using post-processed images acquired from a color welding camera.

2.3.1.2 Spectral sensing

Spectral sensing uses optical emission spectroscopy to analyze the composition of the welded parts as the elemental information is closely related to spectral signals which are critical information in understanding the physical mechanisms. Spectral sensing is used commonly in both laser AM and WAAM systems. Spectrums that are produced in the WAAM process give abundant information about the metal vapors, arc, and shielding gases which are closely related to defects in the WAAM process. Huang et al. [70] developed a method of diagnosing and detecting porosity defects by real-time acquisition and processing of spectral data of an aluminum alloy. An SVM classification model along with a genetic algorithm (GA) is utilized to estimate various types of defects related to porosity.

2.3.1.3 Acoustic sensing

Acoustic sensing has proven its potential in its benefits of being a non-destructive and flexible method without the need for direct contact with the welding process. Acoustic emission (AE) from the welding process is analyzed to provide insight into arc conditions, melt pool dynamics, and internal defects such as porosities and cracks. The deposition efficiency can be inferred through the AE signal as well [57], [71]. Bhattacharya et al [72] used AE sensors in combination with currents and voltage sensors with an artificial neural network to predict weld deposition efficiency. Bohemen et al. [73] utilized root mean square values of real-time acoustic signal data to detect martensite formation during steel welding. Despite numerous successes in research of AE in the application of WAAM, there is not as many publications compared to that of traditional GMAW and laser AM.

2.3.1.4 Thermal sensing

Sensing temperature in the welding process is critical as failing to control the thermal energy poses significant variability in the microstructure of the built part, leading to inhomogeneous material properties. Also, the geometry of the built part may deviate from the desired geometry due to the undesired slumping of the deposited material. The thermal data gathered during the manufacturing stage could be useful to analyze and identify potential problems in the workpiece due to high residual stress or defects [74]. Mireles et al. [75] developed a non-constructive method of identifying porosity during the in-situ fabrication stage by utilizing IR images to indicate various defects. Also, in-situ correction strategies were implemented to correct defects detected during the fabrication process.

2.3.2 Control of WAAM process

Most research publications regarding process control in metal AM are related to laser AM and not WAAM. Fathi et al. [76] utilized CCD imaging sensors to study the effects of different process parameters on the resulting deposition height and used system identification techniques to obtain a dynamic model of the laser solid freeform fabrication (LSFF) system. This model was used in traditional proportional-integral-derivative (PID) controllers to show improvement in target tracking of the deposition height. Heralic et al. [77] utilized a camera and a 3D laser scanner to obtain a profile of each layer after every laser metal wire deposition. Through online iterative learning control, the deviation of layer height was adjusted by controlling the wire feed speed for the next deposition layer. Hagqvist et al. [78] utilized the resistance between the nozzle and the substrate during laser AM to acquire the distance between the tool and the workpiece. A feedforward control was used to flatten the sequential layer deposition. Then, a second-order iterative learning control algorithm is used for determining the wire feed rate. Xiong et al. [79] used two CCD cameras to monitor the distance between the nozzle and the printing part, and the width of the printed layer. Band filter lenses and image processing algorithms were used to filter out the intensive torch light. Another common challenge in the WAAM process is to maintain print quality in sharp corners where materials and temperature tends to accumulate. To overcome this challenge, Li et al. [80] used an adaptive process control scheme (APCS) to achieve uniform bead geometry throughout the deposition process. An appropriate wire feed speed is selected depending on various dynamic constraints of different corners in the building toolpath. Xiong et al. [81] established an improved self-learning neuron feedback control of bead width with a visual sensor and its corresponding image processing algorithm. Doumanidis and Kwak [82], [83] used an optical laser scanner and infrared pyrometry sensor to monitor the GMAW system. The obtained data are used for developing a closed-loop geometry control system. With the system, the bead width and height followed the reference values. To compensate for delays in the measurement, a real-time prediction of the deposition model is used. Smith et al. [84] used a CCD camera to capture the image of the molten pool surface and obtained the width of its molten pool. This data was then used in the closed-loop control of a GTAW system as a feedback signal to control weld penetration. Fan et al. [85] implemented feedback control to monitor welding penetration using temperature data. An infrared sensing system monitors the surrounding temperature of the melt pool during a welding process. Liu and Zhang [86], [87] developed a linear-model-based predictive controller to control the penetration or 3D weld pool geometry of a GTAW process. Scetinec et al. [88] proposed an online height controller and toolpath replanning for the fabrication of a metal workpiece. The result showed that varying currents during welding had more impact on the layer height than the voltage, and the fabricated part showed a small deviation from the original CAD model. Dharmawan et al. [89] proposed a reinforcement learning control framework for controlling layer height. The height data of the preceding layer was recorded along with the wire feed speed and the torch travel speed used, and the resulting height of the layer was measured with a laser 3D scanner. This set of data was put into an algorithm to train a model. Finally, the torch travel speed and wire feed rate were adjusted accordingly during the welding process according to the measured height of the preceding layer. Xia et al. [90] developed a model predictive control algorithm to control the deposited bead width. The weld pool images captured by a passive visual sensor with image processing algorithms were used to obtain the width data. The algorithm was tested in simulation and validated through an experiment to show acceptable tracking accuracy and robustness. Mu et al. [91] used real-time PID control and model-predictive control (MPC) to improve width and height fluctuation when building a workpiece.

Although the effort of modeling and controlling the WAAM process had accomplished advancement in control of the WAAM process, there are relevant parameters that were often not considered. For instance, one would optimize bead height but not width. Often one of the process parameters such as the torch travel speed is held constant in a feedback control loop. This calls for the exploration of control algorithms that are more capable handling of a greater number of process parameters efficiently.

3 Experimental Setup

The experimental setup consists of two parts. The first part is the hardware setup and the second is the software-hardware interface setup. Hardware includes the welding system, a gantry positioner, and various sensors. Software and hardware interfacing is required to connect the control system with the WAAM system in a way that the control system can both send and retrieve commands and information from the deposition process.

3.1 Hardware setup

The hardware of the experiments includes setting up the welding machine on a gantry system with various sensors such as a profiler and IR camera. The sensors are carefully set up to lend data as accurately as possible to minimize the margin of error. As the sensors are exposed to a large amount of heat radiation and metal spatters, protective equipment is designed.

3.1.1 Welder setup

Wire arc additive manufacturing process requires multiple equipment such as the operation panel, welding machine, wire feeder, cooling system, feedstock wire, welding gun, robot, or gantry system, shielding gas, substrate and more, as seen in Figure 3.1.

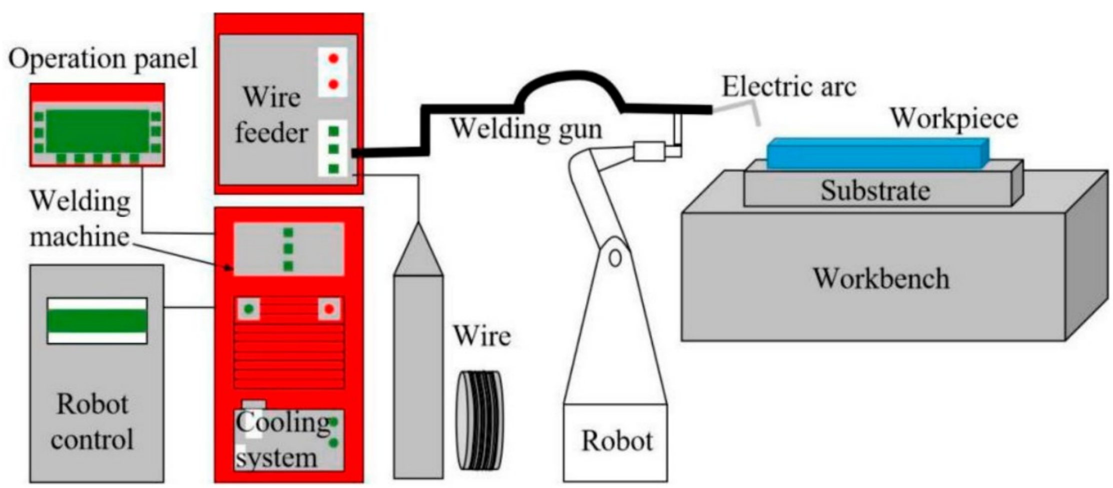

Figure 3.1 Schematic diagram of WAAM-CMT equipment with a robotic manipulator [92]

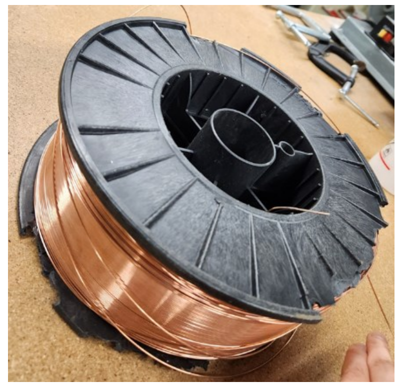

Figure 3.2 Fronius TPS 5000 CMT welding supply fully integrated with 3 axis gantry system with FK4000 cooling unit and VR-7000 wire-feed unit (left) that feeds ER70S-6 copper coated feedstock wire (right)

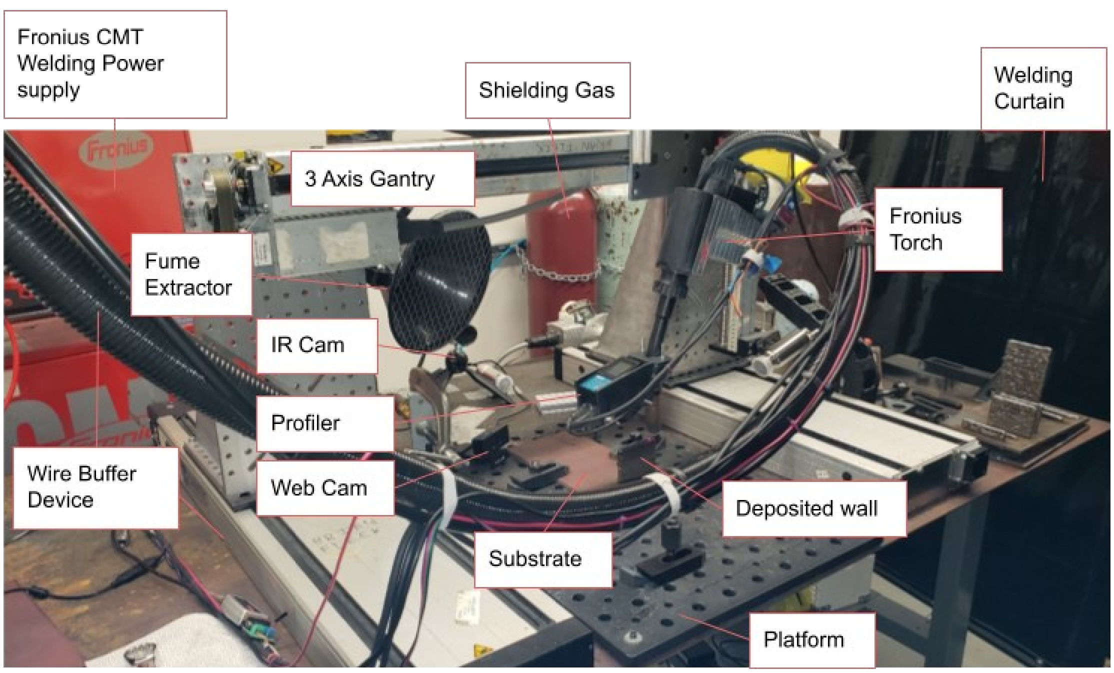

Figure 3.3 Schematic of the CMT wire arc additive manufacturing system with sensors

3.1.2 Gantry System

The gantry system refers to a motion-centric system designed for multi-axis operation. It is custom designed and hand-built including the worktop and the gantry robot. There are two Dantec heavy-duty stepper motor sliders for the first axis. Another stepper motor slider is mounted perpendicular with brackets to the two stepper motors to create another axis. Finally, another slider equipped with the Fronius torch mounting adapter is attached to create the third z-axis. The kinematics and the visual model of the gantry system are built in the ROS environment for simulation, enabling collision detection before commencing with gantry system operation using a custom G-code.

3.1.3 Profile sensor

The model of the profilometer utilized in the experiment is SICK PRO2-N100B25A1. It is capable of high-precision measurements by emitting a band-shaped laser beam and using a light-plane-intersecting method that triangulates the reflected light. The reflected light from the emitted band-shaped laser beam is received by the CMOS light receiving unit and the profile is obtained using the resulting image data. The schematic diagram of the profiler measurement can be seen in Figure 3.4. It has a measuring distance that ranges from 75 mm to 125 mm away from the light emitting unit and measuring width ranging from 17 mm to 27 mm. The z-axis resolution is 2 µm and the x-axis resolution is 25 µm with measuring distance of 75 mm. It uses RS-485 serial communication with a laser class of 2. The profiler was mounted on an instrumentation rig that was attached to the neck of the torch. This setup enabled in-situ monitoring of each layer of bead deposited.

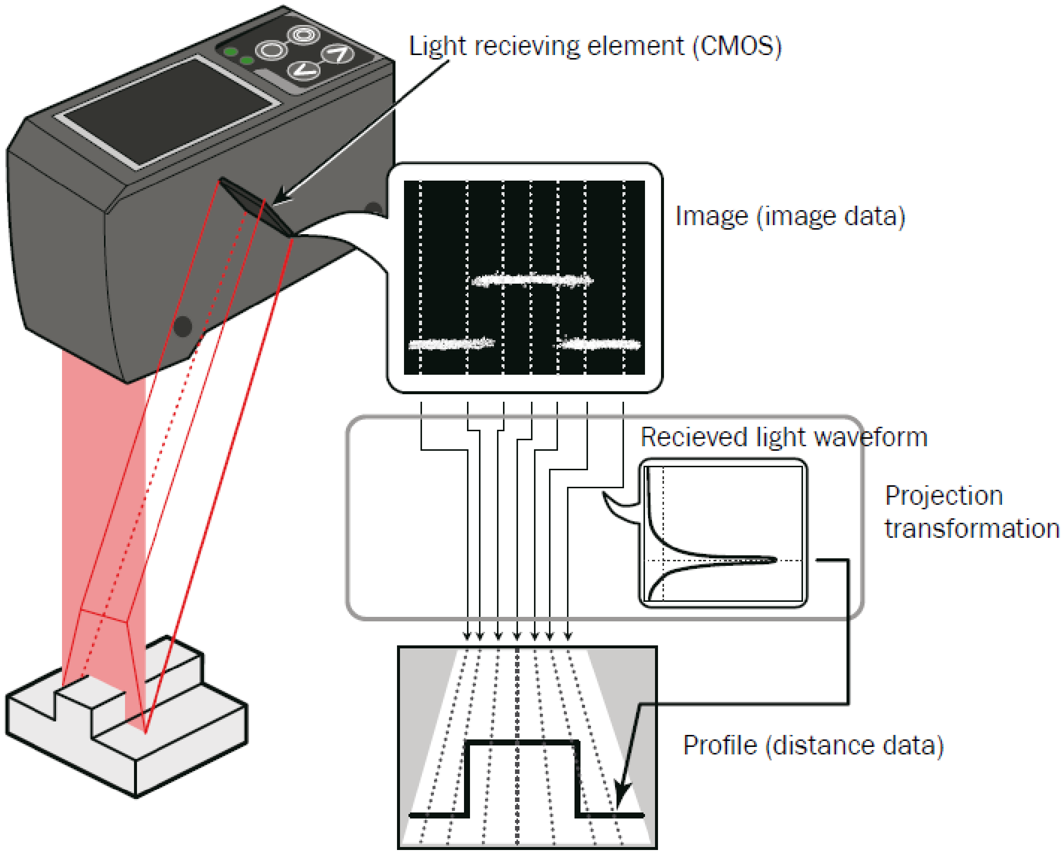

Figure 3.4 . Schematic diagram of the SICK profilometer measurements [93]

Figure 3.5 Top view of mounted profiler with graphical user interface displaying the profile of the bead on the substrate

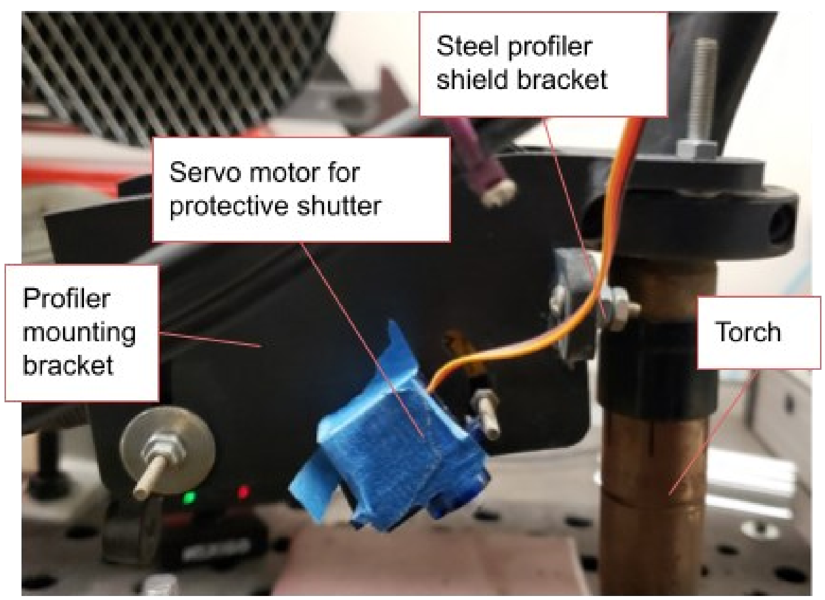

.

Figure 3.6 Sideview of the profiler with accessories attached

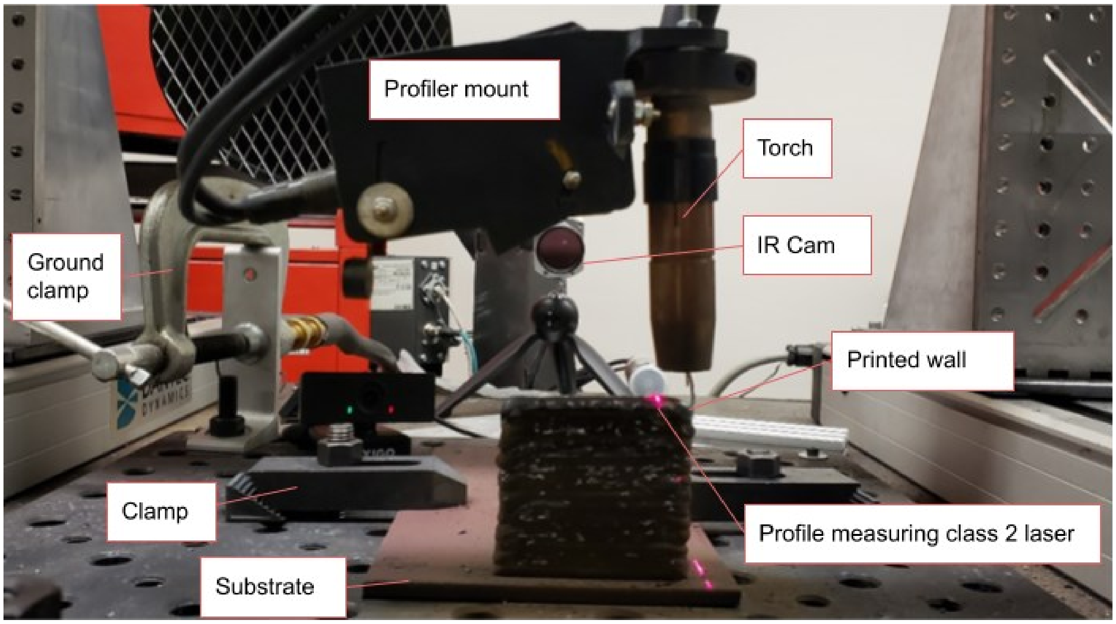

Figure 3.7 Front view of the schematic of the CMT wire arc additive manufacturing system with sensors

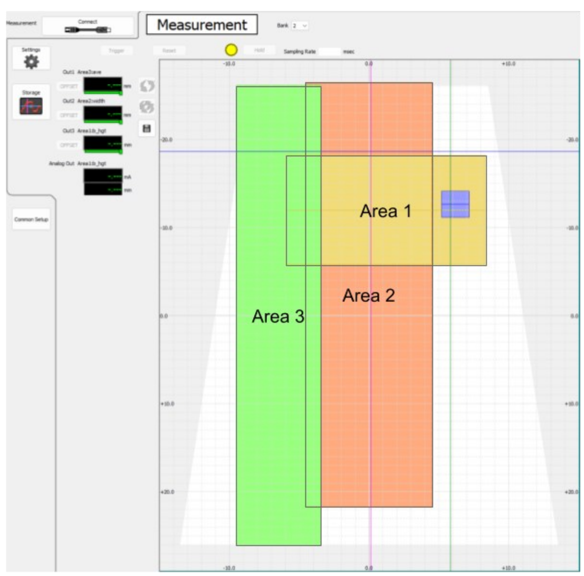

Figure 3.8 Screenshot of profiler configurator, PRO2 Navigator graphic user interface with various measuring areas. Area 1 and 2 were used to obtain width and height of the profile.

The profilometer comes with configurator software with a graphic user interface (GUI) allowing users to conveniently modify camera capture settings and output data as seen in Figure 3.8. The various areas indicated in the PRO2 Navigator GUI may be adjusted in dimensions and locations to lend various information from the obtained profile data, such as width, height, and radius of the profile.

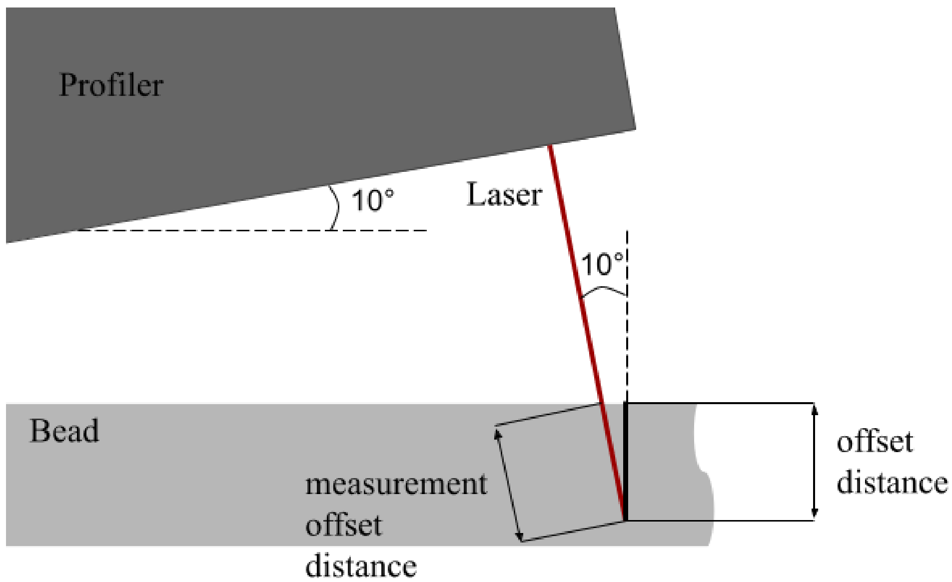

Figure 3.9 Schematic side-view diagram of profiler measuring bead at an inclination of 10°

As the profiler uses the reflection of a laser to acquire profile data, careful tuning of the camera setting is required when measuring the shiny surface of the deposited metal bead. To alleviate the effects of reflection from the surface of the bead, the shutter time, high dynamic range (HDR) shutter time, and gain setting was tuned to 300 μs, 8500 μs, and 1.00, respectively through the GUI. The mode was set as HDR. Additionally, the profiler bracket was designed such that the mounted profiler is inclined at an angle of 10 degrees to avoid unwanted reflections as much as possible. The profiler was mounted to the neck of the torch, enabling an in-situ measurement of the deposited bead as shown in Figure 3.6 and Figure 3.7.

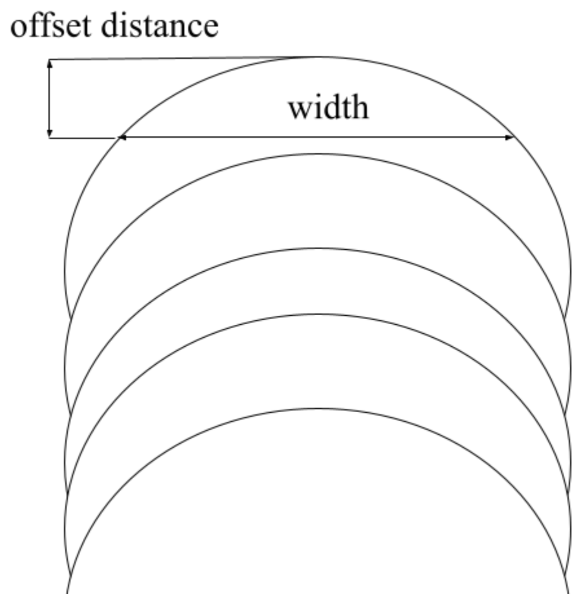

Figure 3.10 Cross-sectional view diagram of deposited beads where the bead width is determined through an offset distance away from the peak

Figure 3.9 and Figure 3.10 display the schematic diagram of the profiler measuring the bead's geometry. The value of width is extracted from this profile. The width of the profile is determined as the length of a horizontal chord across the top profile. The chord is generated at a fixed offset distance of 1mm below the peak of the bead as depicted in Figure 3.10. Since the profiler is mounted at an angle of 10 degrees, the following trigonometrical calculations were performed to calculate the offset distance apparent on the PRO2 Navigator GUI:

$$measurement\ offset\ distance = \frac{offset\ distance}{\cos 10°} \tag{1}$$

With the measurement offset distance set at 1.015mm in the PRO2 Navigator GUI, the obtained width data is published to the control algorithm at a rate of 30 Hz. With a given range of torch travel speed of 250 to 400 cm/min, the resolution of the measurement is calculated to be ranging from 0.14 to 0.22 mm given the range of the travel speed.

As the start and end condition of the bead suffers from the hardware limitation, namely, delay in the software interface between the Fronius welder driver and the 3-axis gantry system, and acceleration and deceleration of the torch, the geometry quality at the edge of each bead usually does not accurately reflect the input process parameters used. Therefore, only the geometrical values obtained from the middle 85% of the entire length of each bead were used and the geometrical information obtained on the remaining 7.5% on each end of the beads was excluded from the study. Finally, the overall profile of the side of each printed bead was recorded to gathered to visualize and demonstrate the effectiveness of the control technique applied to the WAAM system.

3.1.4 Thermal sensor

A short wavelength IR camera, Optris PI 1M is used to measure the temperature of the printing part in real time for dwell time control. It is suitable for temperature measurements in metal as this IR camera exhibit distinctly higher emissivity at the short measurement wavelength of 1 μm than at the measurements in the conventional wavelength range of 8 ~ 14 μm. It has a fast reaction time of 1ms with a high dynamic CMOS detector with 764 x 480-pixel resolution with temperature measurements ranging from 450 to 1800 °C. The accuracy of the IR camera is $\pm$5.0 °C at room temperature and is $\pm$1% for temperatures under 1400 °C.

An IR camera was set up on a tripod aloof of the location of deposition such that the field of view of the camera captures the entirety of the build process from the first to the last layer. The highest temperature of the bead under the perspective of the camera is obtained and then transmitted to the main controller at a frequency of 10 Hz. When the controller receives the temperature data that is below a specified threshold, the dwell time is signaled to end to resume the deposition process of the following layer.

Figure 3.11 Isometric view of Optris PI 1M IR camera [94]

Figure 3.12 IR camera mounted on tripod perpendicular to direction of deposited wall

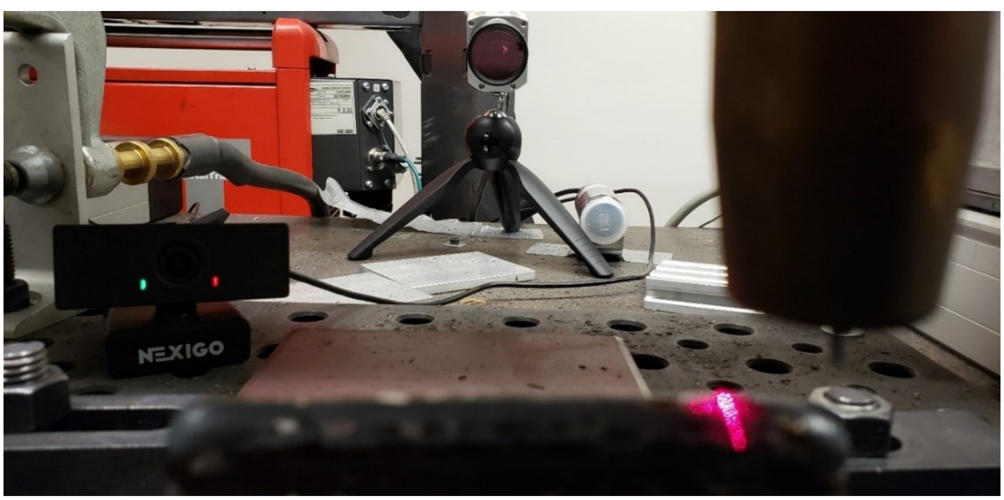

Figure 3.13 IR camera field of view aimed to the entirety of printing wall

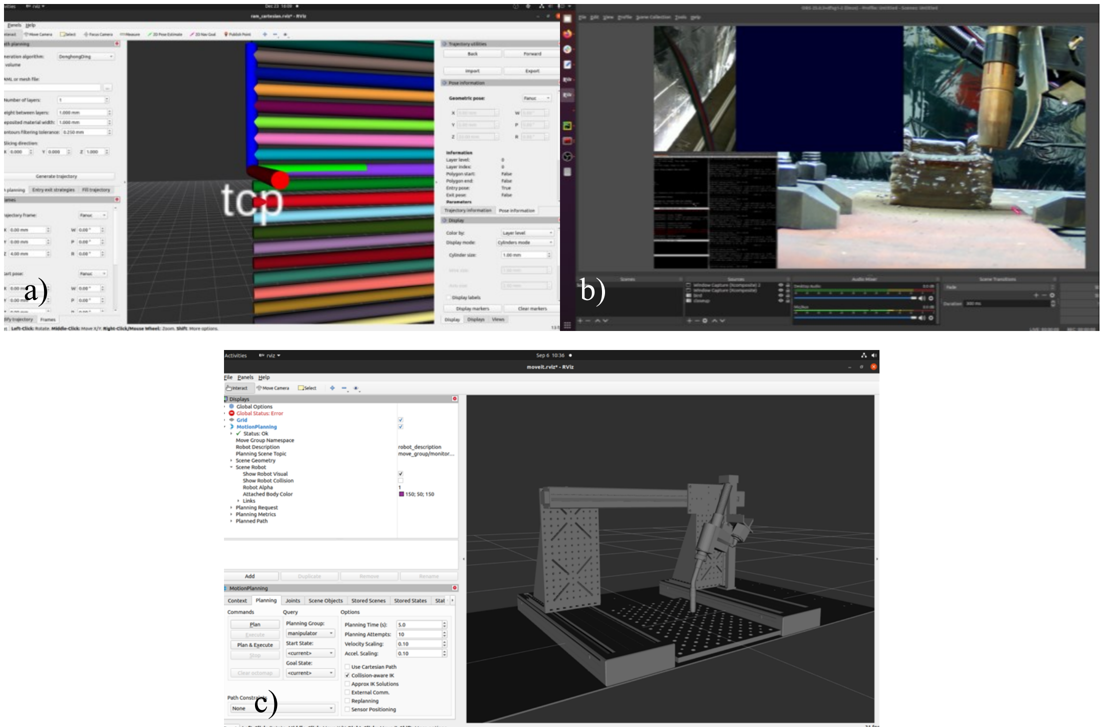

Figure 3.14 ROS integrated control and monitoring system screenshot on PC. a) decomposed trajectory toolpath simulation b) weld visual and thermal monitoring and control screen being recorded c) welding machine collision detection

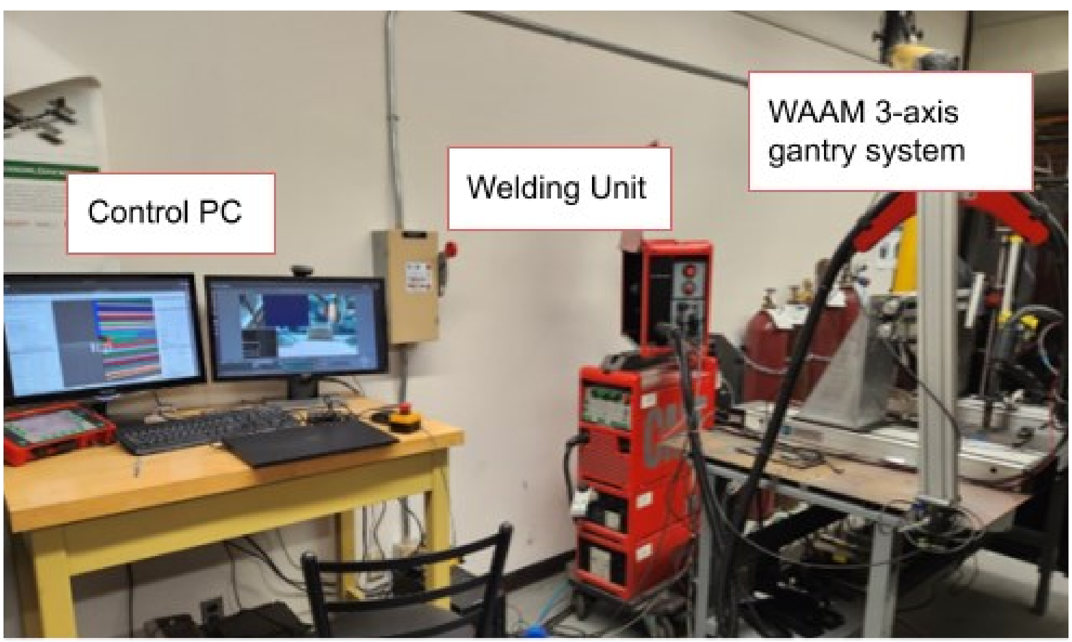

Figure 3.15 System setup showing control PC, welding unit and the gantry system

3.2 Software Hardware Interface

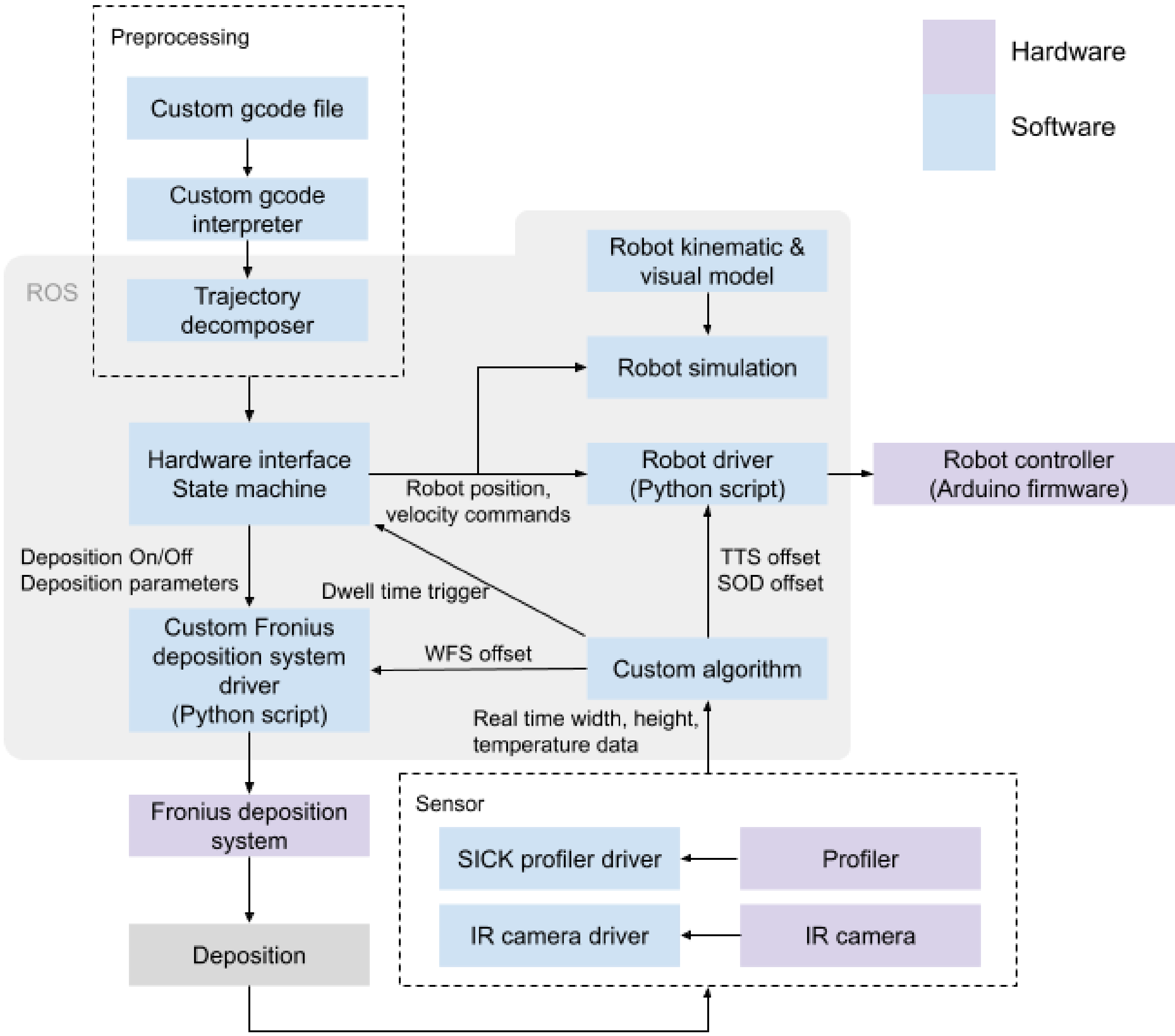

Figure 3.16 System flow diagram of the algorithm aided WAAM control process

The software and hardware interfacing framework are designed to interface the software side of the control system with the hardware side of the WAAM system. Figure 3.16 illustrates the software-integrated WAAM process, starting from the preprocessing stage where a custom G-code is manually inputted to create a desirable shape of the deposited part which is used to command the robotic gantry system to coordinate its torch. Then the hardware interface state machine and the custom Fronius deposition system driver that is wrapped in Robotic Operating

System (ROS) sends the signal to the physical hardware such as the robot controller and the Fronius deposition system to change robot position, velocity and to turn the material deposition on and off. As the deposition creates a bead or a part on the substrate plate, the profile and the thermal data are collected by the sensors such as the profiler and the IR camera. The collected data are fed into the custom algorithm which has the capabilities to take intelligent actions. Torch travel speed and standoff distance offset can be sent from the custom algorithm to the robotic system. Dwell time triggering, or a triggering action to commence on building another layer after the previously deposited bead has been cooled down to a threshold temperature can be sent by the algorithm. Furthermore, the algorithm can send the wire feed speed offset as well to alter the wire feed speed.

3.2.1 Software to hardware ROS interface

G-code, also known as RS-274 is a widely used CNC programming language used widely in CAD to control automated machine tools like the 3-axis gantry system. G-code consists of a sequence of instructions for the machine controller to tell the motors where to move and how fast to move. As the traditional method of creating a G-code does not allow speed and coordinate adjustments in real-time, a custom G-code interpreter had to be designed along with manually typed custom G-codes. A trajectory decomposer converts the G-code instruction to signals compatible with ROS. Within ROS, robot kinematic and visual model helps robot simulation to check the collision of welding parts. Also, ROS contains the custom developed algorithm which is used to interact with data gathered from various sensors, and the algorithms can send various output signals to the welding system and the gantry system such as torch travel speed offset, standoff distance offset, dwell time trigger and wire feed speed offset in real-time. On the side of the gantry system, GRBL firmware installed Arduino receives the signal from the custom G-code interpreter to control each of the stepper motors via stepper motor drivers according to the inputted custom G-code instructions from the PC connected by a USB type A port. The physical setup of the stepper motor drivers and the Arduino can be seen in Figure 3.17.

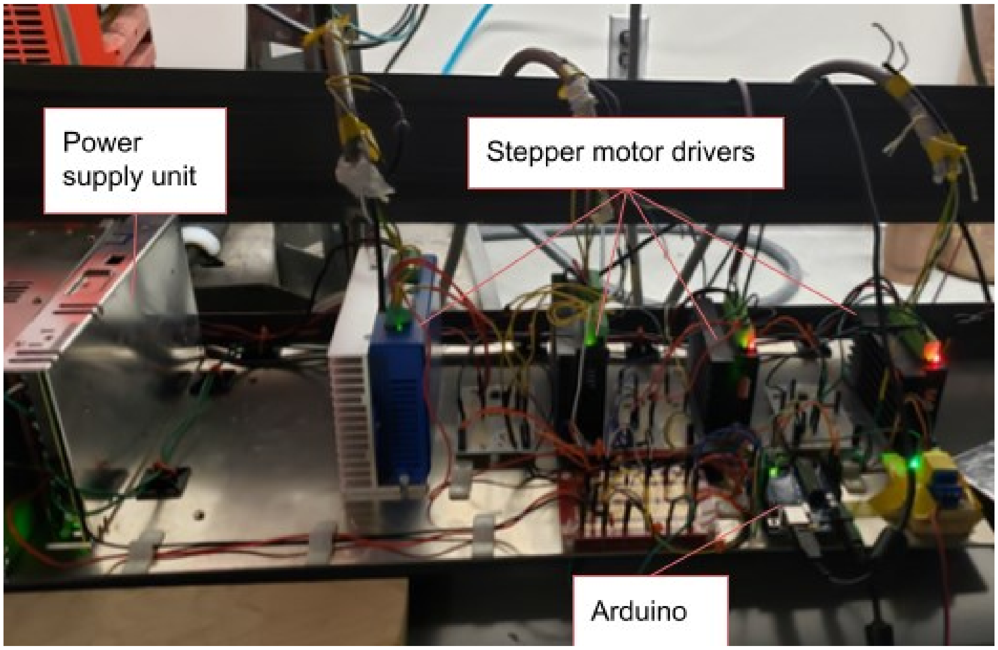

Figure 3.17 Stepper motor drivers and GRBL firmware installed Arduino setup for gantry system, under the welding platform

3.2.2 OpenAI Gym

OpenAI is a convenient toolkit for developing and testing various machine learning and reinforcement learning algorithms. OpenAI gym provides an interface for users to create their own environment on which the algorithms can be tested. However, as the WAAM experiment is carried out in a real-world scenario, the environment seen and the actions taken by the algorithm are interfaced with the physical hardware such as the Fronius torch controller, 3-axis gantry system, profiler, and the IR camera.

To utilize a variety of algorithms provided by OpenAI, reset and step functions are required. First, the reset function is responsible for setting the environment back to the initial state. For example, in the scenario of the WAAM process, the reset function would be called when an entire layer is finished, as indicated by the returned values of the step function. Then the WAAM system would go on to the next empty space on the substrate plate where other layers would be printed for purpose of the initialization of first layers. Next, the step function is a function at which an agent in an environment gets to take an action, observe the consequence, and return information on if the episode is in a terminal state at which the reset function is called, and the reward received for that timestep. In the case of the WAAM system, here is where the command of changing the wire feed speed and torch travel speed would occur. Completion of the OpenAI setup enables the use of state of art algorithms for the experiment.

4 Methodology

Given various sensors streaming real-time data of the environment and a ROS enabled systems that read them and allows online control of manufacturing process parameters, various algorithms were considered for deployment to optimize deposited bead geometry. Q-learning, multi-objective policy gradient reinforcement learning, and inverse supervised learning control techniques were examined. Simulation for each of the algorithms were performed followed by the actual experiments. Results were analyzed and the most rational algorithm is determined.

4.1 WAAM as Reinforcement Learning Markov Decision Process Framework

MDP is a discrete-time stochastic control process that provides a mathematical framework for modeling decision-making. Every reinforcement learning problem needs to be in the form of MDP. The agent-environment interaction in MDP is shown in Figure 4.1.

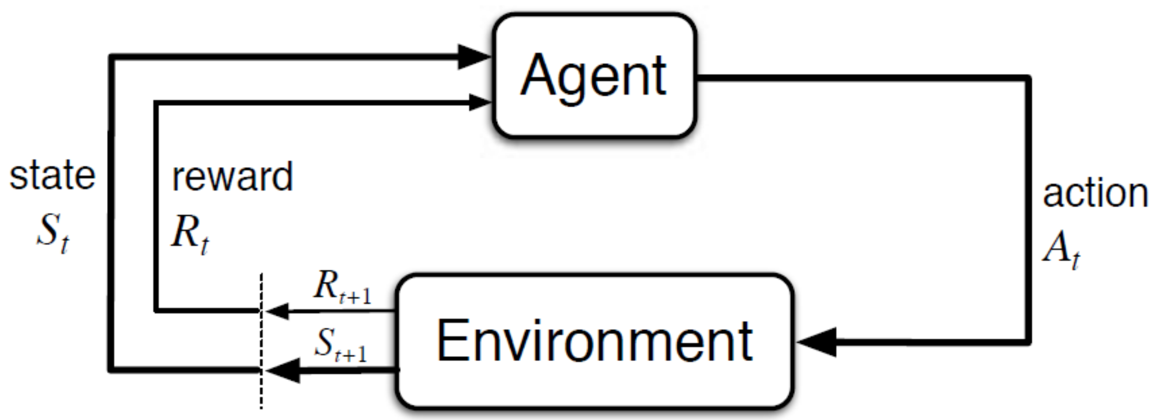

Figure 4.1 Agent-environment interaction [51]

MDP is formulated by tuple of four elements (s, a, p, r).

- State, s

  The observation that the agent receives from the environment is defined as a state. An example of a state in WAAM can be the temperature at which the bead is currently at during the welding process. It also can be the geometrical data of the bead that the current welding is occurring on top of.

- Action, a

  Action is a decision commanded by the agent or the main controller to control the environment. Examples of actions in WAAM include changing wire feed speed, torch travel speed, standoff distance between the torch and the bead, current, and voltage.

- Transition probability, p

  The transition probability is a probability of a state evolving to the next state given the agent taking an action.

- Reward, r

  The reward is obtained at every timestep, and it is a value that is calculated based on how good the next state is after the agent has taken an action in a given state. For example, in WAAM, the agent will receive reward based on how well the bead is printed.

These four elements will continue in a cycle until the state reaches a terminal state, which marks an end of an episode. The terminal state in the case of WAAM in building a multi-layer single-track wall can be the state at which the number of bead layers deposited in building the wall has reached its predefined maximum and cannot deposit layers further on top. At this point, the learning process may be stopped, or continue by resetting the environment and proceeding to build more multi-layer single-track walls.

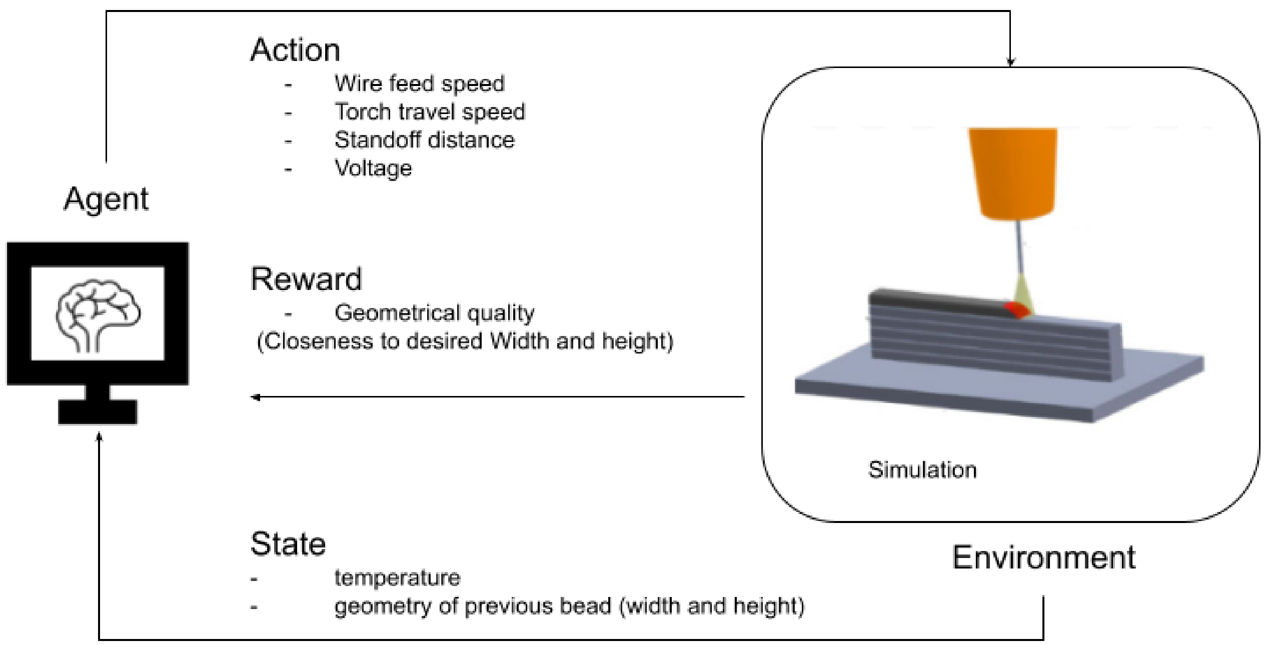

Figure 4.2 Agent-environment interaction scenario in WAAM process

4.2 Q-learning

Machine learning algorithms were utilized for the study of in-situ control of the WAAM system. They include Q-learning and policy gradient algorithm. The first reinforcement learning algorithm used is called Q-learning [95], also known as a model-free off-policy temporal difference method. It is model-free as it does not require any information of the environment. It is off-policy because the policy updated is different from the behavior policy. The term temporal difference means that the algorithm attempts to predict future rewards or value in a sequence of states. The control algorithm is applied to the WAAM system to iteratively learn the set of values for each of the various process parameters to achieve a specified geometrical quality. After the algorithm converges with the Q-learning method, the system can effectively identify what set of action is best for the system to deploy in a real-time manner in a single-track, multi-layer printing scenario. The major advantage of the method is that it can adjust wire feed rate, torch standoff distance, torch travel speed, and voltage in accordance with real-time sensory information from a profilometer and an infrared camera to achieve specified geometrical quality.

Q-learning is one of the most well-known and employed RL algorithms that belong to the class of off-policy methods as convergence is guaranteed for any agent's policy [51].Algorithm is considered converged when the learning curve becomes flat and no longer improves. The basis of Q-Learning stems from a concept of *Quality Matrix* or Q-Matrix. With a matrix size of $N \times Z$ where N is the number of possible states and Z is the number of possible actions that can be taken by the agent, the state action space $S \times A$ is discrete. The Q-Matrix is populated with Q-values that represent "how good" is it to take specific action given the current state. Algorithm 1 summarizes the general Q-learning method.

4.2.1 Q-learning Algorithm

The algorithm begins with initialized Q-matrix with random values and is updated using the Bellman optimality equation (2).

$$Q^{new}(s_t, a_t) = Q(s_t, a_t) + \alpha[R_t + \gamma \max_a Q(s_{t+1}, a) - Q(s_t, a_t)] \tag{2}$$

Variables in (2) are defined as,

- s_t and s_{t+1}: current and next state of the observed environment, where $s_t \in \mathbb{S}$ and S is the set of possible states.
- a_t and a_{t+1}: current and next action taken by the agent, where $a_t \in \mathbb{A}(\mathbb{S}_t)$ is the set of possible actions given state.
- γ: discount factor $\gamma \in [0, 1]$. Defines how much of future rewards are taken into account instead of the immediate rewards.
- α : learning rate, $\alpha \in [0, 1]$. Defines extent of newest knowledge replacing the older one.
- R_t: numerical value of an immediate reward, a consequence of the action, a taken.

Algorithm 1. Q-learning method [95]

Set algorithm parameters: α, γ

Initialize the Q-matrix, $Q(s, a)$ for all $s \in \mathbb{S}$, $a \in \mathbb{A}$, arbitrarily

Repeat for every episode:

Initialize s

Loop for each step of episode:

Choose a_t from s_t with a set policy derived from Q (use ϵ-greedy)

Take action a_t and observe reward, R and next state s_{t+1}

$Q(s_t, a_t) \leftarrow Q(s_t, a_t) + \alpha[R_t + \gamma \max_a Q(s_{t+1}, a) - Q(s_t, a_t)]$ (update Q-matrix)

$s_t \leftarrow s_{t+1}$

until s_t is terminal

The type of Q-learning deployed here is specifically a ϵ-greedy Q-learning. ϵ-greedy method is a simple probabilistic exploratory technique commonly used in RL. ϵ is an exploration probability that represents a value in the range of $[0, 1]$ at which if a randomly generated number between that range falls under, the agent takes a completely random action given a state. Otherwise, it will take a best-known action. This method explained in (3) allows balancing of exploration and exploitation.

$$a_t = \begin{cases} \max Q_t(a), & with\ probability\ 1 - \epsilon \\ any\ action, a & with\ probability\ \epsilon \end{cases} \tag{3}$$

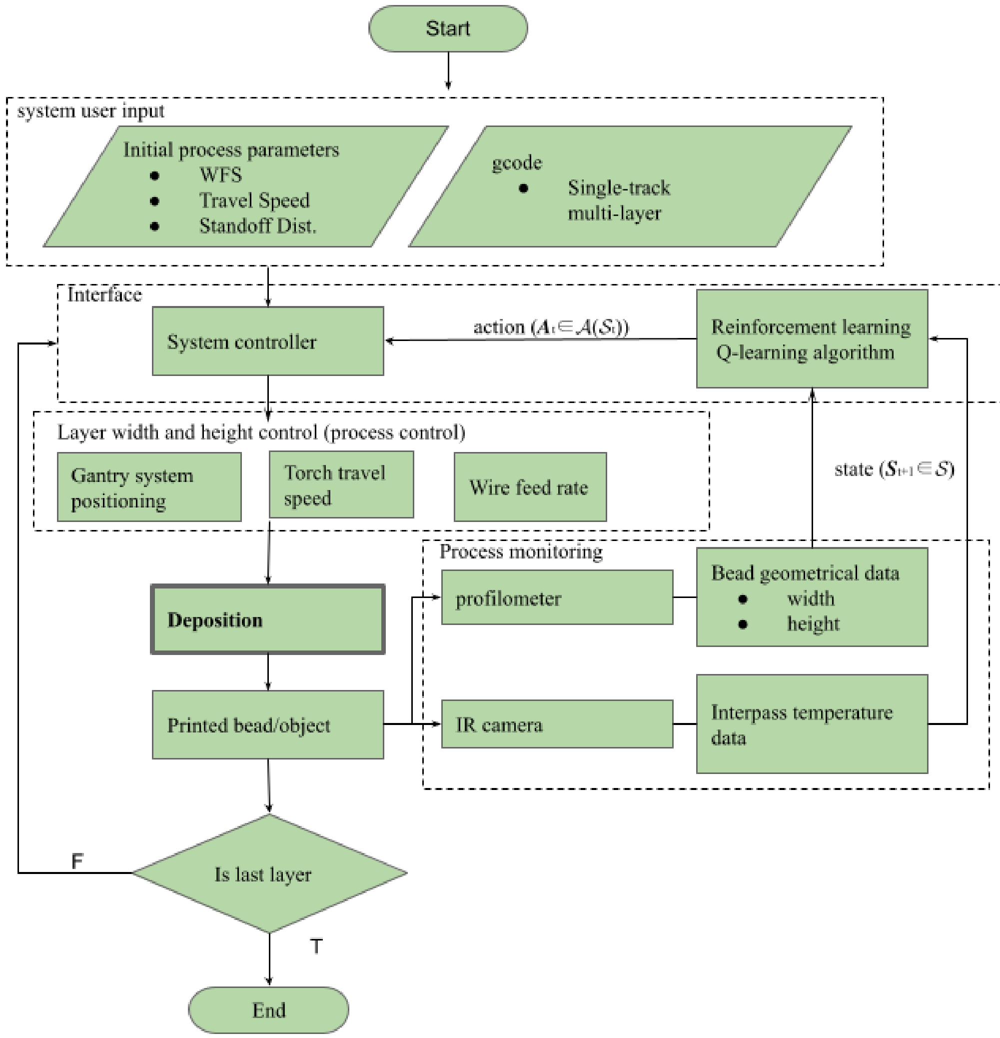

Figure 4.3 Flow chart of Q-learning implemented WAAM process integrated with process monitoring sensors

4.2.2 Q-learning algorithm implementation in WAAM

The conceptual idea of reinforcement learning is translated into implementation in WAAM of single-track multi-layer walls. Figure 4.3 demonstrates the flowchart of the system with the incorporation of the RL algorithm. The state of the environment corresponds to the real-time observation data from a profilometer and an IR camera. The profilometer measures the width and height of the bead that the deposition occurs at. Also, the IR camera provides the temperature data at the point of the deposition. The thermal and geometrical data of the previous layer largely affects the geometry of the next layer. With the two data combined, the agent is to take a corresponding optimized action of changing wire feed speed, torch travel speed, and torch standoff distance to specific values that would ultimately give the desired geometry of the next layer and the next and so forth. Every deposition of layer is a step in an episode. As the Q-learning algorithm works with discretized values, Table 4.1 and Table 4.2 are tabulated to show the equispaced and discretized values of various states and actions considered in this study. The third column represents the count at which an range is discretized into. For example, in Table 4.1, the temperature at deposition has range of [500, 700] with discretized counts of 5 therefore, the state is discretized to 500, 550, 600, 650, and 700 $°C$.

Table 4.1 State or observed process parameters discretized within a specified range

State	Range	Discretized into counts of
Bead width at deposition point [mm]	[6, 14]	3
Bead height at deposition point [mm]	[2, 4]	3
Temperature at deposition [C°]	[500, 700]	5

Table 4.2 Action or process input parameters discretized within a specified range

Action	Range	Discretized into counts of
Wire feed speed (WFS) [m/min]	[2, 3]	5
Torch standoff distance (SOD) [mm]	[10, 13]	3
Torch travel speed (TTS) [cm/min]	[25, 35]	5

The first layer is deposited with a commonly known process parameter and the profilometer mounted behind the torch records the bead profile. The setup can be seen in Figure 4.4. Along with the known temperature and the geometrical profile of the previous layer, or a state, deposition of the next layer commences with specific values of wire feed speed, torch standoff distance, and torch travel speed, or an action. As the deposition of the next layer occurs, the profiler observes the geometrical data of the bead just deposited, given the state information of the previous bead's width, height, and temperature data. The geometrical data of the bead that just deposited is used to calculate the reward,

$$R_t = -|h_o - h_a| - |w_o - w_a| \tag{4}$$

where h_o and h_a represent the desired height and measured the actual height, respectively. w_o and w_a represents the desired width and the measured actual width, respectively. With the reward and through Bellman optimality equation (1), the Q-value can be obtained and tabulated into the Q-matrix of Table 4.2. The Q-matrix is tabulated at every interval where the action parameter changes, and a state observation occurs. The intervals at which action changes and state observation occur are portrayed in Figure 4.4. The process iterates for every episode where the terminal state is determined to be at the point where the $R_t < -0.5$.

Table 4.3 Q matrix

State \ Action	$A_1 = (wfs_1, sod_1, tts_1)$	$A_2 = (wfs_1, sod_1, tts_2)$	…	$A_{75} = (wfs_5, sod_3, tts_5)$
$S_1 = (T_1, w_1, h_1)$	$Q(S_1, A_1)$	$Q(S_1, A_2)$	…	$Q(S_1, A_{75})$
$S_2 = (T_1, w_1, h_2)$	$Q(S_2, A_1)$	$Q(S_2, A_2)$		
…	…		…	
$S_{45} = (T_5, w_3, h_3)$	$Q(S_{45}, A_1)$			$Q(S_{45}, A_{75})$

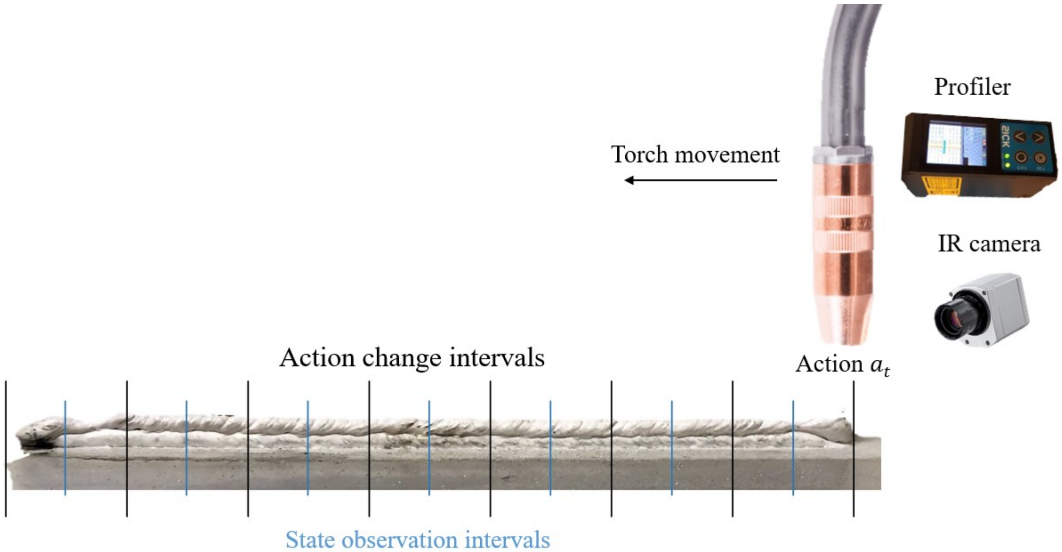

Figure 4.4 Layout of the setup shows that the agents are discretized into sections. An action occurs and the result of the action is observed with the profiler and the IR camera. The observed profile data is used to evaluate the reward.

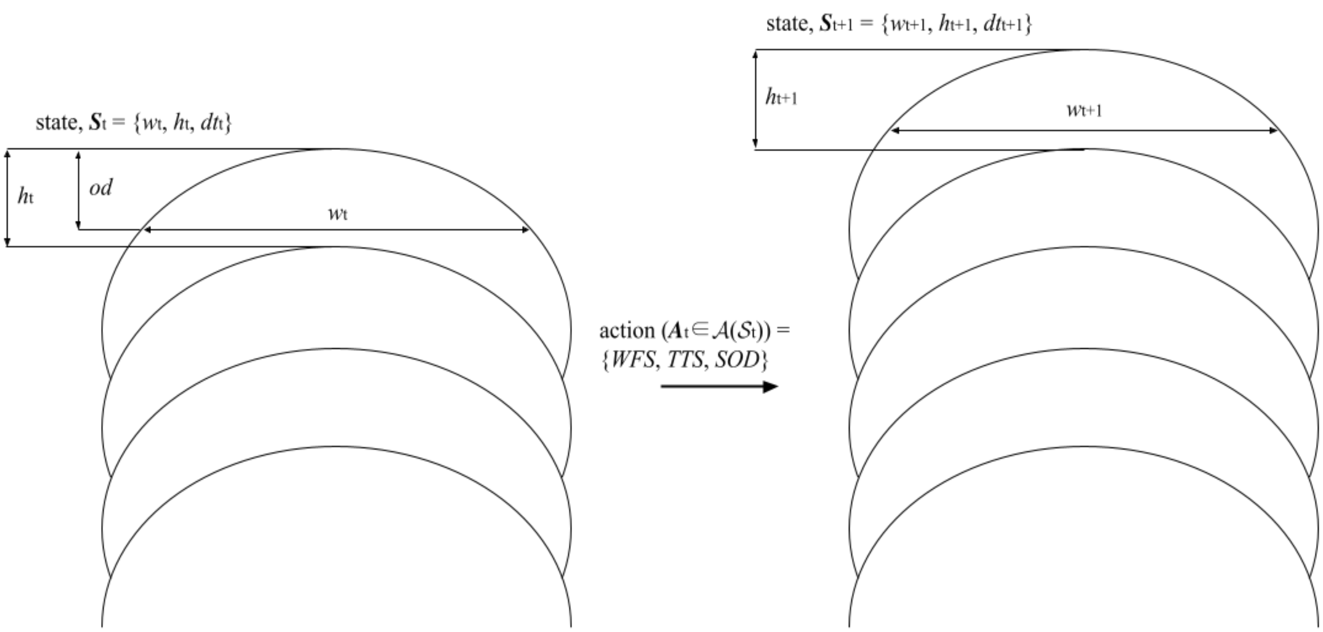

Figure 4.5 State transition displayed by cross-sectional side view of a printed wall

Figure 4.6 Profilometer attached behind and along the trajectory of the print path

The Q-learning method was validated using a simulator before commencing real-world experiments. Second-order regression model [96] was used to map the input parameters, namely the wire feed speed, standoff distance, and torch travel speed, to the resulting width and height of the printed bead. The model is as follows for the prediction of width, W and height, H, respectively.

$$W = 8.9462 + 1.8088R * 0.3621S + 0.1739V - 0.5008D + 0.003556SD + 0.01667VD - 0.1169R^2 + 0.003137S^2 \tag{5}$$

$$H = -0.3514 + 0.4818R - 0.08477S + 0.4028V + 0.01431D - 0.006146RS + 0.001168S^2 - 0.012463V^2 \tag{6}$$

where R, S, V, D represent wire feed rate, torch speed, arc voltage, and standoff distance, respectively. The units are m/min for feed rate, cm/min for welding speed, V for arc voltage and mm for standoff distance. The output temperature data was roughly simulated without an expert modeling equation. The learning rate α, discount factor γ, and exploration probability ϵ, were set at 0.5, 0.99, and 0.1, respectively during the simulation.

4.2.3 Q-learning results

Q-learning was implemented and validated with python codes. The simulation of the experiment was conducted to show the convergence. Figure 4.7 shows that the first episode of learning had an average reward of approximately -75 which corresponds to the summed deviation of width and height from the desired value in units of mm. This deviation is further minimized as the algorithm further tabulates the Q-Matrix. The system, over 30 episodes seem to converge at around a reward of -8.

It is notable in Figure 4.8 that the first episode took an average of 40 steps of episodes or update iterations until reaching the terminal state and quickly down to less than 10 update iterations in the 5th episode. This amount of iteration counts may or may not be a problem depending on how sparse the action change interval is in Figure 4.4 in the real-world experiment. The steady-state error of the resulting graph is occurred due to ϵ, which is fixed throughout the simulation. The major disadvantage of Q-learning is its sensitivity to varying hyperparameters, potentially requiring many training data, perhaps more than the physical limitations of the experiment, for the algorithm to reach the optimal Q-value. As the Q-learning learns a deterministic policy, the agent either chooses the best action or a random action. This could be problematic in a non-stationary environment that is influenced by an unknown disturbance. Also, as the states and actions are discretized, the resolution of the state observed and the actions taken is limited to Table 4.1 and Table 4.2, respectively. The simulation result in Figure 4.7 and Figure 4.8 shows convergence with decreasing amount of the standard deviations with an increasing number of the episode as seen by the shaded region. However, the performance in the physical experimentation had shown poor convergence in optimizing the reward. The agent was not able to quickly reach the terminal state due to the disturbances in the system as anticipated. Also, the poor generalization and the size of the Q-table resulted in taking a long time and iterations of deposition before showing any signs of convergence.

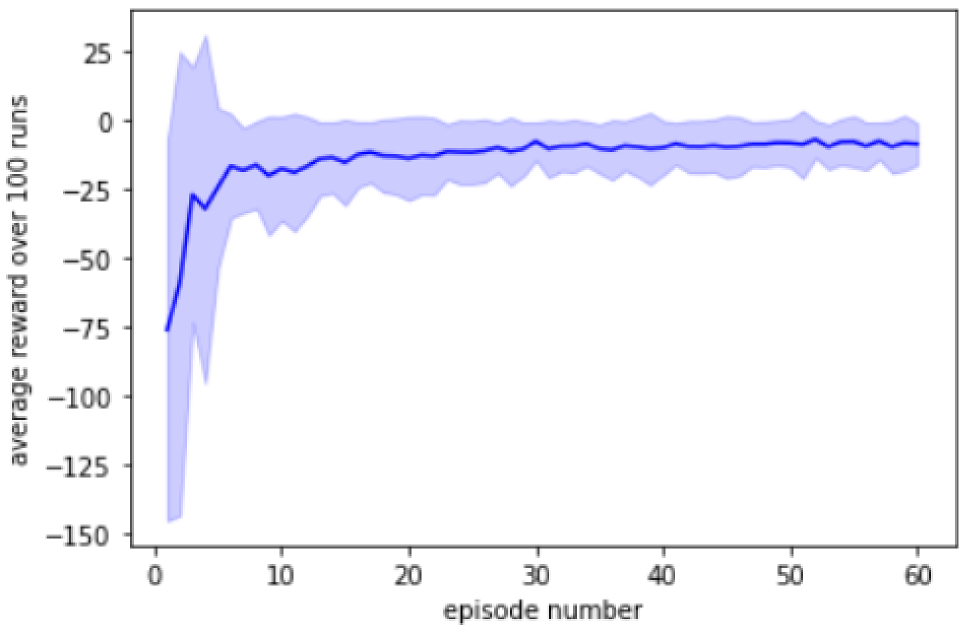

Figure 4.7 Reward obtained with increasing number of episodes averaged over 100 independent runs in simulation environment

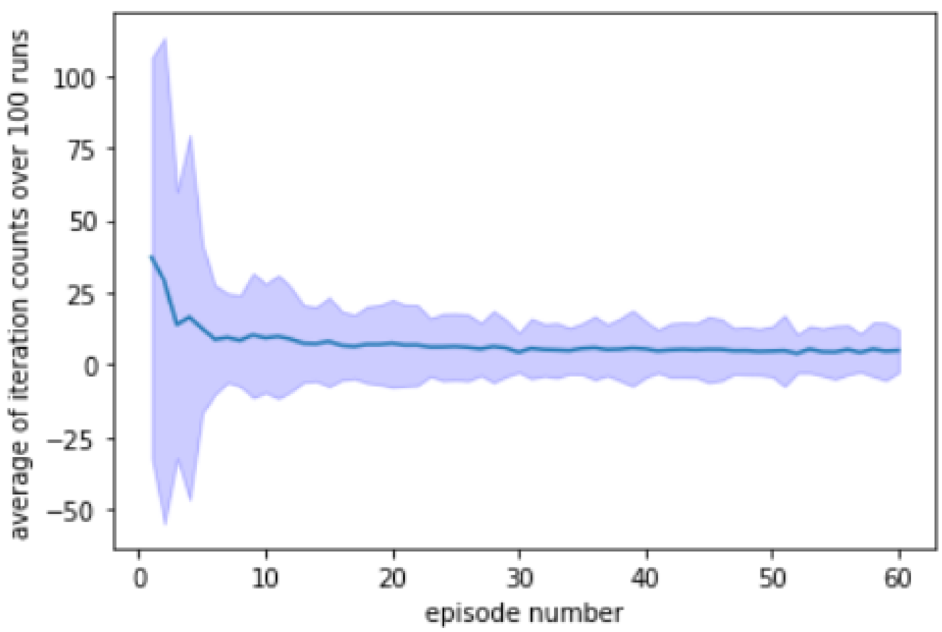

Figure 4.8 Number of update iterations taken to reach terminal state averaged over 100 independent runs in simulation environment

4.3 Policy Gradient

Another algorithm simulated for the WAAM system is a policy gradient method. It is a type of reinforcement learning technique that relies upon optimizing parametrized policies with respect to the expected return by a method of gradient descent. It can optimize both width and height simultaneously, using a multi-criteria objective function [97].

4.3.1 Policy gradient algorithm

Kohl et al. [98] used policy gradient method approach to automatically learn a fast walk on a quadruped robot. The algorithm allowed distributed, efficient policy evaluation, with all learning occurring directly on the robot. A policy gradient algorithm used in the experiment was designed to suit the WAAM optimization process. The policy gradient algorithm for WAAM system uses an initial parameter vector of $\pi = \{\theta_1, \dots, \theta_N\}$ where N represents the number of controllable parameters available for WAAM system, to estimate the partial derivative of the objective function, F in equation (7) with respect to each other. The objective function F is defined to minimize the deviation of width and height of deposited layer given corresponding desired values. The estimation of partial derivative of the objective function is done by evaluating randomly generated policy of t amount $\{R_1, \dots, R_t\}$ near π, such that each $R_i = \{\theta_1 + \delta_1, \dots, \theta_N + \delta_N\}$. Here, δ_j is a value that is randomly chosen between a small, fixed values of $+\epsilon_j, 0, -\epsilon_j$. ϵ_j are relatively small compared to θ_j. The pseudo algorithm can be seen in Algorithm 2.

The neighboring random policies R_i are evaluated with the objective function F, and are categorized into three groups that represent the average evaluated scores for all R_i that had either positive, negative or 0 perturbation in the dimension n. The three groups are summarized as following:

- $Avg_{+\epsilon,n}$ if the n^{th} parameter of R_i is $\theta_{n+\epsilon_n}$
- $Avg_{+0,n}$ if the n^{th} parameter of R_i is θ_{n+0}
- $Avg_{-\epsilon,n}$ if the n^{th} parameter of R_i is $\theta_{n-\epsilon_n}$

These average evaluated scores provide estimation of the benefit of switching the n^{th} parameter, θ_n by $+\epsilon_j$, 0 , or $-\epsilon_j$. An adjustment vector A has size of n is calculated where $A_n \in$

- 0 if $Avg_{+0,n} > Avg_{+\epsilon,n}$ and $Avg_{+0,n} > Avg_{-\epsilon,n}$
- Otherwise, $Avg_{+\epsilon,n} - Avg_{-\epsilon,n}$

A is then normalized by dividing by the Euclidean norm, then multiplied by a scalar adjustment factor η. Then the resulting vector A is summed with the policy π and these steps are repeated in iteration until the evaluated value of the objective function becomes satisfactory, as inputted by the user. The following shows the pseudo code for the policy gradient algorithm.

Algorithm 2 [98]

$\pi \leftarrow$ *Initial Policy*
While !done **do**
  $\{R_1, \dots, R_t\} = t$ random perturbations of π
  Evaluate $\{R_1, \dots, R_t\}$
  for $n = 1$ to N **do**
    $Avg_{+\epsilon,n} \leftarrow$ average score for all R_i that have a positive perturbation in dimension n
    $Avg_{+0,n} \leftarrow$ average score for all R_i that have a zero perturbation in dimension n
    $Avg_{-\epsilon,n} \leftarrow$ average score for all R_i that have a negative perturbation in dimension n
   If $Avg_{+0,n} > Avg_{+\epsilon,n}$ and $Avg_{+0,n} > Avg_{-\epsilon,n}$ then
    $A_n \leftarrow 0$
   else
    $A_n \leftarrow \mathrm{Avg}_{+\epsilon,n} - Avg_{-\epsilon,n}$
   end if
  end for
  $A \leftarrow \frac{\mathrm{A}}{|\mathrm{A}|} \times \eta$
  $\pi \leftarrow \pi + \mathrm{A}$
end while

The objective function is set up such that the system will optimize the bead geometry. The components that constitute the objective function are the following:

1. M_w - The normalized width deviation from the desired width
2. M_h - The normalized height deviation from the desired height

The above components produce the following objective function:

$$F = 1 - (W_w M_w + W_h M_h) \tag{7}$$

All normalized components are multiplied with the user-inputted weight factors of W_w and W_h, respectively. The sum of the weights is constrained to be equal to 1. The distribution of weights determines how much importance is given to each of the optimization criteria of width and height. For example, if the optimization of width is more important than that of the height, W_w will be greater than the other weights. F is the score for the objective function.

4.3.2 Policy gradient result

To evaluate the performance of the policy with specific parameterization, a second-order prediction model of the WAAM process is used like the Q-learning method. The model can be found in equation (5) and (6). The step size η was set as 2, values of ϵ for standoff distance, wire feed speed, torch travel speed and the voltage were set as 0.2, 0.2, 0.5 and 0.5, respectively. The weight factors, W_w and W_h were both set as 0.5. 6 random perturbations of policies, π or simulated deposition iterations were performed per single main while loop of the algorithm.

As seen in Figure 4.9, the objective function score, F showed improvements with an increasing number of iterations, sharply increasing to 0.615 at approximately 50 to 60 iteration counts or number of deposition and then converging to a score of approximately 0.625 after around 450 iterations of deposition. It can be seen from Figure 4.10 and Figure 4.11 that the deviation in width was lowering faster than that of the height, both converging to a deviation of approximately 0.5 mm in 50 iterations and 350 iterations for width and height, respectively.

This method in real-world experiments showed poor results and did not show an increment of score in building a multi-layered wall as this method does not take into account the effect of the previously deposited layer's condition. The previously deposited layer's condition had a significant impact on determining the quality of the next layer in terms of geometry. For example, the high temperature of the preceding layer will likely cause the next layer to slump, and the large width of the preceding layer will consequently make the next layer to have a larger width for the next layer. Due to this inconsistency of iteration starting condition, the algorithm did not successfully learn how to create a multi-layer wall with high geometrical accuracy. However, the algorithm is very suitable for learning to print a single-layer wall if the substrate condition is consistent throughout the learning iterations.

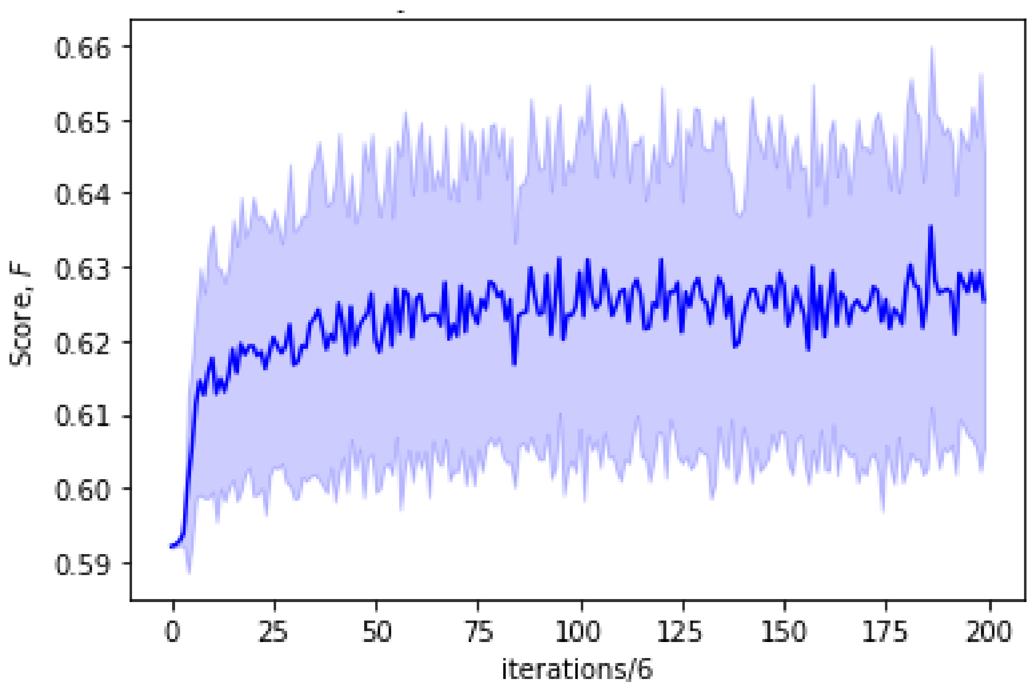

Figure 4.9 Objective function score as a function of iterations in simulation

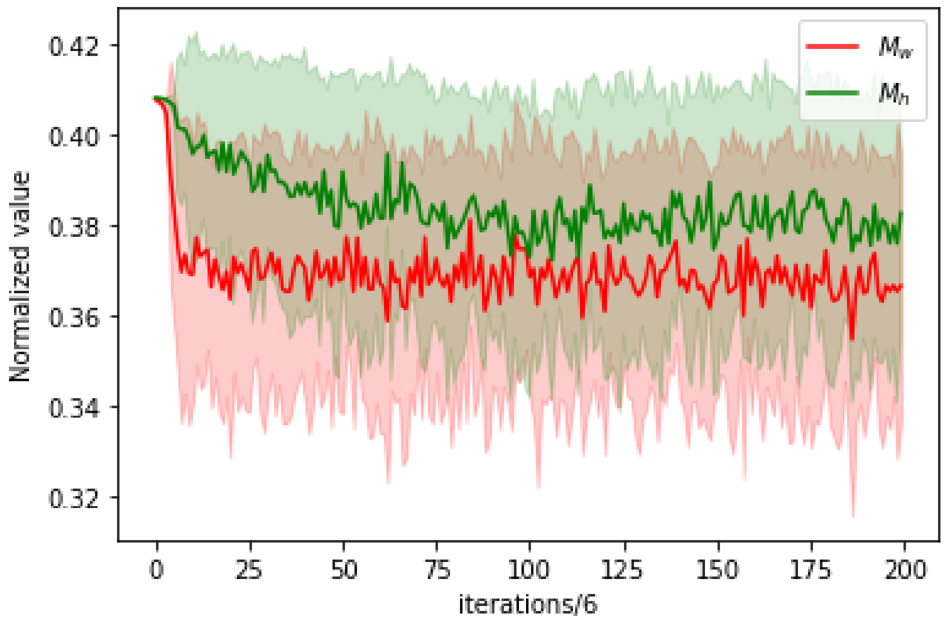

Figure 4.10 Normalized width and height deviation values averaged every 6 randomly perturbed runs as a function of deposition iterations in simulation

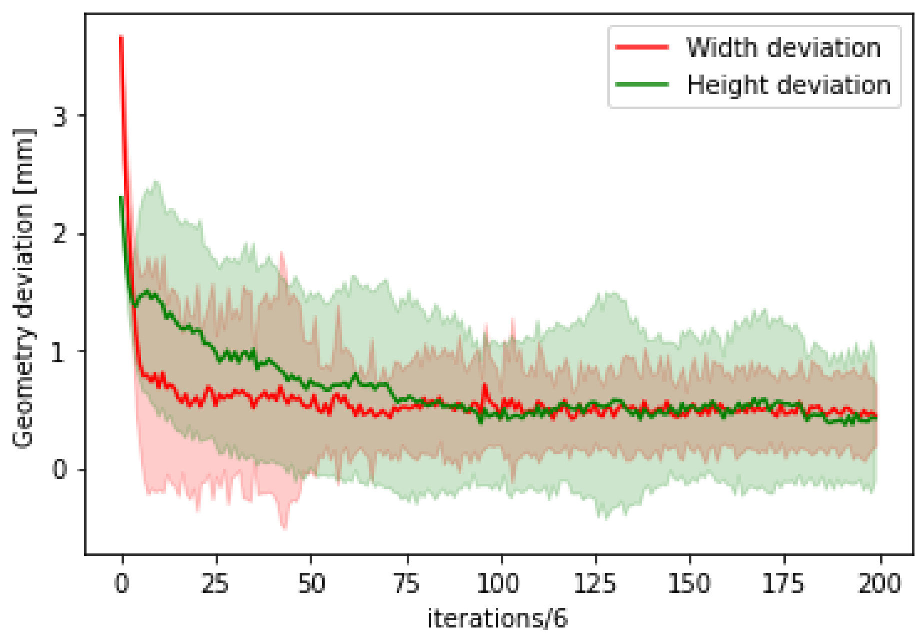

Figure 4.11 Geometry deviation averaged every 6 randomly perturbed runs as a function of deposition iterations in simulation

4.4 Reinforced inverse supervised learning control

To find the optimal wire feed speed and torch travel speed to output desired layer width and height, a supervised learning inverse control algorithm framework is applied. The method of supervised learning functions well with sufficient collected data which had already been collected, amounting to approximately 700 deposited layers after the experimentations for the previously mentioned algorithms, namely Q-learning and policy gradient method.

The term inverse refers to the idea of inputting the desired output first into the system instead of the traditional method of providing input first to a neural network to obtain the output. In the case of WAAM, desired width and height in input to the system to obtain optimal action parameters, namely the wire feed speed and the torch travel speed, instead of inputting the wire feed speed and torch travel speed to obtain layer width and the layer height. It is reinforced to an extent where the data obtained during the deposition process is appended to the historical dataset to perform more accurate predictions for coming layers.

4.4.1 Neural network setup

The thermal, and geometrical data of the previously deposited layer, wire feed speed, and torch travel speed are a set of data composing the input layer of the supervised learning neural network and the output is the deposited layer width and height. The neural network model that maps the input to the output parameters was initially trained with data from 700 layers of bead deposition or a multiple of 14 different 50-layered walls. During acquisition of training dataset, the layers were deposited with random wire feed speed for every layer, ranging from 60 inches per minute (IPM) to 120 IPM with an interval of 10 IPM.

The pretraining of the network was performed using the Sequential model in Keras [99] module, an open-source software library acting as an interface for TensorFlow library [100]. The number of nodes for the input and output layers are 5 and 2, respectively. There are two hidden layers with first hidden layer having 20 nodes, second one with 5 nodes.

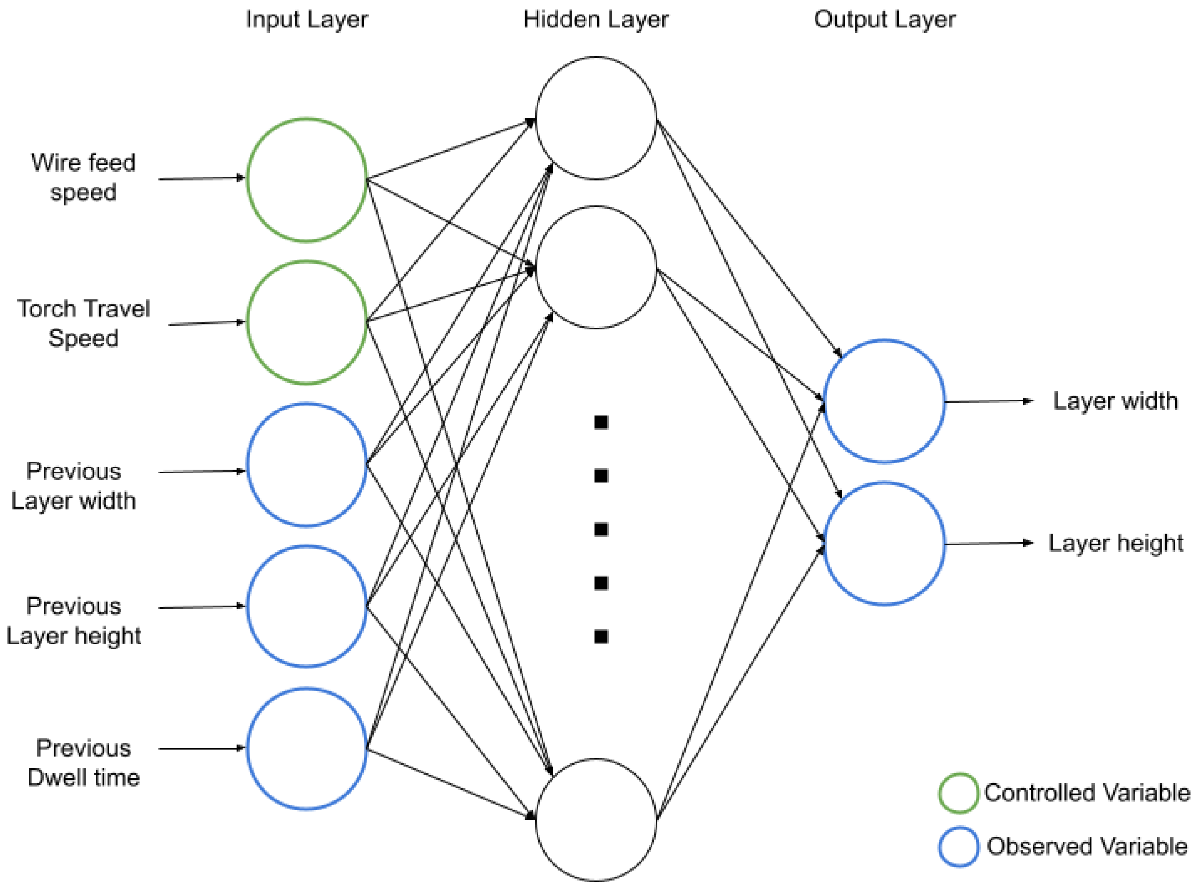

Figure 4.12 Schematic diagram of multilayer neural network

4.4.2 Reinforced inverse supervised learning control algorithm and framework

The control framework utilizes historical deposition rollout data model the input-to-output relation and finally can predict the optimal wire feed speed given desired layer width and height. Also, the framework is capable of enhancing robustness through data reinforcement during the deposition process. Visualization of rollout data collected can be seen in Appendix A. Given the trained neural network that can map the input to the output, it is possible to formulate a framework that can perform control to optimize the bead geometry. The inputs, as can be seen on the input layer of the neural network, are wire feed speed, torch travel speed, previous layer width and height, and the dwell time, or the time taken for the layer to cool to 500 degrees Celsius. The output is the deposited layer's width and height.

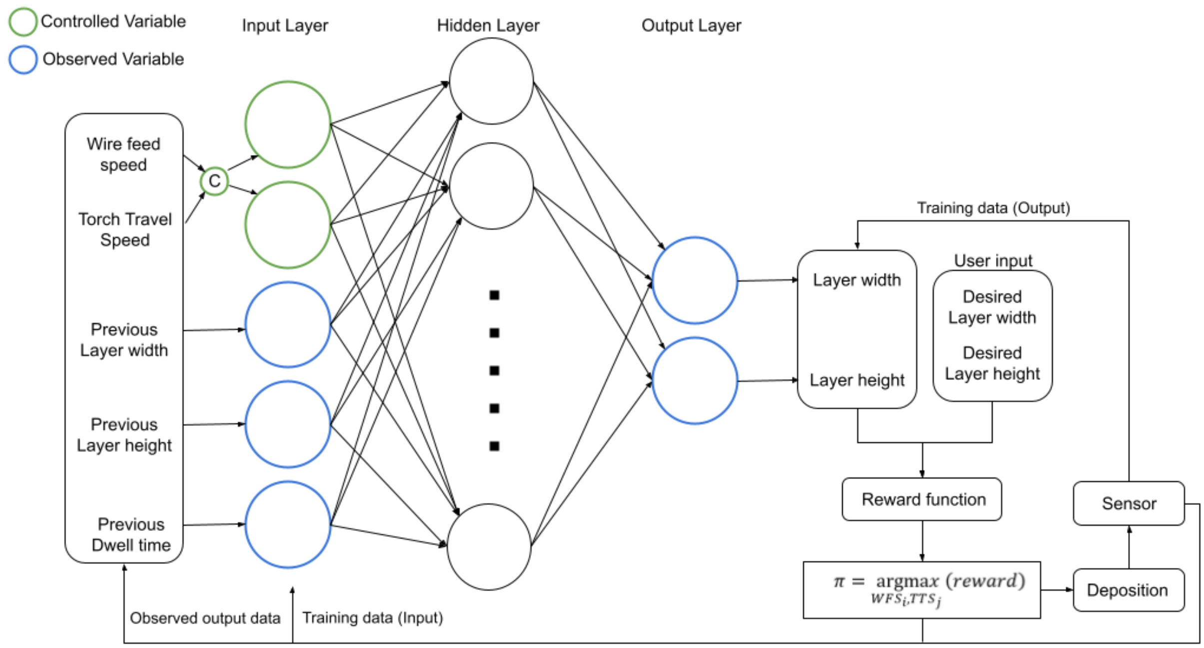

Figure 4.13 Flow diagram of the reinforced inverse supervised learning control framework

Figure 4.13 illustrates the framework of the algorithm expanded from Figure 4.12. First, the user inputs desired layer width and height. Then all combinations of wire feed speed and torch travel speed, indicated by C in the diagram, are simulated with the trained model to output a model predicted geometrical values of width and height. Then, the combination of the wire feed speed and the torch travel speed that resulted in the highest reward value through equation (8) will be selected as the action sets to perform. With more collected rollout data, the weights of the neural network are retrained in-situ with the deposition of every layer to further improve the accuracy of the model.

The control algorithm given layer width, height, and the dwell time of the previous layer can predict the optimal wire feed speed where the optimality criteria are set by a reward function. The policy in choosing the optimal combinations of wire feed speed and torch travel speed is as follows:

$$\pi = \underset{WFS_i, TTS_j}{\operatorname{argmax}} (reward) \tag{8}$$

Here,

$$reward = -|Desired\ width\ - layer\ width| - \frac{|Desired\ height - layer\ height|}{importance\ weight} \tag{9}$$

The various level of the wire speed available is denoted as i. The wire speed level ranges from 60 to 120 IPM, inclusive with interval of 5 IPM. Although the training of the neural network was trained with a broader interval of 10 IPM, the wire feed speed was interpolated to a finer resolution in the WFS to maximize the reward function. The importance weight represents the magnitude at which it diminishes the importance of the height error. An example graph showing how the algorithm decides on the optimal wire feed speed based on the reward calculated with the neural network modeled function is illustrated in Figure 4.14.

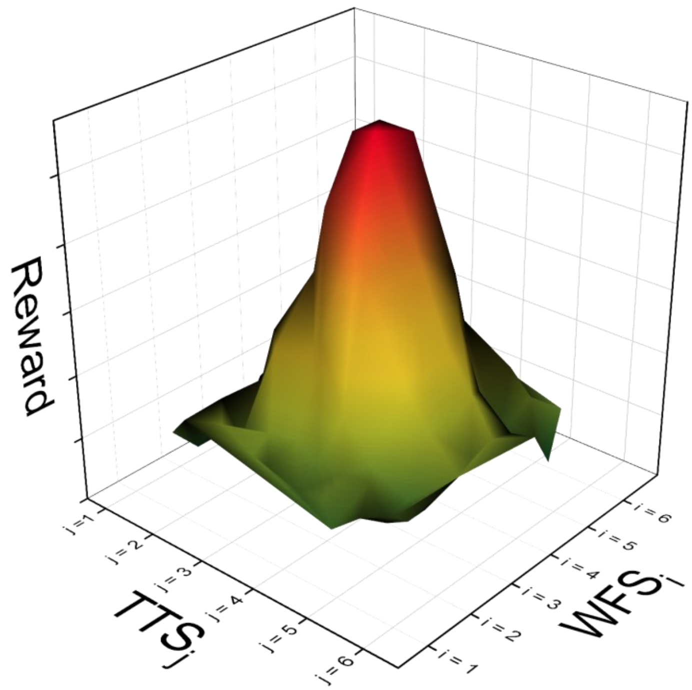

Figure 4.14 Example illustration of perception of algorithm of the action parameters. Combination of actions that results in best reward is chosen

4.4.3 First deposited layers initialization

For both the training and rollout stage of the experiment, the first layer must be initialized. This initialization is required as the deposition of the first layer occurs on the substrate plate with no information of dwell time and the geometrical information on the previously deposited bead. Although the minimum number of layers that must be deposited prior to deploying the control algorithm is one, the initialization is done with the deposition of two layers. This is because the first layer is a special case where the deposition occurs on a cool surface, causing the bead to be very different in size in relation to the following layers. Subsequently, the second layer is also considered a special case as the deposition occurs on top of the first layer. Thus, the first two layers are deposited with a fixed input process parameter. The wire feed speed is set as 90 IPM and 350 cm/min as the torch travel speed for the first two layers initialization. After the initialization layers have been deposited, the dwell time, layer width, and height of the consequent layers are monitored and measured.

5 Results and Discussion

5.1 Control algorithm performance

Using the reinforced inverse supervised learning control algorithm, four walls of 50 layers of deposition were printed, out of which two walls were printed with an input of 5 mm as the target, or the desired width. The other two walls were printed with 5.5 mm as the target width. The importance weight in the reward function is set as 10, to prioritize width optimization. Figure 5.1 shows the tracking performance of the algorithm. All four walls printed showed tracking towards to the desired width. The first layer observed shows undershooting of the width value because the surface where the deposition occurs is at a low temperature and even when it uses the highest possible wire feed rate with low torch travel speed, it cannot achieve tracking as seen in Figure 5.2 and Figure 5.3. The height optimization is found to be unnecessary due to the Fronius welding unit control system micro adjusting synergic line with varying wire stick out length compensating for the deviation in the height during the welding process, giving an overall layer height average of 1.3 mm which matches the desired height.

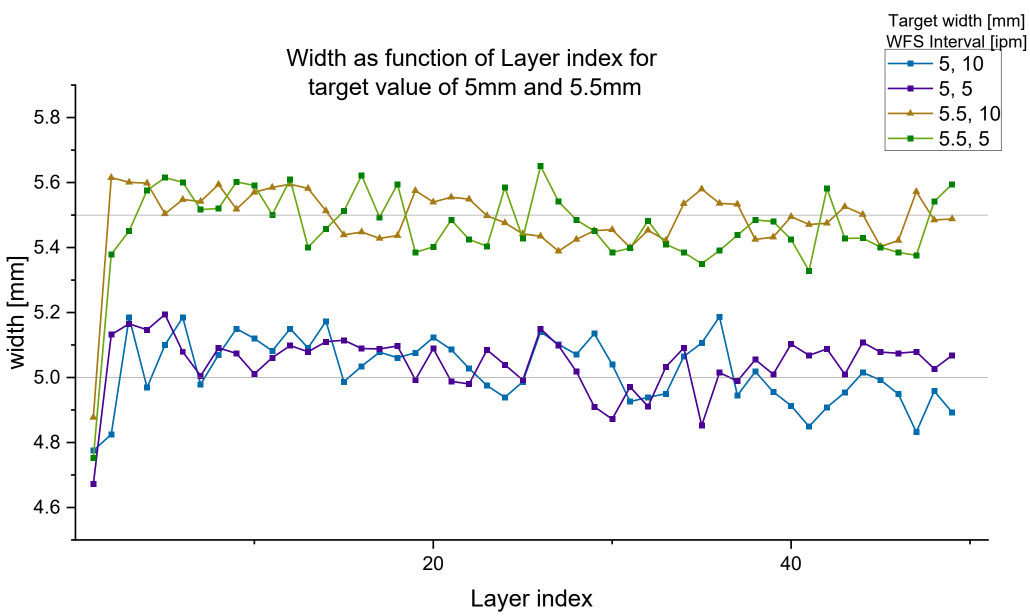

Figure 5.1 Width as function of layer index for target width of 5mm and 5.5mm

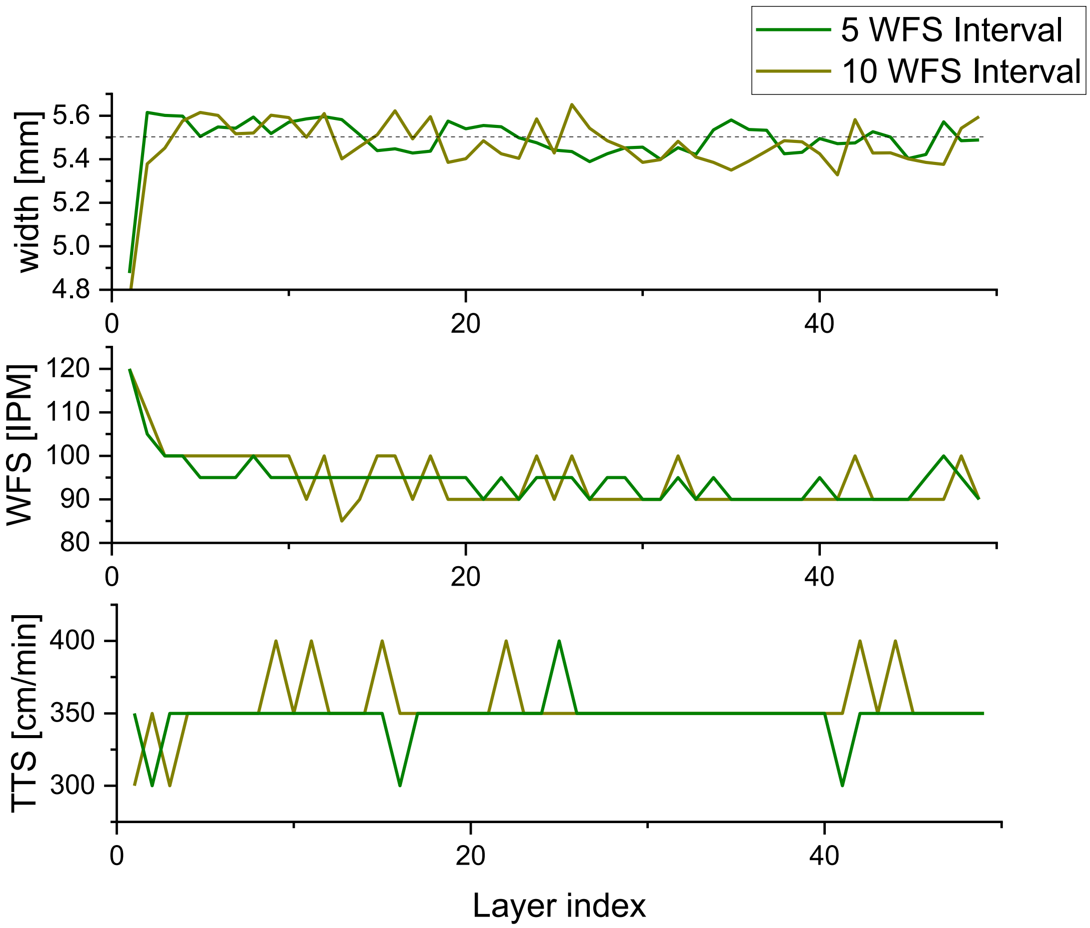

Figure 5.2 Reinforced inverse supervised learning is tracking to the desired layer width of 5.5 mm throughout build of a wall with controlled WFS and TTS. WFS interval of 5 IPM and 10 IPM were used to fabricate the wall

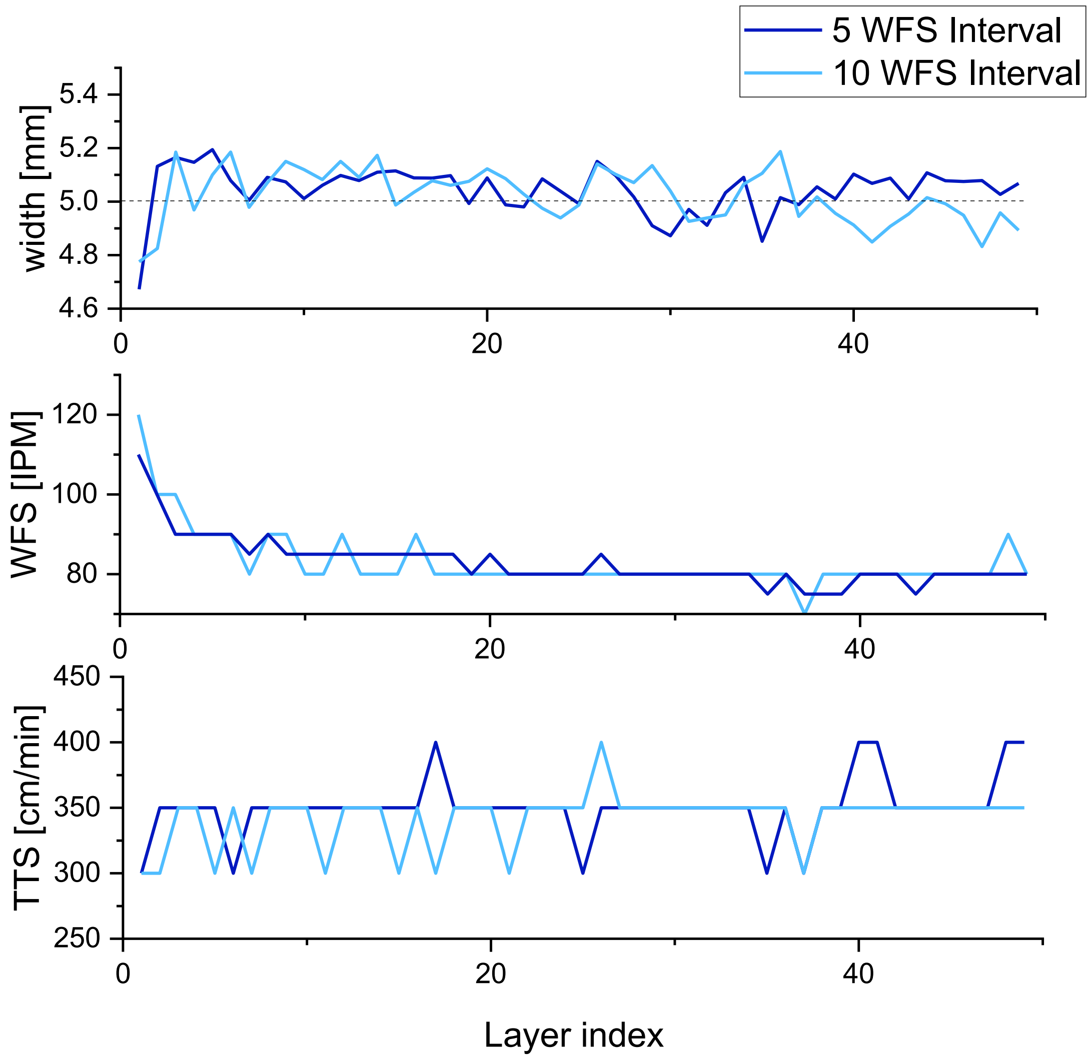

Figure 5.3 Reinforced inverse supervised learning is tracking to the desired layer width of 5 mm throughout build of a wall with controlled WFS and TTS. WFS interval of 5 IPM and 10 IPM were used to fabricate the wall

5.2 Performance Comparison with Open Loop Control Strategy

The performance of the proposed control method is compared to that of the traditional method of printing the bead. Torch travel speed of 350 cm/min, the wire feed speed of 80 and 90 IPM were used for printing bead with target width of 5 mm and 5.5 mm, respectively. The graphs in Figure 5.4 and Figure 5.5 show the comparison of the resulting width for both the proposed control method and traditional methods as a function of deposited layers.

As the traditional method of printing does not take into account of the cool surface during the deposition of the earlier layers, the resulting width is small. This can be seen in Figure 5.7 and Figure 5.8 a) where the width of the earlier layers built using the traditional method is noticeably thinner than the layers built later in the wall. However, it gradually gains sufficient interpass temperature with every iteration of the building to lend correct deposition width. The usage of high wire feed speed by the algorithm at the beginning stage of deposition can be seen in Figure 5.4 and Figure 5.5 for target widths of 5 mm and 5.5 mm, respectively.

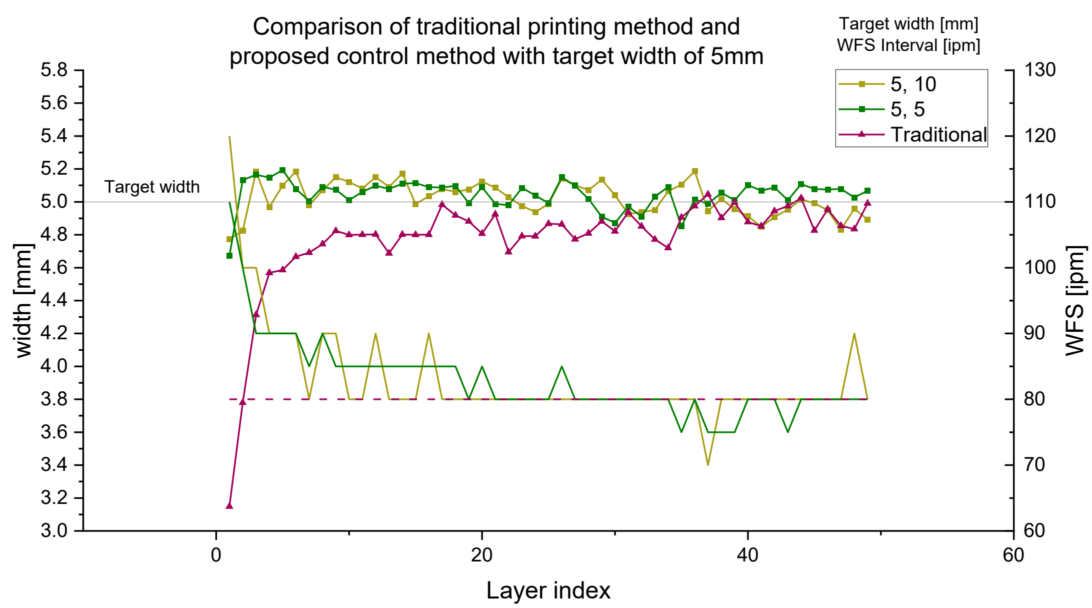

Figure 5.4 Comparison of traditional printing method and proposed control method with target width of 5mm. Varying WFS with increasing number of layer index is shown by the lines without data points and are represented on right y-axis

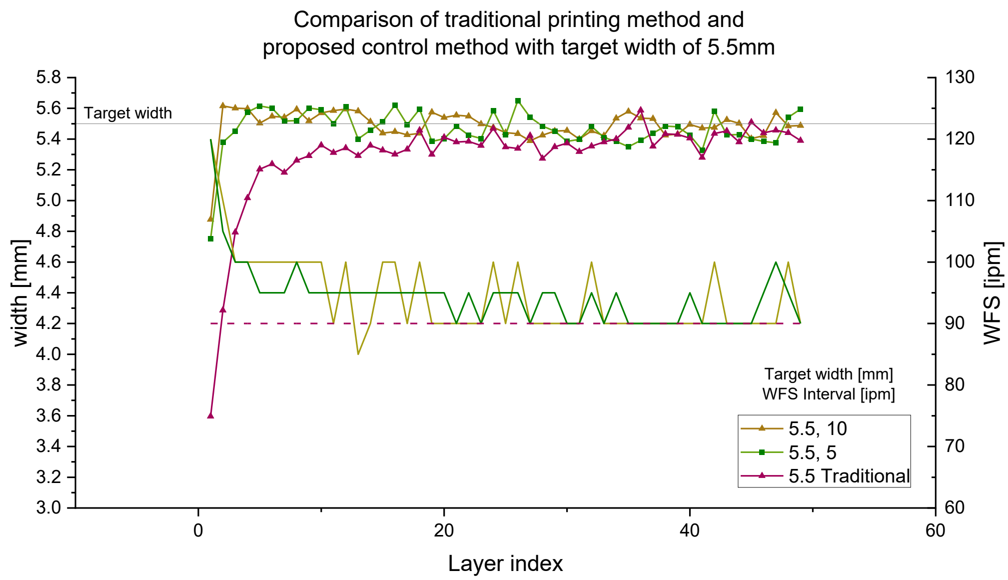

Figure 5.5 Comparison of traditional printing method and proposed control method with target width of 5.5mm. Varying WFS with increasing number of layer index is shown by the lines without data points and are represented on right y-axis

The moving average of the printed walls including walls fabricated using the traditional method are shown in Figure 5.6. The moving average graph smoothed out the trajectory of the width observed, and it is evident that all methods showed sufficient tracking to the target width. Also, there is a slight overshoot in width for all walls printed with the control algorithm, giving about 0.1 mm more thickness than the desired width. Although using the maximum allowed wire feed speed of 120 IPM at the beginning layer is the desired behavior, the width overshot the desired width very slightly by consecutively utilizing a high wire feed speed of 100 for the next few layers. This behavior output by the neural network may have been caused by the lack of data that matches the condition of printing on a surface with a relatively low temperature. To compensate for the undershooting of the width in the beginning layer, the torch travel speed could have been set lower by the algorithm, down to 250 cm/min which is the minimum value it can have in the experimental setting. However, it is a significant improvement over the traditional method of printing the wall where the wire feed speed is held constant. The width of the wall printed with the traditional method does not track the target width fast enough. Additionally, having a 5 WFS control interval had a slight edge over having a 10 WFS control interval in tracking the target width, especially when targeting 5.5 mm. Summary of results for average width and average standard deviation of width are displayed in TABLE x and x, respectively. The tables show decent performance improvement in both tracking performance and standard deviation of width throughout the build with the proposed algorithm. Standard deviation of width decreased by 49% and 39%, average width deviation dropped by 90% and 94.5% when building wall of of 5 mm and 5.5 mm thickness, respectively.

Table 5.1 Average width of printed beads with target width of 5 mm and 5.5 mm for various control methods

Control method \ Target Width	5 mm	5.5 mm
Traditional	4.773	5.292
10 WFS interval	5.022	5.464
5 WFS interval	5.044	5.489

Table 5.2 Average standard deviation of printed beads with target width of 5 mm and 5.5 mm for various control methods

Control method \ Target Width	5 mm	5.5 mm
Traditional	4.773	5.292
10 WFS interval	5.022	5.464
5 WFS interval	5.044	5.489

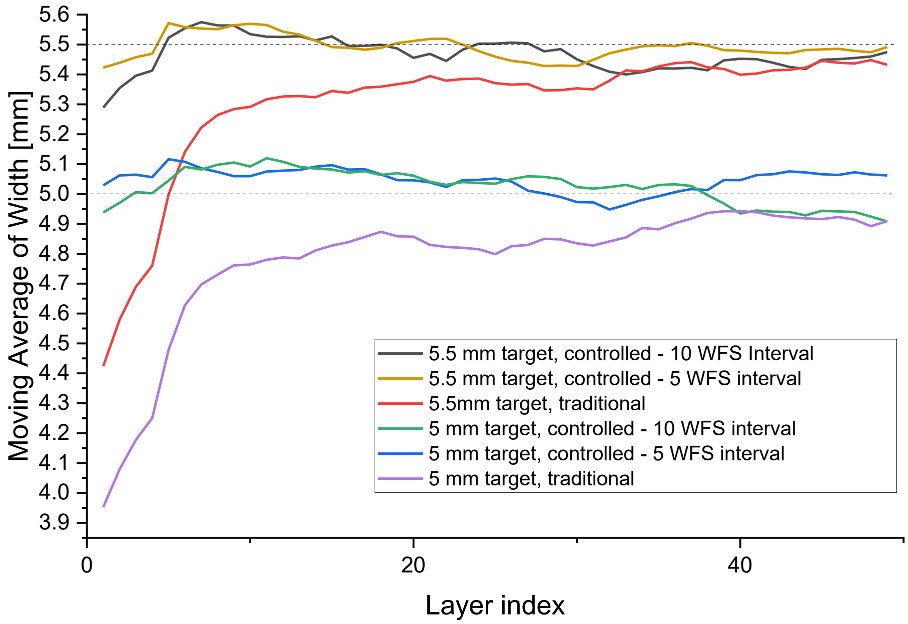

Figure 5.6 Moving average of width for all printed walls as a function of layer index

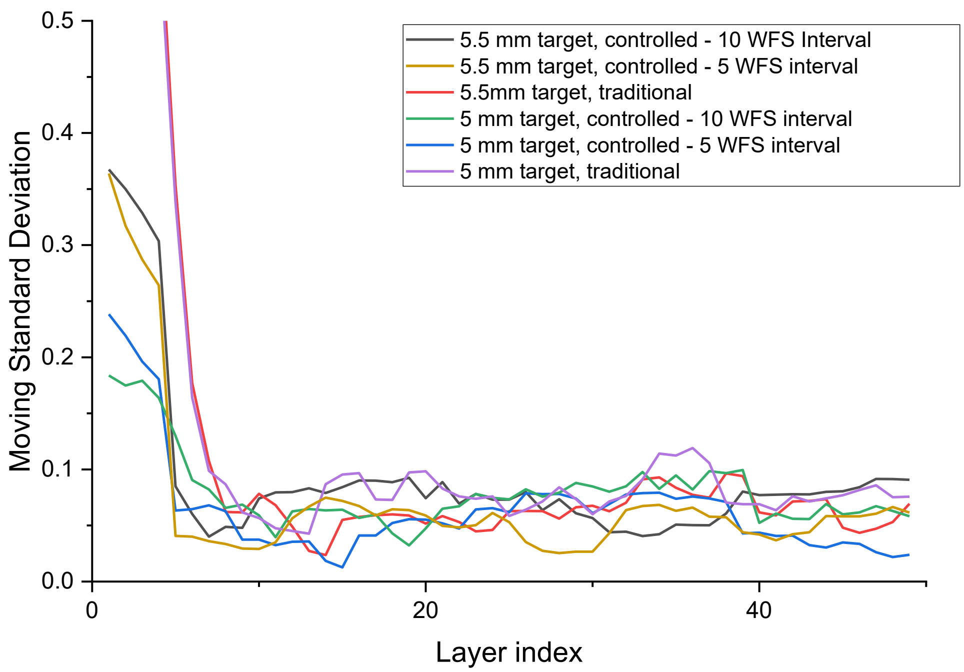

Figure 5.7 Moving standard deviation of width of all printed walls as a function of layer index

The moving standard deviation with 6 data windows is displayed in Figure 5.7. Although the effect of the control algorithm in comparison to the traditional method is not visually distinctive throughout the entire layer, the standard deviation of width for the walls built with the control algorithm with a 5 WFS interval shows a small improvement over that of the traditional method.

Throughout the experiments, measurement errors may have occurred with the profile sensor where the profile reading may be different from the actual value due to the vibration in the gantry system during the measurement and the reflection from the shiny surface of the deposited layer. Also, the time taken to cool down, or the dwell time may have been affected due to the room temperature that varied between 20 to 25 degrees Celsius throughout the training data collection stage as well as the actual algorithm testing stage.

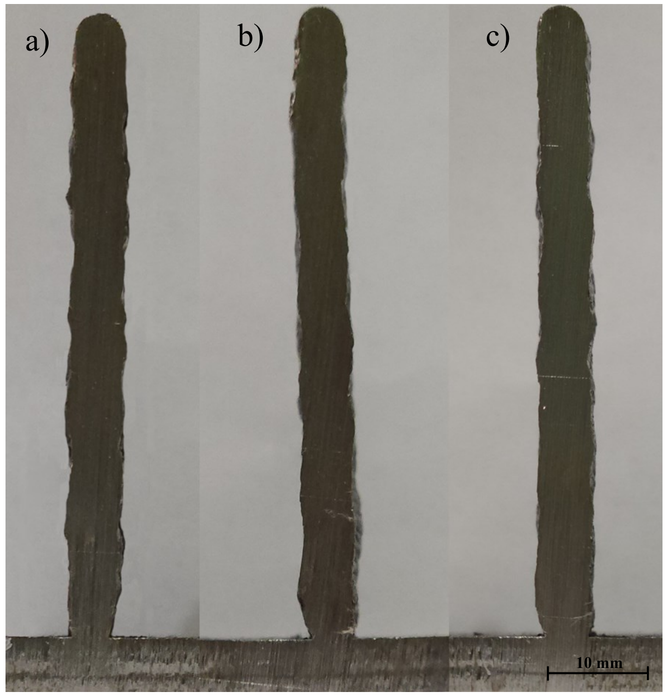

Figure 5.8 Cross-sectional view of a wall targeted to build 5 mm layer width using a) traditional method b) 10 WFS interval c) 5 WFS interval

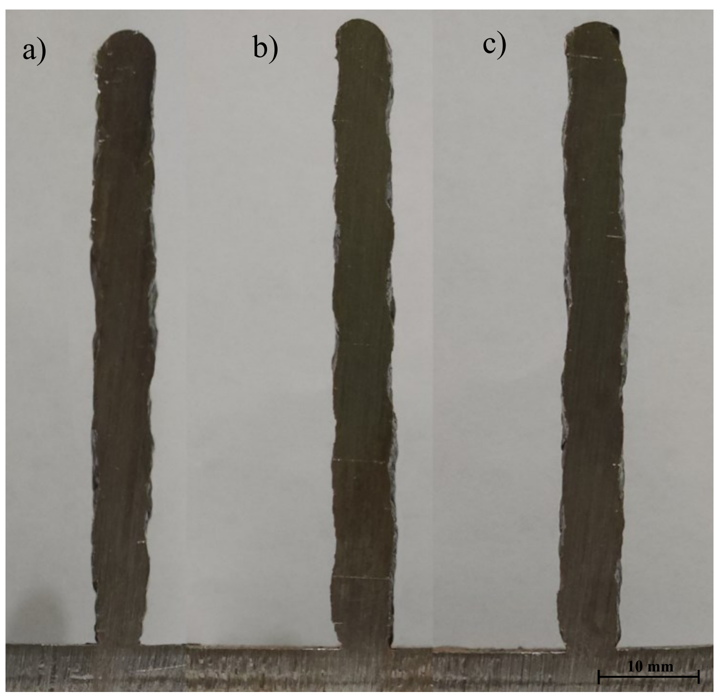

Figure 5.9 Cross-sectional view of a wall targeted to build 5.5 mm layer width using a) traditional method b) 10 WFS interval c) 5 WFS interval

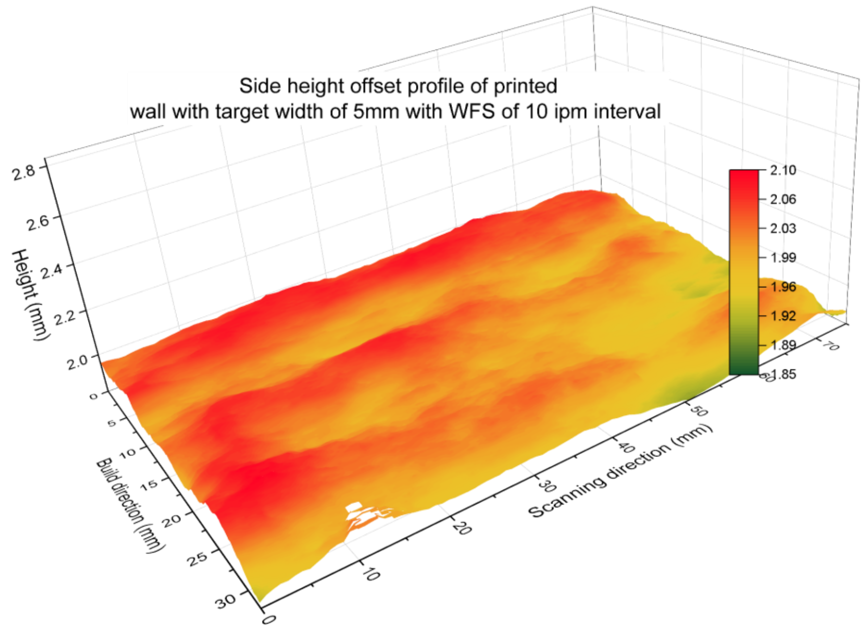

Figure 5.10 Side profile of wall printed with target width of 5mm and 10 IPM of WFS interval

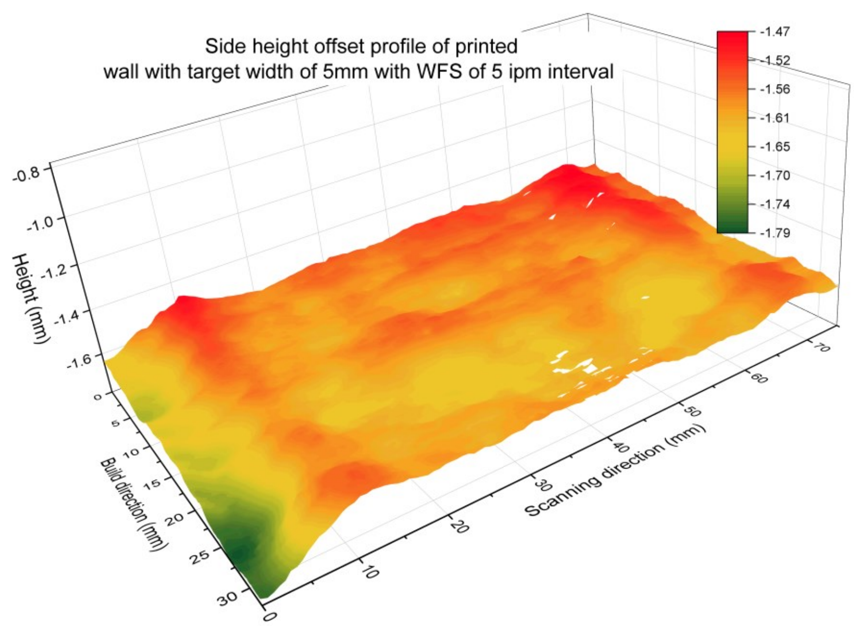

Figure 5.11 Side profile of wall printed with target width of 5mm and 5 IPM of WFS interval

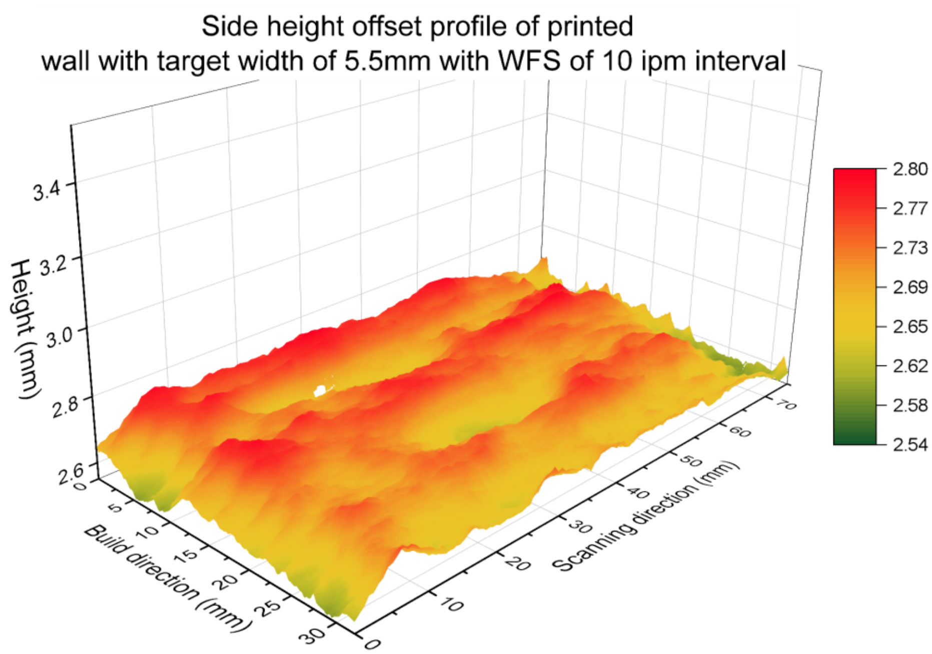

Figure 5.12 Side profile of wall printed with target width of 5.5 mm and 10 IPM of WFS interval

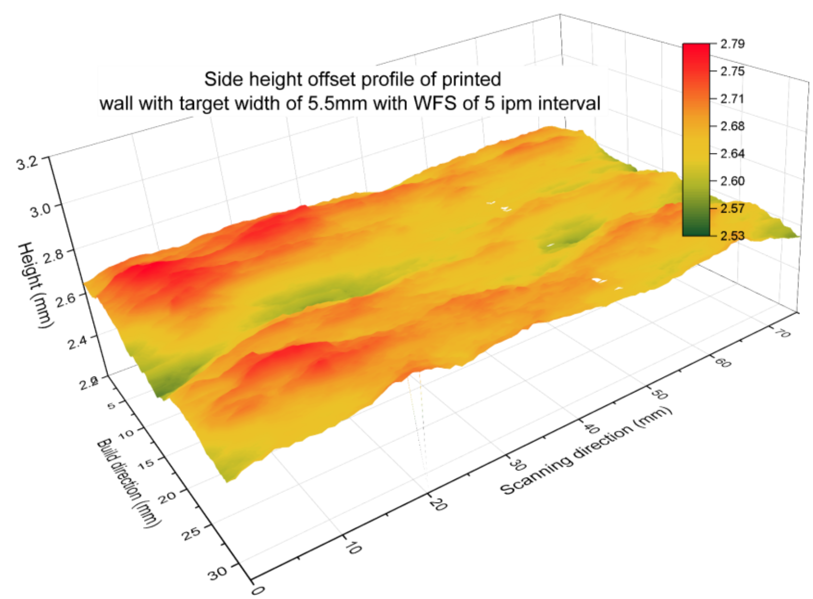

Figure 5.13 Side profile of wall printed with target width of 5.5mm and 5 IPM of WFS interval

Figure 5.10 to Figure 5.13 shows the scanned side profiles of all walls printed with the control algorithm with varying target width and the WFS interval. The deviation of width of the side profile in the measurement window lies between approximately 0.2 mm to 0.3 mm. This deviation measurement may have increased due to slant in the workpiece during the scanning process and the inconsistency in alignment of the layer deposition during the printing process as can be seen by the waviness in the wall as a function of increasing number of layers in Figure 5.9 b).

The major advantage of the WAAM system integrated with a reinforced inverse supervised learning control algorithm is the ability to learn from data to make a model of the dynamic process. This ability, given sufficient data to learn from, allows the operator of the WAAM system to input any reasonable target width, and it will be able to print beads with the desired width regardless of choice of the welding material.

6 Conclusion and Future Work

6.1 Conclusion

Numerous input parameters affecting the geometrical output exist in WAAM, and they are often difficult to control as they are highly non-linear and coupled. To overcome this challenge, an in-situ data-reinforced control framework with machine learning integration or reinforced inverse supervised learning control is developed and implemented on a sensor-integrated custom 3-axis gantry robot with a CMT welding unit to optimize the output bead geometry of building single-track multi-layer wall. Reinforcement learning methods such as Q-learning and policy gradient method showed promising results in simulation, but they did not show convergence in real-world due to lack of data and the limitation of the algorithms. However, the performed experiments provided sufficient training data to initially train the supervised learning neural network model within the proposed reinforced inverse supervised learning method to successfully have the output bead width track the inputted desired width of 5 mm and 5.5mm. In comparison to the traditional method of printing the wall, the tracking performance significantly improved especially during the early stage of layer deposition. The average width deviation dropped by up to 90% and 94.5%, and the standard deviation of the wall width decreased by 49% and 39% with the implementation of the algorithm with the WFS control resolution of 5 WFS for target wall thickness of 5 mm and 5.5 mm, respectively. A major advantage of this control framework is its ability to control the WAAM system to track any given width. since it has learned the input-to-output model through the data-driven machine learning approach.

6.2 Future Work

The future work of the experiment involves incorporating more input and output parameters to build more accurate model, hence further improving the quality of the printed part. Some of the parameters that could be taken into consideration are part cooling rate, material used, gas flow rate, synergic pulse current, voltage, and timing. Additionally, further work will involve optimizing the geometries of parts with more complex features such as overhangs and angles. As the involvement of complex geometries consequently requires more sophisticated sensing technologies, equipment will require modifications and upgrades such as development and integration of a 2-axis baseplate positioner and an instrumentation rig that allows the sensing equipment like profiler to track the deposited bead with varying angles. With the developed in-house ROS integrated control software, future work may involve exploring more state-of-art reinforcement learning algorithms suitable for controlling WAAM processes. For effective use of the control algorithm, an iterative study will be required to determine the optimum hyperparameters such as the number of nodes, layers, required number of training data, etc.

References

[1] O. Yilmaz and A. A. Ugla, "Shaped metal deposition technique in additive manufacturing: A review:," *http://dx.doi.org/10.1177/0954405416640181*, vol. 230, no. 10, pp. 1781–1798, Apr. 2016, doi: 10.1177/0954405416640181.

[2] H. P. Tang, M. Qian, N. Liu, X. Z. Zhang, G. Y. Yang, and J. Wang, "Effect of Powder Reuse Times on Additive Manufacturing of Ti-6Al-4V by Selective Electron Beam Melting," *JOM*, vol. 67, no. 3, 2015, doi: 10.1007/s11837-015-1300-4.

[3] Y. Zhang *et al.*, "Additive Manufacturing of Metallic Materials: A Review," *Journal of Materials Engineering and Performance*, vol. 27, no. 1. 2018. doi: 10.1007/s11665-017-2747-y.

[4] J. Mehnen, J. Ding, H. Lockett, and P. Kazanas, "Global Product Development," *Global Product Development*, no. January, 2011, doi: 10.1007/978-3-642-15973-2.

[5] S. W. Williams *et al.*, "Wire+arc additive manufacturing vs. traditional machining from solid: a cost comparison," *Materials Science and Technology (United Kingdom)*, vol. 32, no. October, 2015.

[6] J. Mehnen, J. Ding, H. Lockett, and P. Kazanas, "Design study for wire and arc additive manufacture," *International Journal of Product Development*, vol. 19, no. 1–3, 2014, doi: 10.1504/IJPD.2014.060028.

[7] O. v. Panchenko, L. A. Zhabrev, D. v. Kurushkin, and A. A. Popovich, "Macrostructure and Mechanical Properties of Al – Si, Al – Mg – Si, and Al – Mg – Mn Aluminum Alloys Produced by Electric Arc Additive Growth," *Metal Science and Heat Treatment*, vol. 60, no. 11–12, 2019, doi: 10.1007/s11041-019-00351-z.

[8] C. Xia *et al.*, "A review on wire arc additive manufacturing: Monitoring, control and a framework of automated system," *J Manuf Syst*, vol. 57, no. July, pp. 31–45, 2020, doi: 10.1016/j.jmsy.2020.08.008.

[9] J. J. Lewandowski and M. Seifi, "Metal Additive Manufacturing: A Review of Mechanical Properties," *Annu Rev Mater Res*, vol. 46, pp. 151–186, 2016, doi: 10.1146/annurev-matsci-070115-032024.

[10] T. Sathish, J. Jayaprakash, P. v. Senthil, and R. Saravanan, "Multi period disassembly-to-order of end of life product based on scheduling to maximize the profit in reverse logistic operation," *FME Transactions*, vol. 45, no. 1, pp. 172–180, 2017, doi: 10.5937/fmet1701172S.

[11] T. Sathish, K. Muthukumar, and B. Palani Kumar, “A study on making of compact manual paper recycling plant for domestic purpose,” *International Journal of Mechanical and Production Engineering Research and Development*, vol. 8, no. Special Issue 7, pp. 1515–1535, 2018.

[12] B. Wu, Z. Pan, S. Li, D. Cuiuri, D. Ding, and H. Li, “The anisotropic corrosion behaviour of wire arc additive manufactured Ti-6Al-4V alloy in 3.5% NaCl solution,” *Corros Sci*, vol. 137, no. March, pp. 176–183, 2018, doi: 10.1016/j.corsci.2018.03.047.

[13] L. E. Murr *et al.*, “Characterization of titanium aluminide alloy components fabricated by additive manufacturing using electron beam melting,” *Acta Mater*, vol. 58, no. 5, pp. 1887–1894, 2010, doi: 10.1016/j.actamat.2009.11.032.

[14] R. Li, J. Xiong, and Y. Lei, “Investigation on thermal stress evolution induced by wire and arc additive manufacturing for circular thin-walled parts,” *J Manuf Process*, vol. 40, no. June 2018, pp. 59–67, 2019, doi: 10.1016/j.jmapro.2019.03.006.

[15] S. W. Williams, F. Martina, A. C. Addison, J. Ding, G. Pardal, and P. Colegrove, “Wire + Arc additive manufacturing,” *Materials Science and Technology (United Kingdom)*, vol. 32, no. 7, pp. 641–647, 2016, doi: 10.1179/1743284715Y.0000000073.

[16] J. Gu *et al.*, “The strengthening effect of inter-layer cold working and post-deposition heat treatment on the additively manufactured Al-6.3Cu alloy,” *Materials Science and Engineering A*, vol. 651, pp. 18–26, Jan. 2016, doi: 10.1016/j.msea.2015.10.101.

[17] V. Dhinakaran, J. Ajith, A. Fathima Yasin Fahmidha, T. Jagadeesha, T. Sathish, and B. Stalin, “Wire Arc Additive Manufacturing (WAAM) process of nickel based superalloys-A review,” *Mater Today Proc*, vol. 21, pp. 920–925, 2020, doi: 10.1016/j.matpr.2019.08.159.

[18] Y. Zhang, Z. Wei, L. Shi, and M. Xi, “Characterization of laser powder deposited Ti-TiC composites and functional gradient materials,” *J Mater Process Technol*, vol. 206, no. 1–3, pp. 438–444, 2008, doi: 10.1016/j.jmatprotec.2007.12.055.

[19] M. Seifi, A. Salem, J. Beuth, O. Harrysson, and J. J. Lewandowski, “Overview of Materials Qualification Needs for Metal Additive Manufacturing,” *Jom*, vol. 68, no. 3, pp. 747–764, 2016, doi: 10.1007/s11837-015-1810-0.

[20] R. Merz, Ramaswami, K. Terk, and M. Weiss, “Shape Deposition Manufacturing,” *The Solid Freeform Fabrication Symposium*, no. 8426325, pp. 1–7, 1994, [Online]. Available: https://repositories.lib.utexas.edu/handle/2152/68579

[21] M. Agarwala, D. Bourell, J. Beaman, H. Marcus, and J. Barlow, “Direct selective laser sintering of metals,” *Rapid Prototyp J*, vol. 1, no. 1, pp. 26–36, 1995, doi: 10.1108/13552549510078113.

[22] K. Taminger and R. Hafley, “Electron beam freeform fabrication: a rapid metal deposition process,” *Proceedings of the 3rd Annual Automotive Composites Conference*, pp. 9–10, 2003, [Online]. Available: http://www.ntrs.nasa.gov/archive/nasa/casi.ntrs.nasa.gov/20040042496_2004036110.pdf

[23] G. K. Lewis and E. Schlienger, “Practical considerations and capabilities for laser assisted direct metal deposition,” *Mater Des*, pp. 417–423, 2000.

[24] F. Wang, S. Williams, and M. Rush, “Morphology investigation on direct current pulsed gas tungsten arc welded additive layer manufactured Ti6Al4V alloy,” *The International Journal of Advanced Manufacturing Technology*, vol. 57, no. 5–8, pp. 597–603, Nov. 2011, doi: 10.1007/s00170-011-3299-1.

[25] P. M. Sequeira Almeida and S. Williams, “Innovative process model of Ti-6Al-4V additive layer manufacturing using cold metal transfer (CMT),” *21st Annual International Solid Freeform Fabrication Symposium - An Additive Manufacturing Conference, SFF 2010*, no. January 2010, pp. 25–36, 2010.

[26] E. Brandl, V. Michailov, B. Viehweger, and C. Leyens, “Deposition of Ti-6Al-4V using laser and wire, part I: Microstructural properties of single beads,” *Surf Coat Technol*, vol. 206, no. 6, pp. 1120–1129, 2011, doi: 10.1016/j.surfcoat.2011.07.095.

[27] S. H. Mok, G. Bi, J. Folkes, and I. Pashby, “Deposition of Ti-6Al-4V using a high power diode laser and wire, Part I: Investigation on the process characteristics,” *Surf Coat Technol*, vol. 202, no. 16, pp. 3933–3939, 2008, doi: 10.1016/j.surfcoat.2008.02.008.

[28] D. Ding, Z. Pan, D. Cuiuri, and H. Li, “Wire-feed additive manufacturing of metal components: technologies, developments and future interests,” *International Journal of Advanced Manufacturing Technology*, vol. 81, no. 1–4. 2015. doi: 10.1007/s00170-015-7077-3.

[29] R. Baker, “Method of making decorative articles,” 1925

[30] Jr. William D. White, “Pressure roller and method of manufacture,” 1962.

[31] K. Kussmaul, F. W. Schoch, and H. Luckow, “High quality large components shape welded by saw process,” 1983.

[32] P. M. Dickens, M. S. Pridham, R. C. Cobb, I. Gibson, and G. Dixon, "Rapid Prototyping Using 3-D Welding," 1992.

[33] RAMLAB, "WAAMpeller." 2017. [Online]. Available: https://www.ramlab.com/wp-content/uploads/2017/12/WAAMpeller.jpg

[34] Z. Pan, D. Ding, B. Wu, and D. Cuiuri, "Arc Welding Processes for Additive Manufacturing: A Review," *Transactions on Intelligent Welding Manufacturing*, no. 2, pp. 3–24, 2019, doi: 10.1007/978-981-10-8740-0.

[35] C. Buchanan and L. Gardner, "Metal 3D printing in construction: A review of methods, research, applications, opportunities and challenges," *Engineering Structures*, vol. 180. 2019. doi: 10.1016/j.engstruct.2018.11.045.

[36] J. D. Spencer, P. M. Dickens, and C. M. Wykes, "Rapid prototyping of metal parts by three-dimensional welding," *Proc Inst Mech Eng B J Eng Manuf*, vol. 212, no. 3, pp. 175–182, 1998, doi: 10.1243/0954405981515590.

[37] C. S. Wu, L. Wang, W. J. Ren, and X. Y. Zhang, "Plasma arc welding: Process, sensing, control and modeling," *J Manuf Process*, vol. 16, no. 1, pp. 74–85, 2014, doi: 10.1016/j.jmapro.2013.06.004.

[38] O. Yilmaz and A. A. Ugla, "Microstructure characterization of SS308LSi components manufactured by GTAW-based additive manufacturing: shaped metal deposition using pulsed current arc," *The International Journal of Advanced Manufacturing Technology*, vol. 89, no. 1–4, pp. 13–25, Mar. 2017, doi: 10.1007/s00170-016-9053-y.

[39] J. Ding *et al.*, "Thermo-mechanical analysis of Wire and Arc Additive Layer Manufacturing process on large multi-layer parts," *Comput Mater Sci*, vol. 50, no. 12, pp. 3315–3322, 2011, doi: 10.1016/j.commatsci.2011.06.023.

[40] J. Xiong, Y. Lei, H. Chen, and G. Zhang, "Fabrication of inclined thin-walled parts in multi-layer single-pass GMAW-based additive manufacturing with flat position deposition," *J Mater Process Technol*, vol. 240, pp. 397–403, 2017, doi: 10.1016/j.jmatprotec.2016.10.019.

[41] B. Wu *et al.*, "A review of the wire arc additive manufacturing of metals: properties, defects and quality improvement," *J Manuf Process*, vol. 35, no. February, pp. 127–139, 2018, doi: 10.1016/j.jmapro.2018.08.001.

[42] T. Lehmann *et al.*, "Large-scale metal additive manufacturing: a holistic review of the state of the art and challenges," *International Materials Reviews*, 2021, doi: 10.1080/09506608.2021.1971427.

[43] R. Fokens, “Cold Metal Transfer - CMT - A Revolution in Mechanized Root Pass Pipeline Welding,” *4th Pipeline Technology Conference*, 2009.

[44] C. G. Pickin and K. Young, “Evaluation of cold metal transfer (CMT) process for welding aluminium alloy,” *Science and Technology of Welding and Joining*, vol. 11, no. 5, 2006, doi: 10.1179/174329306X120886.

[45] Fronius, “CMT: Cold Metal Transfer-MIG/MAG dip transfer arc process.” 2021.

[46] F. Veiga, A. Suárez, E. Aldalur, and T. Bhujangrao, “Effect of the metal transfer mode on the symmetry of bead geometry in waam aluminum,” *Symmetry*, vol. 13, no. 7. 2021. doi: 10.3390/sym13071245.

[47] I. H. Sarker, “Machine Learning: Algorithms, Real-World Applications and Research Directions,” *SN Comput Sci*, vol. 2, no. 3, pp. 1–21, 2021, doi: 10.1007/s42979-021-00592-x.

[48] M. Yin, J. W. Vaughan, and H. Wallach, “Understanding the effect of accuracy on trust in machine learning models,” *Conference on Human Factors in Computing Systems - Proceedings*, pp. 1–12, 2019, doi: 10.1145/3290605.3300509.

[49] L. Bote-Curiel, S. Muñoz-Romero, A. Gerrero-Curieses, and J. L. Rojo-álvarez, “Deep learning and big data in healthcare: A double review for critical beginners,” *Applied Sciences (Switzerland)*, vol. 9, no. 11, 2019, doi: 10.3390/app9112331.

[50] S. S. Mousavi, M. Schukat, and E. Howley, “Deep Reinforcement Learning: An Overview,” *Lecture Notes in Networks and Systems*, vol. 16, pp. 426–440, 2018, doi: 10.1007/978-3-319-56991-8_32.

[51] R. S. Sutton and A. G. Barto, “Reinforcement Learning: An Introduction,” *IEEE Trans Neural Netw*, vol. 9, no. 5, 1998, doi: 10.1109/tnn.1998.712192.

[52] R. Bellman, “A Markovian Decision,” *Journal of Mathematics and Mechanics*, pp. 679–684, 1957.

[53] L. Buşoniu and R. Munos, “Optimistic planning for Markov decision processes,” *Journal of Machine Learning Research*, vol. 22, pp. 182–189, 2012.

[54] J. Han, M. Kamber, and J. Pei, *Data Mining: Concepts and Techniques*. 2012. doi: 10.1016/C2009-0-61819-5.

[55] I. H. Sarker, A. S. M. Kayes, S. Badsha, H. Alqahtani, P. Watters, and A. Ng, “Cybersecurity data science: an overview from machine learning perspective,” *J Big Data*, vol. 7, no. 1, 2020, doi: 10.1186/s40537-020-00318-5.

[56] N. Kumar *et al.*, “Wire Arc Additive Manufacturing – A revolutionary method in additive manufacturing,” *Mater Chem Phys*, vol. 285, no. October 2021, p. 126144, 2022, doi: 10.1016/j.matchemphys.2022.126144.

[57] K. Pal, S. Bhattacharya, and S. K. Pal, “Prediction of metal deposition from arc sound and weld temperature signatures in pulsed MIG welding,” *International Journal of Advanced Manufacturing Technology*, vol. 45, no. 11–12, pp. 1113–1130, 2009, doi: 10.1007/s00170-009-2052-5.

[58] W. Ya, A. R. Konuk, R. Aarts, B. Pathiraj, and B. Huis In ’T Veld, “Spectroscopic monitoring of metallic bonding in laser metal deposition,” *J Mater Process Technol*, vol. 220, pp. 276–284, 2015, doi: 10.1016/j.jmatprotec.2015.01.026.

[59] S. UNNIKRISHNAKURUP, “Monitoring TIG welding using infrared thermography - simulations and experiments,” *Przegląd Elektrotechniczny*, vol. 1, no. 4, pp. 8–11, 2016, doi: 10.15199/48.2016.04.02.

[60] A. M. Pringle, S. Oberloier, A. L. Petsiuk, P. G. Sanders, and J. M. Pearce, “Open source arc analyzer: Multi-sensor monitoring of wire arc additive manufacturing,” *HardwareX*, vol. 8, p. e00137, 2020, doi: 10.1016/j.ohx.2020.e00137.

[61] F. Xu *et al.*, “Multi-Sensor System for Wire-Fed Additive Manufacture of Titanium Alloys,” *26th International Conference on Flexible Automation and Intelligent Manufacturing (FAIM 2016)*, vol. 44, no. June, p. Article in Press, 2016.

[62] T. A. Davis and Y. C. Shin, “Vision-based clad height measurement,” *Mach Vis Appl*, vol. 22, no. 1, pp. 129–136, 2011, doi: 10.1007/s00138-009-0240-9.

[63] S. Clijsters, T. Craeghs, S. Buls, K. Kempen, and J. P. Kruth, “In situ quality control of the selective laser melting process using a high-speed, real-time melt pool monitoring system,” *International Journal of Advanced Manufacturing Technology*, vol. 75, no. 5–8, pp. 1089–1101, Nov. 2014, doi: 10.1007/s00170-014-6214-8.

[64] M. Grasso, A. G. Demir, B. Previtali, and B. M. Colosimo, “In situ monitoring of selective laser melting of zinc powder via infrared imaging of the process plume,” *Robot Comput Integr Manuf*, vol. 49, pp. 229–239, 2018, doi: 10.1016/j.rcim.2017.07.001.

[65] Y. Zhang, G. S. Hong, D. Ye, K. Zhu, and J. Y. H. Fuh, “Extraction and evaluation of melt pool, plume and spatter information for powder-bed fusion AM process monitoring,” *Mater Des*, vol. 156, pp. 458–469, 2018, doi: 10.1016/j.matdes.2018.07.002.

[66] G. Repossini, V. Laguzza, M. Grasso, and B. M. Colosimo, "On the use of spatter signature for in-situ monitoring of Laser Powder Bed Fusion," *Addit Manuf*, vol. 16, pp. 35–48, 2017, doi: 10.1016/j.addma.2017.05.004.

[67] S. Tang, G. Wang, H. Zhang, and R. Wang, "An online surface defects detection system for AWAM based on deep learning," *Solid Freeform Fabrication 2017: Proceedings of the 28th Annual International Solid Freeform Fabrication Symposium - An Additive Manufacturing Conference, SFF 2017*, pp. 1965–1981, 2020.

[68] F. Bonaccorso, L. Cantelli, and G. Muscato, "An arc welding robot control for a shaped metal deposition plant: Modular software interface and sensors," *IEEE Transactions on Industrial Electronics*, vol. 58, no. 8, pp. 3126–3132, 2011, doi: 10.1109/TIE.2011.2114311.

[69] Q. Zhan, Y. Liang, J. Ding, and S. Williams, "A wire deflection detection method based on image processing in wire + arc additive manufacturing," *The International Journal of Advanced Manufacturing Technology*, vol. 89, no. 1–4, pp. 755–763, Mar. 2017, doi: 10.1007/s00170-016-9106-2.

[70] Y. Huang, D. Wu, Z. Zhang, H. Chen, and S. Chen, "EMD-based pulsed TIG welding process porosity defect detection and defect diagnosis using GA-SVM," *J Mater Process Technol*, vol. 239, pp. 92–102, 2017, doi: 10.1016/j.jmatprotec.2016.07.015.

[71] K. Pal, S. Bhattacharya, and S. K. Pal, "Investigation on arc sound and metal transfer modes for on-line monitoring in pulsed gas metal arc welding," *J Mater Process Technol*, vol. 210, no. 10, pp. 1397–1410, 2010, doi: 10.1016/j.jmatprotec.2010.03.029.

[72] S. Bhattacharya, K. Pal, and S. K. Pal, "Multi-sensor based prediction of metal deposition in pulsed gas metal arc welding using various soft computing models," *Applied Soft Computing Journal*, vol. 12, no. 1, pp. 498–505, 2012, doi: 10.1016/j.asoc.2011.08.016.

[73] S. M. C. van Bohemen, M. J. M. Hermans, and G. den Ouden, "Monitoring of martensite formation during welding by means of acoustic emission," *J Phys D Appl Phys*, vol. 34, no. 22, pp. 3312–3317, 2001, doi: 10.1088/0022-3727/34/22/316.

[74] W. Carter, C. Masuo, A. Nycz, M. Noakes, and D. Vaughan, "Thermal process monitoring for wire-arc additive manufacturing using IR cameras," *Solid Freeform Fabrication 2019: Proceedings of the 30th Annual International Solid Freeform Fabrication Symposium - An Additive Manufacturing Conference, SFF 2019*, no. Figure 1, pp. 1812–1817, 2019.

[75] J. Mireles, S. Ridwan, P. A. Morton, A. Hinojos, and R. B. Wicker, "Analysis and correction of defects within parts fabricated using powder bed fusion technology," *Surf Topogr*, vol. 3, no. 3, 2015, doi: 10.1088/2051-672X/3/3/034002.

[76] A. Fathi, A. Khajepour, E. Toyserkani, and M. Durali, "Clad height control in laser solid freeform fabrication using a feedforward PID controller," *International Journal of Advanced Manufacturing Technology*, vol. 35, no. 3–4, pp. 280–292, Dec. 2007, doi: 10.1007/s00170-006-0721-1.

[77] A. Heralić, A. K. Christiansson, and B. Lennartson, "Height control of laser metal-wire deposition based on iterative learning control and 3D scanning," *Opt Lasers Eng*, vol. 50, no. 9, 2012, doi: 10.1016/j.optlaseng.2012.03.016.

[78] P. Hagqvist, A. Heralić, A. K. Christiansson, and B. Lennartson, "Resistance based iterative learning control of additive manufacturing with wire," *Mechatronics*, vol. 31, pp. 116–123, 2015, doi: 10.1016/j.mechatronics.2015.03.008.

[79] J. Xiong and G. Zhang, "Online measurement of bead geometry in GMAW-based additive manufacturing using passive vision," *Meas Sci Technol*, vol. 24, no. 11, p. 115103, Nov. 2013, doi: 10.1088/0957-0233/24/11/115103.

[80] F. Li, S. Chen, Z. Wu, and Z. Yan, "Adaptive process control of wire and arc additive manufacturing for fabricating complex-shaped components," *International Journal of Advanced Manufacturing Technology*, vol. 96, no. 1–4, pp. 871–879, Apr. 2018, doi: 10.1007/s00170-018-1590-0.

[81] J. Xiong, G. Zhang, Z. Qiu, and Y. Li, "Vision-sensing and bead width control of a single-bead multi-layer part: material and energy savings in GMAW-based rapid manufacturing," *J Clean Prod*, vol. 41, pp. 82–88, Feb. 2013, doi: 10.1016/J.JCLEPRO.2012.10.009.

[82] C. Doumanidis and Y. M. Kwak, "Multivariable adaptive control of the bead profile geometry in gas metal arc welding with thermal scanning," *International Journal of Pressure Vessels and Piping*, vol. 79, no. 4, 2002, doi: 10.1016/S0308-0161(02)00024-8.

[83] C. Doumanidis and Y. M. Kwak, "Geometry modeling and control by infrared and laser sensing in thermal manufacturing with material deposition," *Journal of Manufacturing Science and Engineering, Transactions of the ASME*, vol. 123, no. 1, 2001, doi: 10.1115/1.1344898.

[84] J. S. Smith and C. Balfour, "Real-time top-face vision based control of weld pool size," *Industrial Robot*, vol. 32, no. 4, 2005, doi: 10.1108/01439910510600209.

[85] H. Fan, N. K. Ravala, H. C. Wikle, and B. A. Chin, “Low-cost infrared sensing system for monitoring the welding process in the presence of plate inclination angle,” in *Journal of Materials Processing Technology*, 2003, vol. 140, no. 1-3 SPEC. doi: 10.1016/S0924-0136(03)00836-7.

[86] Y. K. Liu and Y. M. Zhang, “Model-Based predictive control of weld penetration in gas tungsten arc welding,” *IEEE Transactions on Control Systems Technology*, vol. 22, no. 3, 2014, doi: 10.1109/TCST.2013.2266662.

[87] Y. K. Liu and Y. M. Zhang, “Control of 3D weld pool surface,” *Control Eng Pract*, vol. 21, no. 11, 2013, doi: 10.1016/j.conengprac.2013.06.019.

[88] A. Ščetinec, D. Klobčar, and D. Bračun, “In-process path replanning and online layer height control through deposition arc current for gas metal arc based additive manufacturing,” *J Manuf Process*, vol. 64, 2021, doi: 10.1016/j.jmapro.2021.02.038.

[89] A. G. Dharmawan, Y. Xiong, S. Foong, and G. Song Soh, “A Model-Based Reinforcement Learning and Correction Framework for Process Control of Robotic Wire Arc Additive Manufacturing,” *Proc IEEE Int Conf Robot Autom*, pp. 4030–4036, May 2020, doi: 10.1109/ICRA40945.2020.9197222.

[90] C. Xia *et al.*, “Model predictive control of layer width in wire arc additive manufacturing,” *J Manuf Process*, vol. 58, 2020, doi: 10.1016/j.jmapro.2020.07.060.

[91] H. Mu, J. Polden, Y. Li, F. He, C. Xia, and Z. Pan, “Layer-by-layer model-based adaptive control for wire arc additive manufacturing of thin-wall structures,” *J Intell Manuf*, vol. 33, no. 4, pp. 1165–1180, 2022, doi: 10.1007/s10845-022-01920-5.

[92] Q. Yang *et al.*, “Microstructure and Mechanical Properties of TiB2/AlSi7Mg0.6 Composites Fabricated by Wire and Arc Additive Manufacturing Based on Cold Metal Transfer (WAAM-CMT),” *Materials*, vol. 15, no. 7, 2022, doi: 10.3390/ma15072440.

[93] SICK Ltd., “SICK Profiler 2 Short range distance sensor operating instructions.” 2021.

[94] Optris, “IR camera Optris PI 1M.” 2021. [Online]. Available: https://www.optris.global/thermal-imager-optris-pi-1m

[95] C. J. C. H. Watkins and P. Dayan, “Q-learning,” *Mach Learn*, vol. 8, no. 3–4, 1992, doi: 10.1007/bf00992698.

[96] J. Xiong, G. Zhang, J. Hu, and L. Wu, “Bead geometry prediction for robotic GMAW-based rapid manufacturing through a neural network and a second-order regression analysis,” *J Intell Manuf*, vol. 25, no. 1, 2014, doi: 10.1007/s10845-012-0682-1.

[97] M. Saggar, T. D'Silva, N. Kohl, and P. Stone, "Autonomous learning of stable quadruped locomotion," *Lecture Notes in Computer Science (including subseries Lecture Notes in Artificial Intelligence and Lecture Notes in Bioinformatics)*, vol. 4434 LNAI, pp. 98–109, 2007, doi: 10.1007/978-3-540-74024-7_9.

[98] N. Kohl and P. Stone, "Policy gradient reinforcement learning for fast quadrupedal locomotion," *Proc IEEE Int Conf Robot Autom*, vol. 2004, no. 3, pp. 2619–2624, 2004, doi: 10.1109/robot.2004.1307456.

[99] C. Francois, "keras." Github, 2015. [Online]. Available: https://github.com/fchollet/keras

[100] E. B. Martín Abadi, Ashish Agarwal, Paul Barham *et al.*, "TensorFlow: Large-scale machine learning on heterogeneous systems." 2015. [Online]. Available: https://www.tensorflow.org/

Appendix A. Training Data Analysis

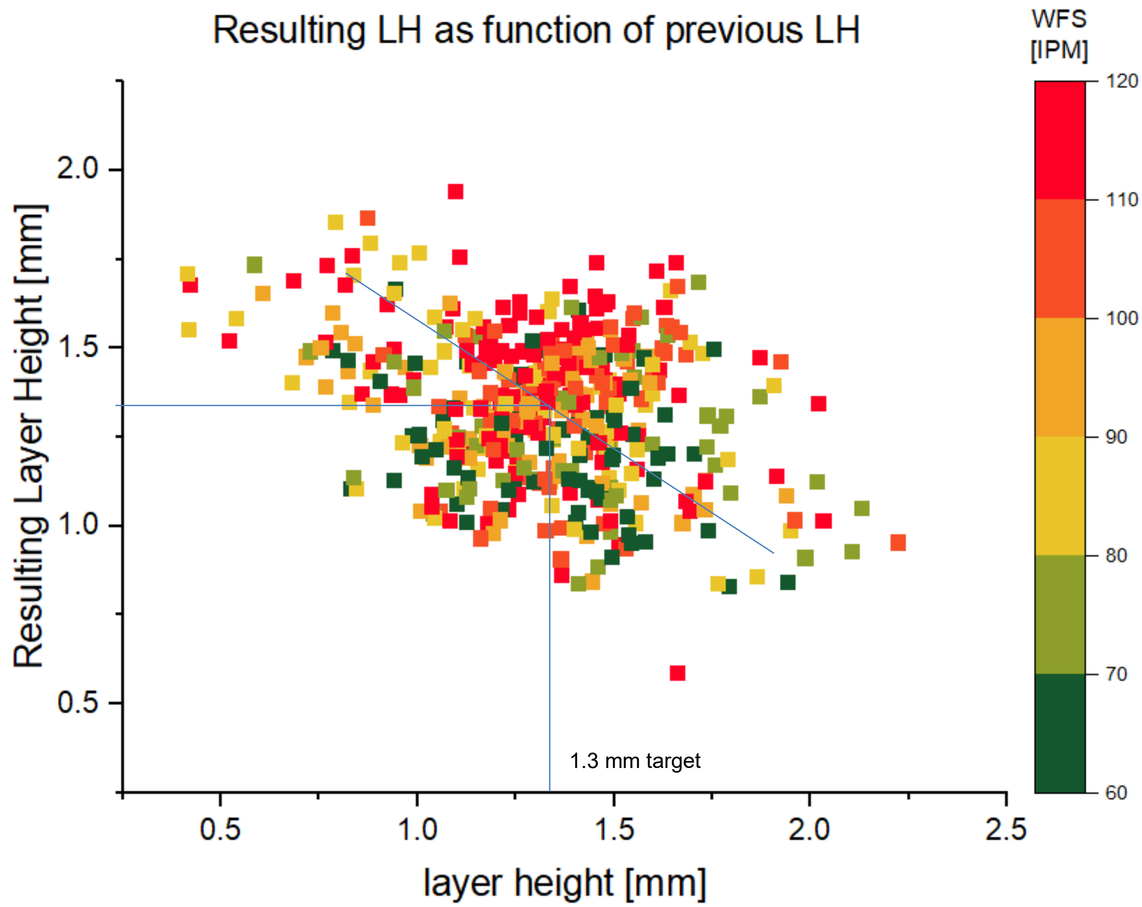

Figure A.1 Resulting layer height (LH) as a function of previous layer height color mapped graph shows that the layer height averages to the target value of 1.3 mm due to the interference of the Fronius welder's control unit

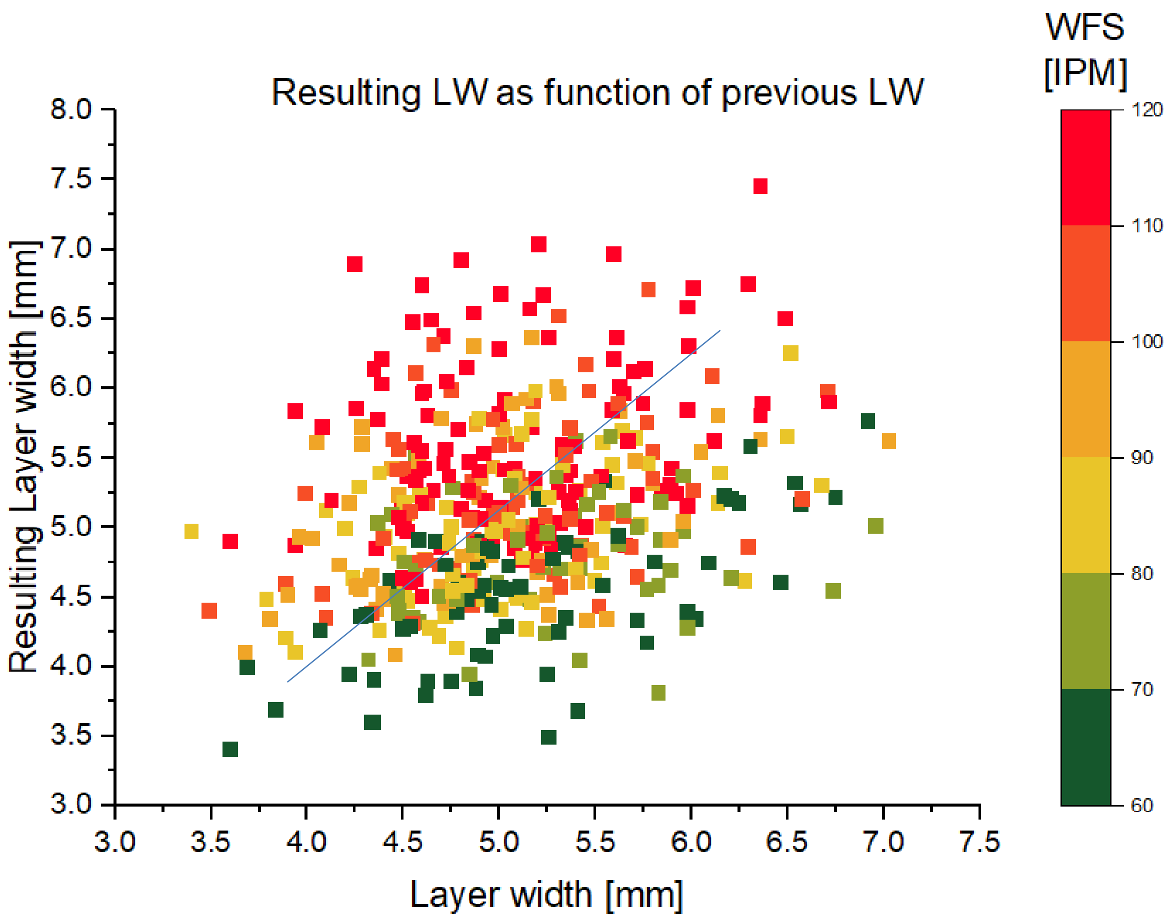

Figure A.2 Resulting layer width (LW) as a function of previous layer width color mapped graph shows that the Previous layer's width impacts the width of the following layer's width

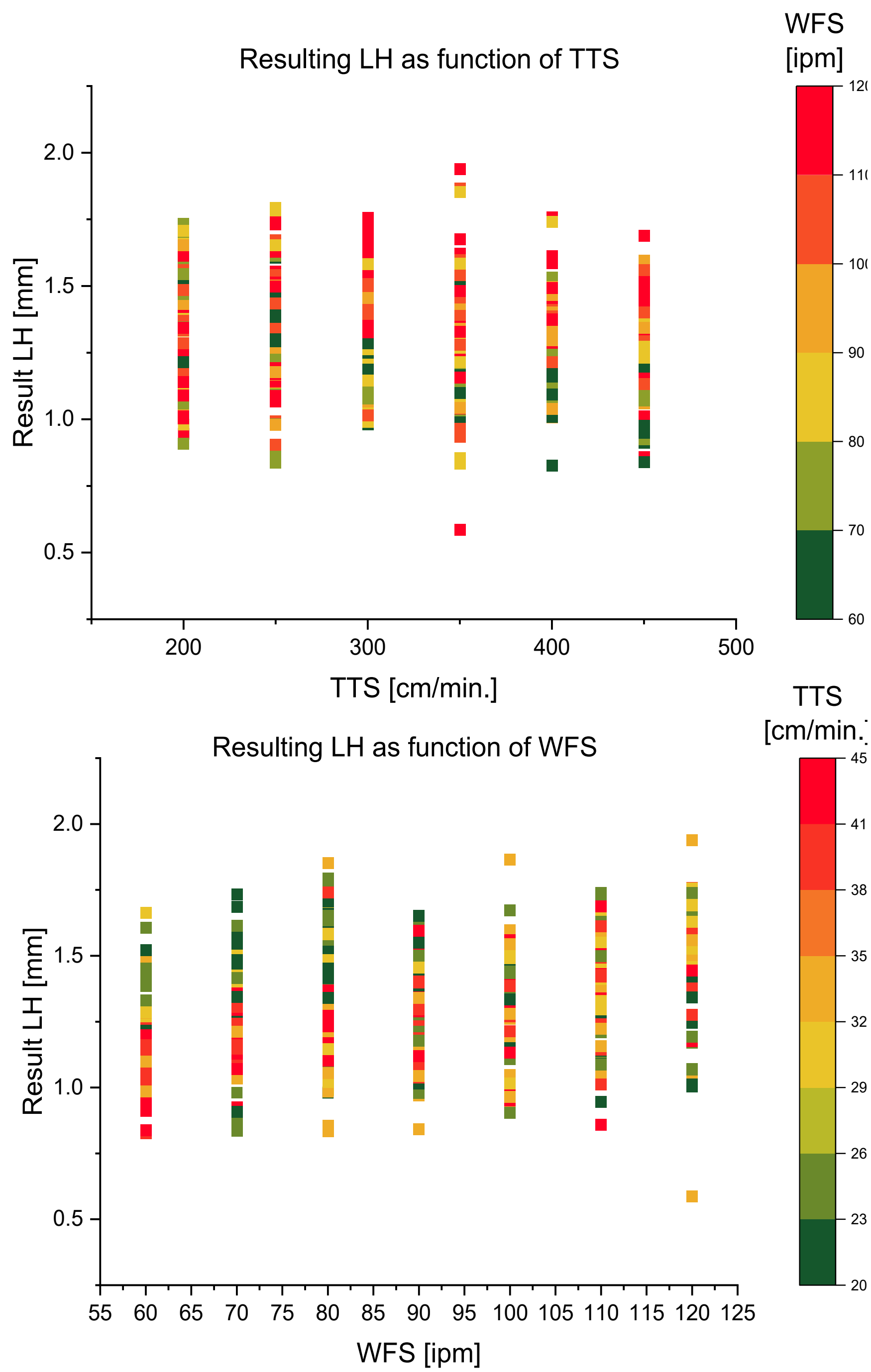

Figure A.3 Resulting layer height as a function of TTS and WFS color mapped. Layer height does not have evident trend with varying WFS and TTS

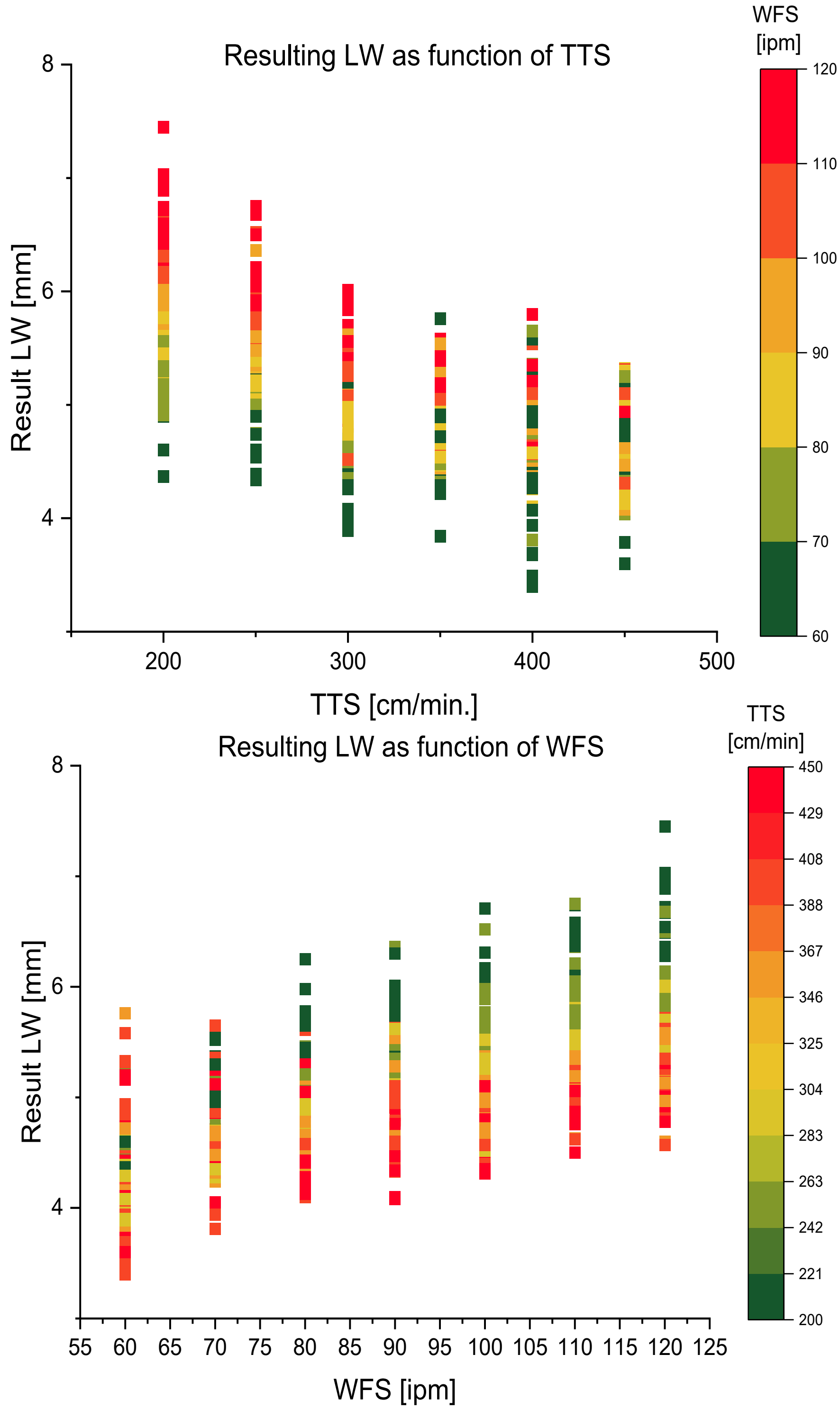

Figure A.4 Resulting layer width as a function of TTS and WFS color mapped. Layer width shows evident trend with varying WFS and TTS

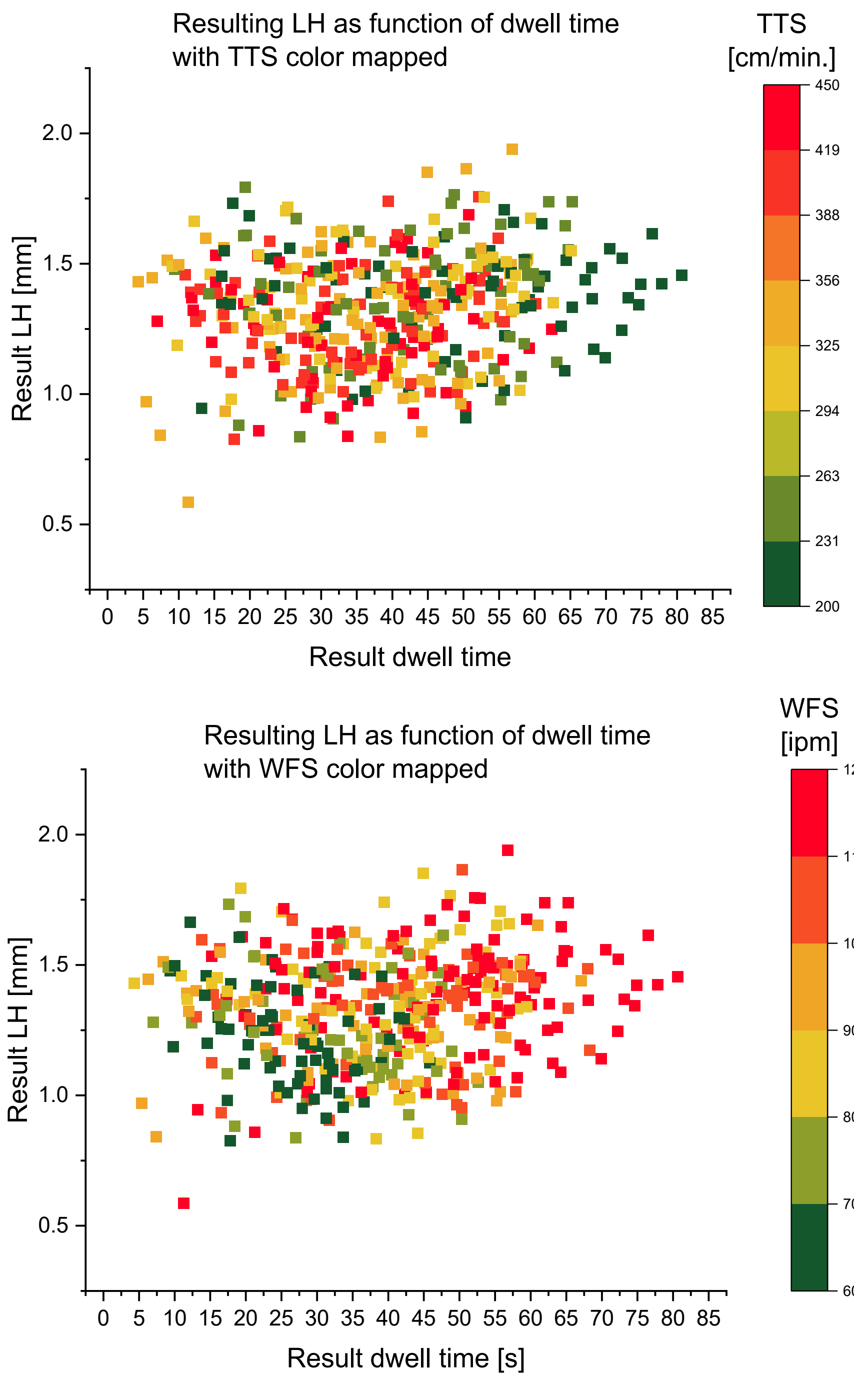

Figure A.5 Resulting layer height as a function of dwell time color mapped. No evident correlation is shown between the layer height and TTS

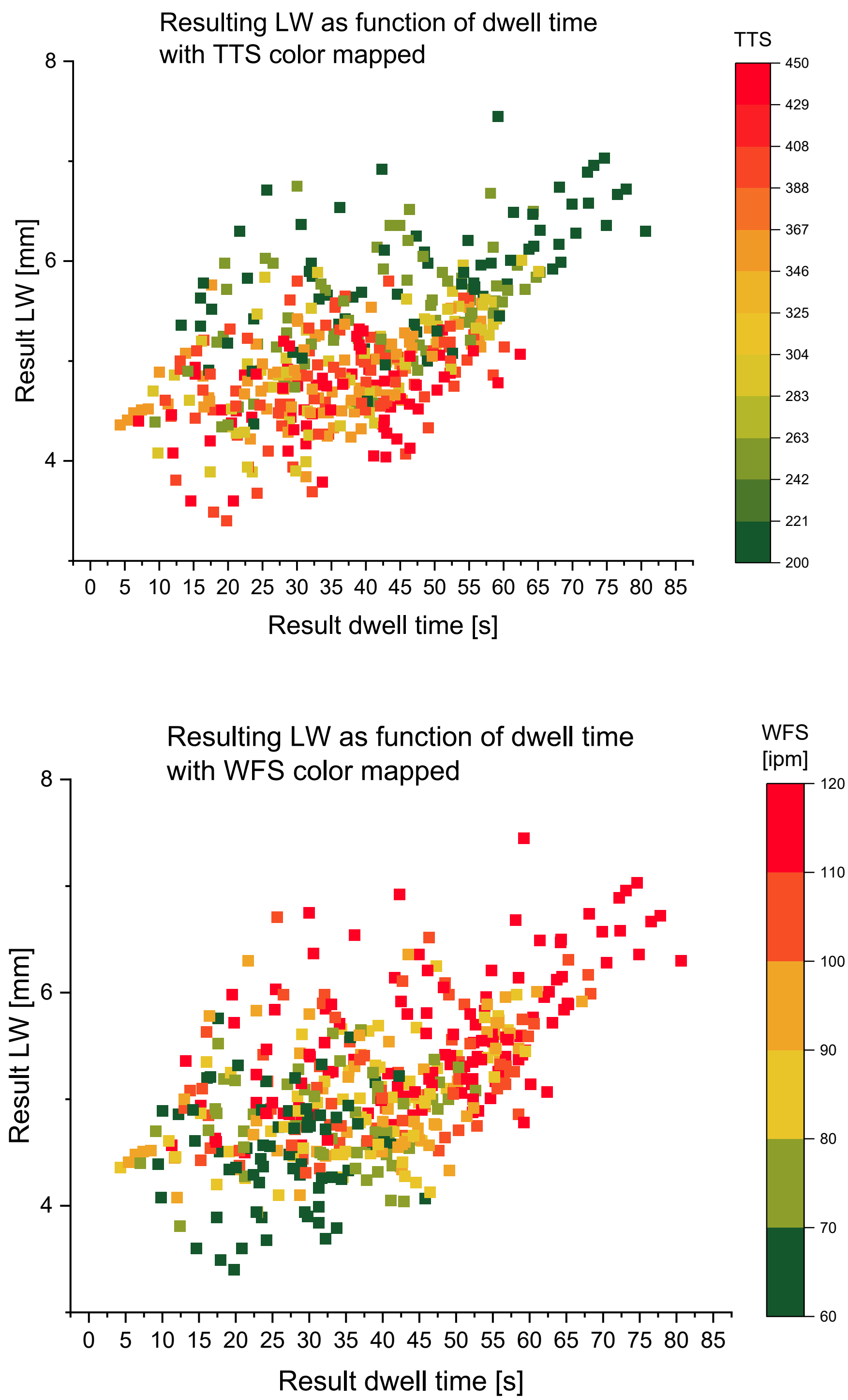

Figure A.6 Resulting layer width as a function of dwell time color mapped. Evident trend is shown between the layer width, TTS and WFS